U.S. DEPARTMENT OF COMMERCE
U.S. Environmental Science Services Administration
Weather Bureau

ESSA Technical Memorandum WBTM NMC 46

NOISE ANALYSIS OF A LIMITED-AREA FINE-MESH PREDICTION MODEL

Joseph P. Gerrity, Jr.
and
Ronald D. McPherson

RARE BOOK
QC
996
.T33
no. 46

National Meteorological Center

WASHINGTON, D.C.
February 1970

National Oceanic and Atmospheric Administration

U.S. Joint Numerical Weather Prediction Unit

ERRATA NOTICE

One or more conditions of the original document may affect the quality of the image, such as:

Discolored pages
Faded or light ink
Binding intrudes into the text

This has been a co-operative project between the NOAA Central Library, National Center for Environmental Prediction and the U.S. Air Force. This project includes the imaging of the full text of each document. To view the original documents, please contact the NOAA Central Library in Silver Spring, MD at (301) 713-2607 x124 or www.reference@nodc.noaa.gov.

LASON
Imaging Contractor
12200 Kiln Court
Beltsville, MD 20704-1387
April 13, 2004

~~UDC 551.509.313~~

Numerical Prediction Models

149 440

Contents

I	Introduction	1
II	Diagnosis of the primary noise components	2
III	Theoretical and numerical analysis of noise in a one-dimensional analog to the model	8
	Physical representation	8
	Mathematical representation	9
	Numerical representation	15
	Numerical solutions	15
IV	Remedial measures	23
V	Summary and conclusions	25
	Acknowledgments	27
	References	28
	Appendix A: Linear analysis of centered differences in time and space	30
	Appendix B: Linear analysis of Euler-backward time integration combined with centered-space differences	32
	Figures	35

ABSTRACT

A diagnostic study of the mechanisms responsible for producing high wavenumber oscillations (noise) in the numerical solution of the nonlinear equations governing a free surface, barotropic, atmospheric model is reported. The oscillations are identified as predominantly the result of the lattice structure of the difference equations and the boundary conditions employed to specify the solution. The analytic methods employed involved the use of space and time sections of the numerical solutions to provide a set of hypotheses. These are tested utilizing a one-dimensional linear analog of the model equations. The solution of the linear equations is obtained analytically, by the method of characteristics, and numerically. Several possibilities for removing the noise are suggested. Some improvement is demonstrated when the suggested methods are used in the linear one-dimensional analog.

I. Introduction

Interest in numerical models applicable to short-range weather prediction over limited geographical areas is currently increasing, stimulated by the desirability of forecasting "today's" weather with substantially greater precision than is usually afforded by present operational models. Such short-range prediction models seek to achieve this advantage by increasing the resolution of the spatial grid lattice on which the governing equations are solved. Enhanced spatial resolution affords the opportunity to more accurately represent significant atmospheric features, especially those of relatively small horizontal extent. This is true, both in a diagnostic sense, through more efficient utilization of available data in data-dense areas, and in a prognostic sense through the reduction of numerical truncation error, improved modeling of relevant physical processes, and more realistic representation of terrain distribution.

As a first step in the process of developing a high-resolution numerical model for short-range weather prediction, the authors recently (Gerrity and McPherson, 1969), experimented with a primitive equation barotropic free-surface model applied to the 500-mb level over the geographical area indicated in figure 1. The difference system featured the Shuman (1960) semi-momentum form for approximating horizontal derivatives, and the Euler-backward (Kurihara, 1965) technique for temporal differencing. A grid lattice of 53 by 57 points separated by 190.5 km at 60 N (one-half the operational NMC grid length) was used. Initial data were obtained by interpolating the operational NMC analyses of 500-mb height and wind to the fine-mesh grid; no initial balancing was attempted. The lateral boundaries were treated by holding both height and velocity constant with time.

Early tests with this model showed that by the twelfth hour the most striking characteristic was the virtually complete contamination of the forecast by noise of approximately two grid intervals in wavelength and of appreciable amplitude. Now, the difference method used does not admit a tendency in the two-grid-interval wave; how, then, could this noise appear? This mysterious and disheartening result was jolted into the background by the simple device of passing a selective low-pass filter of appropriate response characteristics over the field, thereby uncovering what appeared, by comparison to the unfiltered fields, to be a nearly flawless forecast. More penetrating investigations showed it to be not without flaws, of course, but a series of subsequent integrations indicated that the predictions of this dynamically simple model, with the simplest possible boundary conditions, compare quite favorably with those from the primitive equation baroclinic model (Shuman and Hovermale, 1968)

currently in operation at NMC and from the operational barotropic (filtered) model. The state of euphoria which this induced waned slowly, while the spectre of the noise lurked in the shadows.

Upon reflection, however, it was realized that, while this short-wave corruption is apparently innocuous in the sense that it can be tolerated in a barotropic model during the marching process and removed by filtering prior to output, similar behavior in a multi level moist, baroclinic model would probably be more troublesome. The ten-level moist baroclinic model developed by Bushby and Timpson (1967) became unstable with these constant boundary conditions, although it is not clear to what extent this was due to the short wavelength noise described above. Another noise component in the same model was detected and removed by Benwell and Bretherton (1968), and its removal occasioned significant changes in the predicted precipitation. Subsequent integrations reported by Bushby (1968) reflect a return to constant boundary conditions and treatment of the short-wave noise by artificial viscosity near the boundaries. The experience of the English investigators, combined with our experience with the barotropic model, seemed to dictate a thorough investigation of the noise components of our system before attempting to extend it to a multilevel baroclinic version. This paper is an account of that investigation.

We will rather arbitrarily define "noise" as unwanted gravitational oscillations, as contrasted with "errors" incurred in the representation of the meteorological mode. In the following sections we will be first concerned with the diagnosis of the primary noise components in the fine-mesh limited-area barotropic model, and the delineation as far as possible of their origin and characteristics. An attempt will be made to simulate some of the components within the framework of a simple, one-dimensional model in an effort to understand the excitation mechanisms. Finally, possible remedial action to eliminate or reduce the noise will be examined.

II. Diagnosis of the Primary Noise Components

The progressive corruption of the fine-mesh barotropic forecast by short-wave noise is illustrated in figures 3-6, representing three-hourly forecasts of 500-mb height to 12 hours, based on the initial data of 12Z, February 1, 1969 shown in figure 2. By the third hour the presence of the noise is quite evident and is approximately two grid intervals in length. It is observed to some degree near all of the boundaries of the grid lattice, but is most intense along the left side of the array. The interior is as yet smooth and uncluttered. The amplitude of the noise is difficult to determine unequivocably, but the variability of height from point to point is as much as 300 meters.

Figure 4 shows that by 72 iterations, or six hours forecast time, noise has affected the entire array. Some synoptic features, mainly in the interior, are still identifiable; but the meteorologically significant components of the field over roughly the left half of the grid lattice are almost completely obscured. It is of interest to compare the progression of the strikingly intense noise component over the left side of the array in figures 3 and 4. In the former, the noise is generally to the left of column 15; in the latter this delineation is not so distinct, but in general appears as far into the interior as columns 26-30. To the extent that this phenomena can be viewed as the leading edge of a group of waves the foregoing comparison suggests that the inward movement is in the vicinity of twelve grid intervals in 36 time steps. Attention should also be focused on the far left side of figure 4 between rows 15 and 35: whereas at the third hour, the meteorological character of the field to the left of column 15 is completely obscured by noise, some indication of the flow is faintly discernible at the sixth hour. This suggests that the noise is excited near the boundary and moves into the interior in pulses. Finally, it is worth noting that the most intense noise, that is, where the point-to-point variability of height is greatest, is concentrated in three main left-to-right bands; one along the lower boundary, one in the middle, and one close to the top boundary.

The banded appearance continues at the ninth hour, as shown in figure 5, but the central band again appears more pulse like in nature. Synoptic features in the interior which were corrupted but identifiable in figure 4 cannot be identified in figure 5; but the flow characteristics in the left central portion which were barely discernible at the sixth hour are easily seen. The rate of progression from left to right has continued unchanged; about 12 grid intervals in 36 time steps.

Finally, figure 6 illustrates the 500-mb height field at the twelfth hour. A first impression of this figure is one of mostly chaos and very little, if any, order. The noise is rampant over the entire field, completely obscuring the meteorologically significant field except in small local areas. Perhaps the only discernible pattern of larger scale than the noise itself are left-to-right bands which are still visible along the bottom boundary and slightly inward from the top boundary.

Underneath this chaotic distribution of height, however, there remains the field of meteorological interest. There would appear to be an analogy here to a river whose waters are polluted by garbage floating on the surface only, but not diffused through the depth: scoop off the garbage and the river is sparkling again. Passing a filter over the field shown in figure 6 corresponds to scooping off the garbage, and the result is shown in figure 7.

In order to examine further the character of this short-wavelength noise, graphs of height as ordinate against time-step as abscissa have been plotted for a cluster of grid points in the lower right portion of the array; the points are indicated in figures 3, 4, and 5 by underlining. This particular group of points was chosen because of the relatively small observed change in the 500-mb height over the 12-hour period; the observed change at the central point was a rise of slightly less than 40 meters.

Figure 8 illustrates the temporal behavior of the height as computed at each time step for the three adjacent points in a column, oriented approximately north-south. The values plotted are "raw;" that is, no filtering has been applied other than that associated with the Euler-backward time-differencing scheme. There are three features of this graph which are important to note. First, the behavior of the height with time at each point individually: let attention be focused on the central point. The solution for the height at this point seems to bear a remarkable resemblance to a relatively long-period gravitational oscillation. A minimum is reached between the first and second hours, and a maximum about five hours later, suggesting a ten-hour period, approximately. The amplitude is difficult to estimate, but the variability from minimum to maximum is about 170 meters; this is far greater than could reasonably be associated with the meteorological mode. At the two adjacent (odd-numbered in the north-south direction) points, the height again behaves in a manner difficult to associate with the synoptic pattern. Mentally filtering, for the moment, the prominent oscillation of about a two-hour period which will be considered subsequently, the solution for the height at these two points appears to rise to a maximum near the fifth hour and then diminish. The suggested period for this oscillation is again around ten hours, but the minimum to maximum variability is somewhat less than at the central point, around 100 meters. Evidently, then, the variability of height with time associated with the systems of meteorological interest is overwhelmed, at least at these three points, by that associated with an oscillation of apparently gravitational character, possessing a period of about ten hours and a trough-to-crest variability of 100-200 meters.

Secondly, the solution at the central (even-numbered) grid point and the solution at its odd-numbered neighbors are clearly marching to different drummers; that is, the latter is about 90 degrees out of phase with respect to the former, in addition to apparently possessing significantly less amplitude. As a result of the phase difference, there is a strong north-south variability of height from point to point; at the sixth hour, for example, the height varies from around 5690

meters at point five to about 5820 meters at point six to about 5750 meters at point 7. This, then, is the north-south component of the two-grid-interval noise which is so prominent in figures 3 through 6.

Thirdly, figure 8 shows the previously mentioned oscillation of about a two-hour period superimposed on the longer-period wave. It is most evident on the odd-numbered points, although discernible on the central point. The oscillation is clearly damped out with time, a characteristic which is no doubt due to the Euler-backward integration technique. Maxima are visible at about 1.5, 3.5, and 5.5 hours before the amplitude is reduced to an indistinguishable level.

The behavior of this prominent high-frequency oscillation is perhaps more lucidly illustrated in figure 9, which differs from its immediate predecessor only in that the heights were filtered by the selective low-pass filter referred to earlier. Filtering completely the two-grid-interval wave effectively recouples the differing solutions at the alternate grid points, so that the feature now under consideration stands out clearly. It will be observed from this figure that the initial amplitude is perhaps 60 meters, but is reduced to virtually zero after the sixth hour. It will also be seen that this high-frequency noise component is superimposed upon what appears to be an almost linear upward trend with a slope of about ten meters per hour. This is about thrice the average observed rate, based on a 40 meter rise in twelve hours. Therefore, either the recoupling of the long gravity wave components of the solution through use of the filter does not remove all of the long-period, relatively large amplitude gravitational oscillation, or the constant boundary conditions induce a frightful distortion of the meteorological mode. More argument on this question will be presented shortly.

Figures 10 and 11 present the unfiltered and filtered heights respectively, as a function of time for three adjacent points in a row, roughly oriented east-west. Note that in the unfiltered case the behavior of the solution is similar at all three points until after the seventh hour, when that at the central (odd-numbered in the east-west direction) responds to that drummer again and begins to diminish while the solution at its neighbors rather sharply increases, thus giving rise to the two-grid-increment east-west component observed on figures 3-6. The time of this departure from sensibly similar solutions corresponds to the arrival of the very intense band of two-grid-interval noise which progresses from left to right across the grid array, as in figures 4 and 5. Figure 11 again shows that recoupling of the solutions by filtering yields essentially the same behavior in the east-west direction as in the north-south.

Of the main components of the noise thus far identified, clearly those which possess the most potential for causing difficulty are the relatively low frequency, high amplitude oscillations which appear at alternate grid points. The higher-frequency perturbation is damped out rather rapidly by the Euler-backward difference scheme, and thus cannot cause much mischief. To the extent that the low-frequency components are eliminated by recoupling their alternate grid point behavior, these waves are rendered innocuous; however, a significant fraction of their amplitude remaining after filtering would constitute a rather serious error in the forecast. Since there is some evidence in figures 9 and 11 that the latter event may occur, further examination of this possibility is warranted.

The 12-hour 500-mb height forecast, filtered immediately prior to output, was compared with the observed distribution, and the difference field is presented in figure 12. Error, that is, distortion of the meteorological mode, is clearly present, but it is not obvious to what extent noise associated with the gravity mode is present. If attention is directed to the central portion of the lowest six rows of grid points, it will be observed that there is an extensive area of positive differences ranging from 40 to 100 meters. It is difficult to believe that this is all attributable to errors in the representation of the meteorological mode, since the assumption of temporal constancy of heights and winds does not appear unreasonable, especially over the left half of this boundary. Observed height changes at the boundary, not included in figure 12, were less than 20 meters up to and including column 24, and somewhat larger over the remainder of the southern boundary. Indeed, along column 24, for example, the observed height change at the boundary was only eight meters, but the errors within six grid lengths are an order of magnitude greater.

An attempt was made to separate errors in the meteorological mode from the gravitational noise which was only partially successful, but may still offer some instructive insight. In order to isolate the effect of the limited-area boundary conditions, the same physical model was integrated over the entire northern hemisphere, and the results were compared with the limited-area forecast. The difference field (limited-area minus hemispheric) between the two 12-hour forecasts, both filtered prior to output, is given in figure 13. It is evident that the limited-area forecast contains a bias toward rather large positive differences over a broad area, and that this bias is especially pronounced over the southern portion of the grid array. The time variability of this is shown in cross-sections along column 25 (80 W) at several hours during the period; these are shown in figure 14. It should be emphasized that, while these diagrams do not distinguish

clearly the gravitational noise from the synoptic error, the introduction of an artificial boundary as in the limited-area forecast results in a systematic and spurious height increase over a broad area inward from the southern boundary. Since the assumption of temporal constancy of heights and winds appears to be far less damaging with respect to the meteorological mode along this boundary than elsewhere around the limited-area grid, this result indicates at least that something other than synoptic error is involved.

We shall now attempt to construct a synthesis of the primary noise components and their characteristics. The investigation has uncovered three main noise components: an oscillation of about a two-hour period, one of longer period (about ten hours) on even gridpoints, and another of the same period but of different amplitude and phase on odd gridpoints. The last two components when viewed together constitute large amplitude two-grid-interval noise; but clearly the two-grid interval noise is not a primary component.

All three of the gravitational oscillations that have been identified must arise from imbalances in the initial analyses of pressure, height, and velocity. This problem, generally known as the "initialization problem," has been the subject of much investigation over the past decade, leading to a substantial accumulation of knowledge to which we will not attempt to add in this paper. It will simply be taken for granted that the source of the noise is in the initial imbalance between the pressure gradient force and the Coriolis acceleration, and attention will henceforth be directed at the behavior of the noise.

The oscillation with a two-hour period is of relatively little importance in this model because it is damped out so rapidly. We have observed that it possesses initially a trough-to-crest variability of about 60 meters, but disappears after the sixth hour. Little further mention of this noise component will be made, except to show in Appendix A that a wave of this frequency is, indeed, damped rather strongly by the Euler-backward time differencing technique.

Of more importance are the longer period oscillations. It has been estimated that the frequency of these oscillations is around ten hours, and the wavelength roughly the same as the dimensions of the grid-point array. The oscillation carried on the even-numbered points is significantly different, both in amplitude and phase, from that carried on odd-numbered points. This difference is manifested as two-grid-interval noise, of great amplitude where the solutions differ the most and of small amplitude where the solutions are close to one another. There is considerable evidence that filtering the two-grid-interval

noise does not completely recouple the different long-wave solutions, but leaves a residual near the boundaries which may contribute substantially toward an observed broad scale error of fairly large magnitude.

The remainder of this paper is concerned mainly with the two low-frequency oscillations. We attempt in the next section to simulate these components of the noise in a one-dimensional gravity-wave model which possesses most of the essential attributes of the two-dimensional model.

III. Theoretical and numerical analysis of noise in a one-dimensional analog to the model.

Physical representation

Consider a swimming pool* of uniform depth constructed with a lip and a drain around its periphery, as illustrated in cross-section in figure 15. In addition to being equipped with the customary lip and drain, we assume that this pool has a spout very near the lip and an automatic sensing system which is activated if the level of the fluid falls the slightest amount below the level of the lip, and inserts just exactly the amount of fluid required to bring the fluid back up to lip-level. Furthermore, we assume that the required fluid is inserted in a very thin layer immediately adjacent to the wall. The lip-spout-drain (LSD) system thus acts, in theory at least, to keep the height of the fluid constant and the fluid velocity zero at the edge of the lip.

Now assume that a rock of very small mass compared to the total mass of fluid is dropped in the middle of the pool. The gravity waves which are excited on the surface of the fluid go scurrying out in all directions and specifically toward the edge of the pool. As soon as they approach the edge, the LSD system is activated: fluid is added or withdrawn as necessary to keep the level constant at the lip. Very quickly the waves are absorbed at the boundary, and the surface again becomes calm. It is worth noting that this system does massive violence to the concept of conservation of mass in the short run, but is mass-conserving in the long run. Kinetic energy is not conserved in either run, but is continually dissipated.

Once the gravity waves are excited in the middle of the pool, they obey the familiar laws which govern gravitational oscillations. However, when they propagate to the vicinity of the lip, the LSD system comes into play, and very different and much more complicated physical laws apply. The mathematical representation of this system in its entirety

*The authors are indebted to Dr. John D. Stackpole of NMC for the analogy.

is therefore very complex, assuming such a representation can be formulated at all. In the following analysis, we will avoid this difficulty by proclaiming that the physics of the layer immediately adjacent to the lip are of secondary interest to the larger aspects of the problem; that the motions of interest are governed by the gravity wave equations, and the characteristics of the boundary are adequately treated by holding the height constant at its initial value, and the velocity zero.

Before considering the mathematical formulation of this problem, it is well to reflect upon the degree to which this physical system is analogous to the two-dimensional model. We have constructed a physical system which admits of gravity waves, which constitute the main noise components in the two-dimensional model, and we have required boundary conditions identical to those in that model. An essential difference is that the swimming pool is undergoing neither translational nor rotational velocity. The velocity therefore vanishes at the lip, and the height (in the undisturbed state) is uniformly horizontal; whereas in the two-dimensional model, the velocity is not required to vanish at the boundaries, and the height slopes downward from south to north. To include translational motion in this model does not seem worth the effort, and to include rotational motion, thus allowing for a sloping surface, would add substantially to the difficulty of the analysis. It is not known to what extent these omissions will affect the validity of the results.

Mathematical representation

The equations governing the gravitational oscillations which are excited by some mechanism in the interior of the pool are, in one space dimension,

$$\frac{\partial u}{\partial t} + g\frac{\partial h}{\partial x} = 0, \tag{1}$$

and

$$\frac{\partial h}{\partial t} + H\frac{\partial u}{\partial x} = 0, \tag{2}$$

where u represents fluid velocity, h the local depth of the fluid, H its mean depth, and g the acceleration of gravity. The horizontal dimension of the pool is denoted by X, and the boundary conditions to be imposed are

$$\left.\begin{array}{l} u = 0 \\ h = H \end{array}\right\} x = 0,\ x = X, \tag{3}$$

for all values of time. It will be assumed that (1) and (2) completely govern the behavior of the fluid in the region $\delta x \leq x \leq X - \delta x$, where

δx represents the dimensions of the boundary layer adjacent to the lip in which some other unspecified equations apply. Finally, we will assume that at $t = 0$ the height field is everywhere equal to the mean depth of the fluid, and the velocity field is given by

$$u(x, 0) = U \sin \frac{2\pi m x}{X}, \tag{4}$$

where U is an amplitude and m is an integer. The system (1) and (2) is linear and may be solved rather easily on an infinite domain; but the boundary conditions (3) restrict the domain in a particular fashion. The system, together with the boundary conditions, can be treated by the method of characteristics. Convenient references to the method in the literature are Freeman (1951), or for a more general treatment, von Mises (1958).

For convenience, we adopt the notation $\partial(\ )/\partial t = (\ )_t$, and $\partial(\ )/\partial x = (\ )_x$. The equations become

$$u_t + g\, h_x = 0 \tag{5}$$

and

$$h_t + H u_x = 0. \tag{6}$$

Let $\vec{i}$ and $\vec{j}$ be defined as unit vectors directed along the x and t axes respectively. Then

$$\mathrm{grad}(u) = \vec{i}\, u_x + \vec{j}\, u_t \tag{7}$$

and

$$\mathrm{grad}\,(h) = \vec{i}\, h_x + \vec{j}\, h_t. \tag{8}$$

Further, let us define $c \equiv (gH)^{1/2}$, and

$$\vec{S}_1 = \vec{i}\,(gH)^{1/2} + \vec{j} = c\,\vec{i} + \vec{j} \tag{9}$$

and

$$\vec{S}_2 = -\,\vec{i}\,(gH)^{1/2} + \vec{j} = -\,c\,\vec{i} + \vec{j}. \tag{10}$$

Now, if (6) is multiplied by $(g/H)^{1/2}$ and first added to, then subtracted from (5), the results are

$$(c/H)(h_t + c h_x) + u_t + c u_x = 0, \tag{11}$$

and

$$-(c/H)(h_t - ch_x) + u_t - cu_x = 0. \tag{12}$$

It can be shown that these two equations are equivalent to

$$\vec{S}_1 \cdot \text{grad}\,(u + [c/H] \cdot h) = 0 \tag{13}$$

and

$$\vec{S}_2 \cdot \text{grad}\,(u - [c/H] \cdot h) = 0. \tag{14}$$

Note that $\vec{S}_1 \cdot \vec{S}_2 = -c^2 + 1$, so that $\vec{S}_1$ and $\vec{S}_2$ are not orthogonal unless c is scaled to be unity.

The directions determined by $\vec{S}_1$ and $\vec{S}_2$ define the directions of the characteristics of the set of equations (5) and (6); the characteristics are defined by von Mises (1958) as "curves ... along which analytically different solutions of a differential equation or a system of such equations can be patched together." Equations (13) and (14) state that along these lines the linear combinations $(u + [c/H] \cdot h)$ and $(u - [c/H] \cdot h)$ are invariant.

The problem consisting of the differential equations (5) and (6) and the boundary conditions (3) may be posed as follows. At some time $t = 0$ we may give both u and h in some interval $0 \leq x \leq X$. Now consider a point on a boundary curve $x = X$, $t = t^*$. The characteristic line with direction defined by $\vec{S}_1$ will intersect this point and a point on the initial ($t = 0$) line provided that $0 \leq t^* \leq X/c$. The x - intercept of this characteristic line with the $t = 0$ axis is $x = X - ct^*$. Since $(u + [ch]/H)$ is invariant on this characteristic line, it follows that the values of u and h at (X, t^*) are related as follows:

$$u(X, t^*) = -(c/H)\, h(X, t^*) + [u(X - c\,t^*, 0) + (c/H)\, h\,(X - c\,t^*, 0)]. \tag{15}$$

Clearly, it is not consistent with the differential equation to specify arbitrarily both u and h on the initial line $t = 0$ and on the boundary curve $x = X$. Similar arguments apply to the line $x = 0$. It can be seen that we are at liberty to specify initial conditions on u and h, and <u>either</u> u or h but not both, along a boundary curve. Physically, this can be interpreted as follows: if one encloses a fluid region within a rigid wall, the only information one has about the behavior of the fluid at the wall is that no fluid penetrates the wall.

However, we have previously asserted that the physical system we are representing is such that throughout the interior of the interval

$0 < x < X$ the differential system (5) and (6) is valid, but in the neighborhood of $x = 0$ and $x = X$, a mechanism is active which does not obey the differential system. Rather, this mechanism requires u and h on the lines $x = 0$ and $x = X$ to be independent of time. Now the differential equations permit "influences" to propagate only along characteristic lines. The corollary of this is that the solution may be discontinuous across a characteristic line.

With the problem as posed above, expressed by (3), (4), (13), and (14), we may examine the nature of the solutions. Figure 16 illustrates that the domain: $t \geq 0$, $0 \leq x \leq X$, may be partitioned into four regions by considering just the characteristic lines originating at the points $t = 0$, $x = 0$, and $x = X$.

Within R_1 the solution depends solely upon conditions imposed on the initial line $t = 0$, $0 \leq x \leq X$. Consider a point (x, t) in R_1: it will be the intersection of two characteristic lines, one originating at $x_0 = x - ct$ with direction given by $\vec{S}_1$, and the other originating at $x_1 = x + ct$ with direction given by $\vec{S}_2$. At this point both of the equations

$$u(x, t) + (c/H)h(x, t) = U \sin k(x-ct) + (c/H) \cdot H, \tag{16}$$

and

$$u(x, t) - (c/H)h(x, t) = U \sin k(x + ct) - (c/H) \cdot H \tag{17}$$

must be valid, where $k = 2\pi m/X$. Therefore,

$$u(x, t) = (U/2)\left\{\sin k(x-ct) + \sin k(x + ct)\right\} \tag{18}$$

and

$$h(x, t) = H + (HU/2c)\left\{\sin k(x-ct) - \sin k(x+ct)\right\} \tag{19}$$

represent the solutions at any point (x, t) in R_1.

This may be interpreted as follows. Given a disturbance defined at $t=0$, $0 \leq x \leq X$, one part will propagate to the right at the rate $c = (gH)^{1/2}$ with half the original amplitude, and another part will propagate to the left at $c = -(gH)^{1/2}$ also with half the original amplitude. The "influence" of the first part will propagate along the positive characteristic parallel to $\vec{S}_1$ and also originating on $t = 0$. Thus, the solution at any point (x, t) in R_1 consists in part of a wave propagating to the right along a positive characteristic originating at $(t = 0, x_0 = x - ct)$, and in part of a wave propagating to the left along a negative characteristic originating at $(t = 0, x_1 = x+ct)$.

Consider now the region denoted by R_2 in figure 16. A point (x, t), $x > 0$, is again the intersection of two characteristic lines: one, with a negative slope, originating on the initial line, and the other, with a positive slope, which originates on the boundary $x = 0$. The negative characteristic intercepts the initial line at $x_1 = x + ct$; the intercept of the positive characteristic is irrelevant, since it requires that the characteristic equation

$$u(x,t) + (c/H)\, h\,(x,t) = (c/H)\, H \tag{20}$$

be valid, irrespective of where the characteristic intercepts the boundary. The characteristic equation on the negative characteristic is

$$u(x,t) - (c/H)\, h(x,t) = U \sin k\,(x + ct) - (c/H)\, H. \tag{21}$$

Combining (20) and (21) yields the solutions,

$$u(x,t) = (U/2) \sin k\,(x+ct) \tag{22}$$

and

$$h(x,t) = H - (HU/2c) \sin k\,(x+ct) \tag{23}$$

The solutions in R_2 for $x > 0$ are therefore composed in part of a signal propagating leftward along a negative characteristic originating on the initial line, and carrying half of the original amplitude. The other part of the solution is a signal propagating to the right along a positive characteristic originating on the boundary curve $x = 0$, and communicating to the fluid, in effect, "Peace: be still!"

In R_3 the situation is the reverse of that in R_2. We have the two characteristic equations

$$u(x,t) - (c/H)\, h\,(x,t) = -(c/H)\, H \tag{24}$$

along the negative characteristics, and

$$u(x,t) + (c/H) h(x,t) = U \sin k(x-ct) + (c/H) H \tag{25}$$

along the positive characteristics. Both must be valid at any point (x, t) in R_3, so the solutions are

$$u(x,t) = (U/2) \sin k\,(x-ct) \tag{26}$$

and

$$h(x, t) = H + (HU/2c) \sin k (x-ct) \tag{27}$$

In R_3, then, the solutions are composed of a wave originating on the initial line and propagating to the right along a positive characteristic, and a "peace" signal emanating from the boundary line $x = X$.

Finally, in R_4 the solutions are completely independent of data on the initial line. Any point (x, t) is the intersection of a positive characteristic originating on the boundary curve $x = 0$ and a negative characteristic originating on the boundary curve $x = X$. The solutions therefore are

$$u(x, t) = 0 \tag{28}$$

and

$$h(x, t) = H \tag{29}$$

A schematic illustrating the solutions is given in figure 17. It can be seen that in R_1 both u and h respond in a familiar standing wave pattern. In R_2, however, the solution is mixed: the leftward-propagating wave is approaching the boundary, and the boundary is acting to increase the level of the fluid and diminish the velocity. Mass is therefore being added and kinetic energy withdrawn near the boundary $x = 0$. In R_3, the boundary is again acting to increase the level and to force the negative velocity toward zero: again mass is added and kinetic energy withdrawn. By time $t = X/2c$, the effects of this process are clearly visible: the mean level of the fluid is obviously higher than its original value, and the kinetic energy is greatly diminshed. After this time, the boundaries begin to extract the fluid which had previously been added and continue to withdraw kinetic energy. By time step 100 ($t = X/c$), all kinetic energy and excess fluid have been withdrawn, and the disturbance has vanished.

The solution to the problem constructed by the method of characteristics is therefore in agreement with our preconceived notion of what would happen in the swimming pool: disturbances excited in the interior of the pool move out to the edge and are swallowed up by the drain. In time, the pool becomes uniform and motionless. With reference to the two-dimensional barotropic model, it appears that, to the extent that the damping properties of the boundary conditions apply only to the gravity mode, holding the boundaries constant with time is an excellent technique, since all gravity waves arising from the initial data should be absorbed at the boundaries, given enough time. This

observation hinges, of course, on the accuracy with which the numerical solution approaches the theoretical solution just obtained; we now examine the numerical simulation of the physical system.

Numerical representation of the one-dimensional model

We now consider that the region indicated in figure 16 is to be subdivided in rectangles of equal size. In the x-dimension we will require 101 equal segments of the original domain $0 \leq x \leq X$, thus defining 101 discrete and equally-spaced points on the x-axis. Position on the x-axis is then described by $x = j\Delta x$, $j = 0, 1, 2, \ldots 100$. Similarly, the time axis is subdivided into equal intervals Δt, and any particular $t \geq 0$ is given by $t = n\Delta t$, $n = 0, 1, 2, \ldots N$. The differential equations (5) and (6) are to be transformed to a suitable finite-difference analog and solved numerically on this lattice of points in (x, t) space, subject to the boundary conditions (3) applied to $x = 0$ and $x = 100\Delta x$ for all time.

In the barotropic two-dimensional model, the semi-momentum form was used to approximate horizontal derivatives; in this linear one-dimensional experiment, this form collapses to the customary centered-difference form. The Euler-backward technique was used for time-differencing in the two-dimensional model because of its damping property.* However, it is precisely this property which renders it unattractive in the present experiment, since it is desired to study the effect of a particular set of boundary conditions isolated from any damping due to the time-integration scheme. Accordingly, the numerical solutions shown in this section utilized a centered-time-differencing scheme, with a forward time-difference initially. All of the one-dimensional experiments were duplicated using the Euler-backward technique, but are not included here.

Numerical solutions obtained from a one-dimensional model

In the numerical experiment discussed in the following paragraphs, the differential equations (5) and (6) were transformed to the difference equations:

$$u_j^{n+1} = u_j^{n-1} - \frac{g\Delta t}{\Delta x}\left(h_{j+1}^{n} - h_{j-1}^{n}\right) \tag{31}$$

$$h_j^{n+1} = h_j^{n-1} - \frac{H\Delta t}{\Delta x}\left(u_{j+1}^{n} - u_{j-1}^{n}\right) \tag{32}$$

*See Appendices A and B for linear analyses of the characteristics of the centered (leap-frog) and Euler-backward techniques respectively.

The mesh length was taken as 10^4 m, so that the total extent of the x-domain is 10^6 m; the mean depth of the fluid was taken as 10^4 m. The time increment was computed such that $\sqrt{gH}\ (\Delta t/\Delta x) = 1$, which represents the limit of computational stability for the centered space and time difference scheme. Initial conditions consisted of a sine wave of wavelength 10^6 m (wave number one) and amplitude 5 m sec^{-1} in the velocity field, and a uniform height field equal to the mean depth of the fluid, 10^4 m. The velocity was held at zero and the height set equal to H at x=0 and x=X for all time. The integration was carried out to 110 time steps, or well into the R_4 of figure 17 where the analytic solution obtained from the method of characteristics calls for zero velocity and uniform height.

The results of the integration are presented in figures 18-21. The first three of these are composed of panels which, taken together, show the solutions for velocity and height at time steps 5 and 10 and every $10\Delta t$ thereafter. It should be noted prior to discussing these diagrams that the short, solid, vertical lines in each panel denote the actual boundary of the region of integration. It will be observed in the panels for the fifth and tenth time steps that two-grid-interval noise is being excited at the boundary and is progressing into the interior steadily. The "dots" representing the solutions at individual grid points have been connected in the panels representing height at these two times; this practice is not repeated in subsequent panels in order to clearly demonstrate the "splitting" on the solutions at alternate grid points.

Indeed, by time step 50, the two-grid-interval noise, or the process of splitting, has progressed completely into the interior of the region. It is seen with much more clarity than in the similar figures from the two-dimensional case that there exists one solution on even-numbered grid points and a completely different solution on odd-numbered grid points. Let us examine the nature of these solutions. With respect to the height field at this time, the solution on odd grid points shows the same double-bump structure that appears in the analytic solution for the same time, as illustrated in figure 17. In fact, however, closer perusual reveals that it is identical to the analytic solution except that it possesses twice the amplitude. On the even grid points the height field is sensibly constant in the x-dimension; the minor fluctuations are due to a lack of resolution in the computer program used to plot the graphs. This solution is that which would be obtained if the problem were solved under rigid wall conditions imposed at the boundaries.

The solutions for the velocity at time step 50 exhibit somewhat different behavior. On odd grid points the solution is a sine wave 90 degrees out of phase with the original wave and of amplitude 5 m sec^{-1}; this is the pure-reflection solution that would be obtained with rigid wall boundary conditions. On even grid points, the velocity is essentially zero, which is not the solution predicted by the method of characteristics; the analytic solution calls for a sine wave 90 degrees out of phase with, but with only half of the amplitude of the original wave.

At time step 50, in summary, we see a pure-reflection solution for the height on even grid points and for the velocity at odd grid points. The height solution on odd grid points is identical with the analytic solution except that it possesses twice the amplitude; the velocity solution on even grid points has no amplitude at all. It is worth noting that the numerical solution for height on odd points, which resembles the analytic solution, indicates that much more mass has been added by the former than is required by the latter. By the same reasoning, the solution for velocity on even points indicates that all of the kinetic energy has been withdrawn from the fluid. It is almost as if the LSD mechanism of the swimming pool has suffered a malfunction, pouring much more mass into, and extracting much more energy from, the pool than is necessary.

The solutions at subsequent times continue to clearly show a pure-reflection solution for the height on even grid points and for the velocity on odd grid points. Height on odd points and velocity on even points obviously are responding to that other drummer mentioned previously; the solutions do not appear to bear any resemblance to the analytic solution. By time step 100, the solutions for height on both even and odd points are essentially the same; both are going through a nodal time. The velocity solutions appear to be identical but exactly out of phase; however, averaging the two solutions (filtering the two grid interval noise) would apparently yield a good approximation to the analytic solution. Ten time steps later, however, the pure-reflection solutions still appear, but the other solutions are obviously such that averaging does not yield the analytic solution. In fact, a one-dimensional version of the filter mentioned earlier in connection with the barotropic model was passed over the solutions at the 110th time step; this would correspond to applying the filter to the barotropic model prior to output. The filtered solutions are shown in the lowest panels of figure 20. In the interior of the region the filtered solutions are reasonably close to the analytic; but near the boundaries there results a departure from the analytic solution amounting to, in the height field, about 40 meters.

The panels in figure 21 give the behavior of the velocity and height at four adjacent grid points at each time step, and are intended to be compared with figure 8. The pure-reflection solution for the height on even grid points and for velocity on odd grid points is again evident.

We have therefore shown through this numerical experiment that the differencing system utilized admits of solutions which bear little or no resemblance to the analytic solutions. In doing so we have apparently captured in this simple model the essential behavior of the two main long wave noise components of the two-dimensional barotropic model. Having described the problem as it first manifested itself, and having subsequently simulated it in a simpler framework, we are now to the point where it is necessary to gain an understanding of its nature.

Consider the structure of the difference equations (31) and (32) in the space-time lattice of figure 22. It can be seen that, for the linear equations, solutions on points marked by triangles depend only on points similarly designated. For example, the solution for height at point (4, 4) depends on the value of height at point (4, 2) and the values of velocity at points (5, 3) and (3, 3). The same arrangement is true with respect to the solution for velocity at point (4, 4). Points marked by circles are similarly interconnected; but there is no interchange (in the linear equations) between the two sets of points.

Platzman (1958) noted this double-lattice structure in pointing out a potential instability associated with the additional boundary condition (on the outflow boundary) required by raising the order of the equations through the use of centered differences. Later, Matsuno (1966), following the ideas of Wurtele(1961) and Nitta (1962), clearly showed that raising of the order of the equations produces a spatial computational mode. This artificial mode of the solution is formally equivalent to the temporal computational mode discussed by Gates (1959) and others, and appears as the highest resolvable wave number when both lattices of figure 22 are considered together. A recent analysis by Gerrity (1969) has shown that this manifestation is misleading: it results from viewing lower wave number solutions on the two independent lattices simultaneously. Matsuno indicated that large errors can arise through improper treatment of the computational mode by the boundary conditions. His boundary specifications require that the normal component of the velocity and the normal derivative of height vanish at the boundary. These represent an overspecification required by the second-order character of the difference equation; but both conditions are mutually compatible in that they are both applicable to the same physical problem, the behavior of a fluid confined by rigid walls.

The boundary conditions used here, holding both velocity and height invariant with time on the boundaries, are quite different in that they are not applicable to the same physical problem. That is, the vanishing normal component of velocity for all time on the boundary is appropriate for the fluid confined by rigid walls, but constraining the height to be constant is related to the LSD system. It will now be demonstrated that these boundary conditions give rise to two distinct solutions on the independent lattices.

The solution of (31) and (32) at point (1, 1) is given by a forward time step, which introduces the possibility of a temporal computational mode. We will assume that for the low frequency oscillation specified initially, the temporal computational mode is of small amplitude. The formulae are

$$u_2^2 = u_2^1 - \frac{g\Delta t}{2\Delta x} (h_3^1 - h_1^1) \tag{33}$$

and

$$h_2^2 = h_2^1 - \frac{H\Delta t}{2\Delta x} (u_3^1 - u_1^1). \tag{34}$$

Now, h_1^1 and u_1^1 are specified boundary values. The solution for height at $x = \Delta x$, $t = \Delta t$ therefore depends <u>only</u> on the velocity boundary condition, while the solution for velocity depends <u>only</u> on the height boundary condition.

Let us now assume that we have completed the first forward time step for all x and consider the solutions at point $x = \Delta x$, $t = 2\Delta t$. These are given by (31) and (32):

$$u_2^3 = u_2^1 - \frac{g\Delta t}{\Delta x} (h_3^2 - h_1^2), \tag{35}$$

and

$$h_2^3 = h_2^1 - \frac{H\Delta t}{\Delta x} (u_3^2 - u_1^2). \tag{36}$$

Again u_1^2 and h_1^2 are specified boundary values, and the height solution depends <u>only</u> upon the velocity boundary condition, while the velocity solution depends <u>only</u> upon the height boundary condition.

Consider now the solutions at $x = 2\Delta x$, $t = 2\Delta t$:

$$u_3^3 = u_3^1 - \frac{g\Delta t}{\Delta x} (h_4^2 - h_2^2), \tag{37}$$

and

$$h_3^3 = h_3^1 - \frac{H\Delta t}{\Delta x}(u_4^2 - u_2^2). \tag{38}$$

Substituting from (33) and (34) into (37) and (38) for h_2^2 and u_2^2 yields

$$u_3^3 = u_3^1 - \frac{g\Delta t}{\Delta x}\left\{h_4^2 - \left[h_2^1 - \frac{H\Delta t}{2\Delta x}(u_3^1 - u_1^1)\right]\right\} \tag{39}$$

and

$$h_3^3 = h_3^1 - \frac{H\Delta t}{\Delta x}\left\{u_4^2 - \left[u_2^1 - g\frac{\Delta t}{2\Delta x}(h_3^1\, h_1^1)\right]\right\}. \tag{40}$$

In contrast to the previous solutions obtained for $x = \Delta x$, the solution for velocity at $x = 2\Delta x$, $t = 2\Delta t$ can be related to the boundary condition on velocity, whereas the solution for height can be related to the boundary condition on height. This demonstration could be continued, but it would serve merely to confirm the observations made thus far, namely:

1. that the solution for height on even-numbered grid points (in the x-direction) and the solution for velocity on odd-numbered grid points can trace their ancestry directly to the boundary condition on velocity, only, and

2. that the solution for height on odd-numbered grid points and the solution for velocity on even-numbered grid points can trace their ancestry directly to the boundary condition on height, only.

Let us consider the implications of this dichotomy of boundary dependence. Returning to the swimming pool analogy, if we for the moment replace the intricate mechanisms of the LSD system with a simple rigid wall, we are left with only one boundary condition, namely that the velocity component normal to the wall shall vanish at the wall. We know that under such circumstances the gravity waves are simply reflected from the wall, and in the absence of viscosity, will richochet back and forth between the walls indefinitely. When we solve the gravity wave equations with this boundary condition, we in fact obtain this sort of solution. By observation (1) above, we should therefore expect this type of solution for height on even-numbered grid points and for velocity on odd-numbered grid points; this was observed to be the case in figures 18-21.

Now, the boundary condition on height is related to the activity of the LSD system of the swimming pool and therefore to the complex physics

of the boundary layer to which we have previously stipulated that the differential equations do not apply. By observation (2) above, it would be expected that the solutions for height on the odd-numbered grid points and for velocity on even-numbered grid points would not be especially well-behaved. We should therefore not be surprised at the appearance of the computed solutions, as shown in figures 18-21, exhibiting as they do such features as sharp, almost discontinuous wave troughs, etc.

As a demonstration that this behavior is indeed the result of the use of centered differences, the numerical experiment illustrated in figures 18-21 was repeated on a grid lattice which is staggered in space only. That is, the variables u and h are defined only at alternate points in space as in figure 23 . Spatial derivatives can be estimated by differences over a distance Δx as opposed to $2\Delta x$ in the customary scheme. This can be viewed as replacing a first-order derivative by a first-order difference, and the reduction in order is reflected in the fact that only one boundary condition, on u or h, is now required on each boundary. For example, if velocity is defined at points in figure 23 marked by circles and height is defined at points marked by triangles, it is necessary to specify only the velocity as a function of time on the boundaries. If the velocity at the boundaries is required to vanish, then the resulting solution should exhibit pure reflection of the gravity wave in a fluid confined by rigid walls. That this is the case is shown by figures 24-26.

On the other hand, if height is defined at circles and velocity at triangles, only the height need be specified along the boundaries. If height is held constant in time on the boundaries the solutions should correspond to the peculiar behavior noted earlier. This is confirmed by figures 27-29.

Consider the solutions at the various grid points of the combined lattice as provided by the method of characteristics. Assume, with reference to figure 22 , that $(\sqrt{gH})\,\Delta t/\Delta x = 1$, so that the characteristic lines diagonally connect grid points, as shown by the dashed lines. Thus, each grid point represents an intersection of a positive and a negative characteristic, each originating at a grid point either on the initial line or on the boundary. We had, from the previous discussion of the method of characteristics, that

$$\text{grad}\,(u + [c/H]\,h) = 0 \tag{41}$$

must be valid along any positive characteristic, and

$$\text{grad}\,(u - [c/H]\,h) = 0 \tag{42}$$

must be valid along any negative characteristic. In particular, along

the positive characteristic connecting points $x = 0$, $t = 0$ and $x = \Delta x$, $t = \Delta t$ in figure 22, (41) becomes

$$\left[u_2^2 + (c/H)h_2^2\right] - \left[u_1^1 + (c/H)h_1^1\right] = 0. \tag{43}$$

Along the negative characteristic connecting $x = \Delta x$, $t = \Delta t$ and $x = 2\Delta x$, $t = 0$, (42) becomes

$$\left[u_2^2 - (c/H)h_2^2\right] - \left[u_3^1 - (c/H)h_3^1\right] = 0. \tag{44}$$

Both (43) and (44) must be valid at the intersection of the positive and negative characteristics, i.e., at $x = \Delta x$, $t = \Delta t$; adding them yields

$$u_2^2 = \frac{1}{2}(u_1^1 + u_3^1) - \frac{c}{2H}(h_3^1 - h_1^1), \tag{45}$$

and subtraction yields

$$h_2^2 = \frac{1}{2}(h_1^1 + h_3^1) - \frac{H}{2c}(u_3^1 - u_1^1). \tag{46}$$

It can be seen that the <u>analytic</u> solution for u_2^2, as given by (45) depends on the boundary specification of <u>both</u> velocity and height, as contrasted with the numerical solution (33) which depends <u>only</u> on the height at the boundary. Similarly, the analytic solution for h_2^2 depends on both boundary conditions rather than only one. This, then, is the basic cause of the dichotomous solution at alternate grid points: the centered space numerical approximation to the derivatives admit of dependency of the solutions upon only <u>one</u> of the boundary conditions at a given grid point, whereas the analytic solution requires that <u>both</u> boundary conditions influence the solution at <u>each</u> grid point.

In summary, we have therefore seen that the "splitting" of the long gravity wave solutions at alternate grid points does much more than merely obscure the meteorological fields by large amplitude two-grid-interval noise; this phenomenon actually negates the beneficial effect of the constant boundary conditions which tend to dissipate gravitational energy. Fundamentally, the problem arises because the use of centered differences in space does not couple the solutions corresponding to each boundary condition on the two independent lattices.

We have therefore unmasked the "other drummer;" we must now address the question of how to require drummers and marchers alike to stay in step.

IV. Remedial measures

We have seen, both in theory and in fact, that the short-period oscillation (2 hours) in the barotropic model is damped rather quickly by the Euler-backward time differencing technique. Damping is also experienced at least in theory, by the more troublesome oscillation of about a 10-hour period, but the damping is not very great; we were not able to observe any damping at all in the two-dimensional results. Nevertheless, the Euler-backward technique clearly qualifies as a weapon of some considerable potency against gravitational noise, provided the noise is of short period; figure B-2 in Appendix B suggests that the upper limit in terms of period is about three hours.

A low-pass filter has also been used to relatively good effect to recouple the dichotomous solutions at alternate grid points, thereby eliminating both the two-grid interval noise and most of the long period gravitational oscillations which are responsible for it. However, we have seen that recoupling the solutions via a low-pass filter leaves a long-wave residual near the boundaries, which we have related to at least part of the observed spurious buildup of heights along the southern boundary in the barotropic model (see figure 14).

A third remedial measure which has already been used is the technique of holding constant values on the boundaries. We have demonstrated that these specifications act as absorbers of gravitational energy. However, the efficacy of this weapon has been negated, as we have seen, by the inappropriate approximation of space derivatives using centered differences. The negation is in fact responsible for the necessity of using the low-pass filter against the noise, with the partial success previously described. There is a strong suggestion that some attempt be made to correct the approximation to the space derivative, and thereby allow the constant boundary conditions to exert their influence.

The last paragraphs of the previous section provide the indication of an appropriate direction in which to proceed. Equations (45) and (46), representing the analytic solution from the method of characteristics, are clearly in a form very similar to a finite-difference form. In general, if we write

$$u_j^{n+1} = \frac{1}{2}(u_{j+1}^n + u_{j-1}^n) - \frac{g\Delta t}{2\Delta x}(h_{j+1}^n - h_{j-1}^n) \tag{47}$$

and

$$h_j^{n+1} = \frac{1}{2}(h_{j+1}^n + h_{j-1}^n) - \frac{H\Delta t}{2\Delta x}(u_{j+1}^n - u_{j-1}^n), \tag{48}$$

we will obtain the exact analytic solution provided $\sqrt{gH}(\Delta t/\Delta x) = 1$.*

This promising result is flawed by the realization that the requirement for an exact solution cannot be used in practice for fear of straying over into the realm of linear computational instability unintentionally. Satisfaction of the stability criterion implies an error in the solution; the question of what magnitude and behavior it exhibits must then be addressed by means of numerical experiment.

The fundamental difficulty with the centered difference approximation is that the signal communicating both boundary conditions to the fluid is distorted in the process of reaching the first interior grid point. The initial part of the Lax-Wendroff method does not permit such a distortion for neutral stability, so that the signal reaches the first interior grid point intact. This suggests that the initial part of the Lax-Wendroff might be used profitably at the first interior grid points and centered-time or Euler-backward elsewhere in the interior.

Experiments were carried out, with the initial part of the Lax-Wendroff method (or diffusive method, as Richtmyer(1962) calls it) at the first interior grid points, and both centered and Euler-backward time differencing employed in the interior. The stability ratio $\sqrt{gH}\,\Delta t/\Delta x$ was initially set to unity. The results for centered differences in the interior are shown in figure 30. Apart from some very small amplitude noise resulting from roundoff error and exaggerated by the plotting routine, this is sensibly equivalent to the analytic solution. Using the Euler-backward method in the interior did not effect any significant change.

The experiment was repeated using a stability ratio of one-half, and the results are presented in figures 31 and 32. It will be seen that the use of a more significant value of the stability ratio, in terms of practical use, results in the appearance of a spatial computational mode, with different solutions at alternate grid points. But both solutions exhibit the same general behavior as the analytic solution; by time step 100, which is equivalent in real time to time step 50 of figure 20, the velocity solutions show the same form as in the analytic solution, and the height solutions have the same double-bump character. By the 200th time step, both solutions are practically uniform, as predicted by the analytic solution at time step 100. At time step 220, some residual amplitude is left in wave number one, and the dichotomy is again evident. Filtering the solutions at this time with a low-pass filter produces the results shown in the lowest panels of figure 32. Some residual amplitude of

*The difference-system indicated in (47) and (48) is the first half of the two-step Lax-Wendroff time-differencing technique, discussed in some detail by Richtmyer (1962) and others.

low wave number remains, with the solutions departing slightly from the desired uniformity near the boundaries; however, the greatest departure in the height field is less than ten meters.

On the basis of this result, it seems that although the one-step Lax-Wendroff scheme applied at the first interior grid point will be of assistance in controlling the noise in the two-dimensional model, it does not represent the solution to the problem.

There is yet another approach. We have seen considerable evidence that the origin of the noise components is in the initial data, presumably arising because of large imbalances between the analyzed heights and winds. It would therefore appear that the gravitational energy could be removed or reduced at the source by correcting the initial imbalances through the solution of the balance equation or by some other initialization.

Finally, we note again that the analytic solutions obtained from the method of characteristics involve both u_{j-1}^{n} and h_{j-1}^{n}, which are boundary values if $j = 2$. We also note that, under constant boundary conditions, $u_{j-1}^{n} = u_{j-1}^{n+1}$ and $h_{j-1}^{n} = h_{j-1}^{n+1}$. The implicit integration schemes discussed by Kurihara (1965) involve values u_{j-1}^{n+1} and h_{j-1}^{n+1} in the solutions for u_{j}^{n+1} and h_{j}^{n+1}. It is therefore possible that the use of an implicit integration scheme may offer an effective mechanism for coupling the solutions. In addition, such a scheme would have the salutary advantage of being absolutely stable with respect to gravitational oscillations, thus allowing a longer time step.

Both of these suggestions will be examined in subsequent experiments with the fine-mesh, limited area model.

V. Summary and Conclusions

In the fine-mesh, limited-area, barotropic prediction model designed as a first step in the development of a more general multi-level model for short-range weather forecasting, we have seen that, with the use of a particular form of finite difference approximations and a particular set of boundary conditions, the forecasts are obscured by very short wavelength noise. The examination of the character of this noise in greater detail revealed that it results from two long wavelength, low frequency gravitational oscillations, which presumably originate from an imbalance between the initial winds and heights, and which appear on alternate grid points. A third component of noise, of shorter wavelength and period, was discovered superimposed on the two longer period oscillations.

The time differencing system, the Euler-backward technique, is damping with respect to gravity waves. The damping rate is greater for shorter-wavelength, higher frequency oscillations. In particular, the last noise component in the above enumeration should be damped rapidly by the Euler-backward method; and this has been shown to occur in the barotropic model. The two longer period waves, on alternate grid points, have been shown to experience very little damping due to the Euler-backward method.

A simulation of the longer period waves in a simple one-dimensional model succeeded in illuminating the behavior of these waves. It was shown that the dichotomy of solutions at alternate grid points results from the use of a second-order difference approximation to a first-order spatial derivative. Recoupling the two solutions was seen to be partially accomplished by passing a low-pass filter over the field, but that this process leaves a residual amplitude in a low-wave number pattern so as to create errors near the boundaries.

The analytic solution of the boundary-initial-value problem by the method of characteristics suggested a finite-difference form called the diffusive method for the time derivative which can yield the exact analytic solution for the gravity mode, but only for exactly neutral computational stability. It was demonstrated by experiment that a combined differencing system of the diffusive method at the points immediately adjacent to the boundary and centered-difference or Euler-backward approximations to the time derivative elsewhere yield, for neutral stability, a numerical solution in very excellent agreement with the analytic solution for the gravity mode. However, since neutral stability is not a practical possibility, this technique does not appear to offer a useful solution.

Further remedial measures have been suggested. One suggested measure would involve reducing the amplitude of the gravitational oscillations by balancing the initial data. Another involves exploration of implicit integration techniques.

The initial objectives of the phase of the research project to develop a high-resolution, limited-area prediction model that is reported upon in this paper were threefold: to diagnose the main noise components of the barotropic model, to then gain an understanding of their origin and behavior, and finally to prescribe appropriate remedial measures to eliminate them or reduce their influence on the forecasts. In the last we have achieved only partial success. But in the first two we have quite successfully identified the noise components, exposing them to the light of methodical inquiry and have developed an understanding both physical and mathematical of their behavior; and in doing so we have elucidated the meaning and impact of the constant boundary conditions.

ACKNOWLEDGMENTS

The authors are grateful to H. Økland for his counsel during the course of this research, and for his critical review of the manuscript. We are also indebted to Dr. John A. Brown, Jr. for reviewing the manuscript, and to Mrs. Zelda Licausi for typing it.

REFERENCES

Benwell, G. R. R., and F. P. Bretherton, 1968: "A Pressure Oscillation in a Ten-Level Atmospheric Model," QJRMS, Vol. 91, pp. 123-131.

Bushby, F. H., 1968: "Further Developments of a Model for Forecasting Rain and Weather," Proc. IUGG, Tokyo, pp. II-75-84.

_____ and M. S. Timpson, 1967: "A Ten-Level Atmospheric Model and Frontal Rain," QJRMS, Vol. 93, pp. 1-17.

Freeman, J. C., 1951: "The Solution of Non-Linear Meteorological Problems by the Method of Characteristics," Compendium of Meteorology, Am. Met. Soc., Boston: 1951, pp. 421-433.

Gates, W. L., 1959: "On the Truncation Error, Stability, and Convergence of Difference Solutions of the Barotropic Vorticity Equation," J. Meteorol., Vol. 16, pp. 556-568.

Gerrity, J. P., and R. D. McPherson, 1969: "Development of a Fine-Mesh, Limited-Area Prediction Model," Monthly Weather Review, 1969, Vol. 97, pp. 665-669.

Gerrity, J. P., 1969: "Lattice Structure and Computational Modes of Centered-Difference Advection Equation," NMC Office Note No. 31, Nov. 1969.

Kurihara, Y., 1965: "On the Use of Implicit and Iterative Methods for the Time Integration of the Wave Equation," Monthly Weather Review, Vol. 93, pp. 33-46.

Matsuno, T., 1966: "False Reflection of Waves at the Boundary Due to the Use of Finite Differences," J. Meteorol. Soc. Japan, Vol. 44, No. 2, pp. 145-157.

Nitta, T., 1962: "The Outflow Boundary Condition in Numerical Time Integration of Advective Equations," J. Meteorol. Soc. Japan, Vol. 40, No. 1, pp. 13-24.

Platzman, G., 1958: "The Lattice Structure of the Finite-Difference Primitive and Vorticity Equations," Monthly Weather Review, Vol. 86, pp. 285-292.

Richtmyer, R. D., 1962: "A Survey of Difference Methods for Non-Steady Fluid Dynamics," NCAR Technical Notes, National Center for Atmospheric Research, Boulder, Colorado, 20 pp.

Shuman, F. G., 1960: "Numerical Experiments with the Primitive Equations," Proc. Int. Sym. NWP, Met. Sec. Jap., Tokyo: 1960, pp. 85-107.

_____, and J. B. Hovermale, 1968: "An Operational Six-Layer Primitive Equation Model," JAM, Vol. 7, pp. 525-547.

Wurtele, M. G., 1961: "On the Problem of Truncation Error," Tellus, Vol. 13, No. 3, pp. 379-391.

von Mises, R., 1958: Mathematical Theory of Compressible Fluid Flow, New York: Academic Press, 514 pp.

Appendix A: Linear Analysis of Centered Differences in Time and Space

The differential equations governing gravitational motion with zero mean velocity are

$$\frac{\partial u}{\partial t} + g\frac{\partial h}{\partial x} = 0 \tag{A-1}$$

and

$$\frac{\partial h}{\partial t} + H\frac{\partial u}{\partial x} = 0. \tag{A-2}$$

Using centered-difference approximations to both temporal and spatial derivatives yields the set of difference equations

$$u_j^{n+1} = u_j^{n-1} - \frac{g\Delta t}{\Delta x}(h_{j+1}^n - h_{j-1}^n) \tag{A-3}$$

and

$$h_j^{n+1} = h_j^{n-1} - \frac{H\Delta t}{\Delta x}(u_{j+1}^n - u_{j-1}^n) \tag{A-4}$$

The trial solutions are

$$u_j^n = u_0\zeta^n e^{ikj\Delta x},\ h_j^n = h_0\zeta^n e^{ikj\Delta x} \tag{A-5}$$

where $\zeta^n = R^n e^{in\varphi}$, $R = \left\{\left[R_e(\zeta)\right]^2 + \left[\mathrm{Im}(\zeta)\right]^2\right\}^{1/2}$, and $\varphi = \sin^{-1}\left\{\frac{\mathrm{Im}(\zeta)}{R}\right\}$.

Substitution of (A-5) into (A-3) and (A-4) leads to

$$(\zeta^2 - 1)u_0 + (2i\zeta\frac{g\Delta t}{\Delta x}\sin(k\Delta x))h_0 = 0 \tag{A-6}$$

and

$$(2i\zeta\frac{H\Delta t}{\Delta x}\sin(k\Delta x))u_0 + (\zeta^2 - 1)h_0 = 0. \tag{A-7}$$

The determinant of the system (A-6) and (A-7) is the frequency equation,

$$\left[\zeta^2 - 1\right]^2 + \left[2\zeta\frac{\sqrt{gH}\Delta t}{\Delta x}\sin(k\Delta x)\right]^2 = 0, \tag{A-8}$$

or

$$\zeta^2 - 1 = \pm 2 i \zeta \sqrt{gH} \frac{\Delta t}{\Delta x} \sin(k\Delta x) \tag{A-9}$$

Solving for ζ,

$$\zeta = \mp i\sqrt{gH} \frac{\Delta t}{\Delta x} \sin(k\Delta x) \pm \sqrt{1 - gH \left(\frac{\Delta t}{\Delta x}\right)^2 \sin^2(k\Delta x)}. \tag{A-10}$$

The amplification factor is

$$R^2 = 1 - gH \left(\frac{\Delta t}{\Delta x}\right)^2 \sin^2(k\Delta x) + gH \left(\frac{\Delta t}{\Delta x}\right)^2 \sin^2(k\Delta x) = 1, \tag{A-11}$$

so that the centered-time, centered-space scheme neither amplifies nor damps so long as the linear stability criterion $\sqrt{gH}\left(\frac{\Delta t}{\Delta x}\right) < 1$ is satisfied. The numerical phase angle φ is

$$\varphi = \sin^{-1}\left[\pm \sqrt{gH}\left(\frac{\Delta t}{\Delta x}\right) \sin k\Delta x\right]. \tag{A-12}$$

It is convenient to normalize this result by the analytic phase angle $\varphi_A = kc\Delta t$, so that the ratio φ/φ_A represents a measure of the numerical phase error. This ratio is plotted as ordinate against the product $(k\Delta x)$ in abscissa in figure A-1, for several values of the computational stability ratio $\sqrt{gH}(\Delta t/\Delta x)$. The figure shows that, so long as the linear stability criterion is satisfied, this differencing system always tends to move waves more slowly than their analytic phase velocity.

Appendix B: Linear Analysis of Euler-Backward Time Integration Combined with Centered-Space Differences

Again, the differential equations governing gravitational motion with zero mean velocity are

$$\frac{\partial u}{\partial t} + g\frac{\partial h}{\partial x} = 0 \tag{B-1}$$

and

$$\frac{\partial h}{\partial t} + H\frac{\partial u}{\partial x} = 0 \tag{B-2}$$

With centered differences in space, the first step of the Euler-backward scheme is

$$u_j^* = u_j^n - \frac{g\Delta t}{2\Delta x}(h_{j+1}^n - h_{j-1}^n) \tag{B-3}$$

and

$$h_j^* = h_j^n - \frac{H\Delta t}{2\Delta x}(u_{j+1}^n - u_{j-1}^n) \tag{B-4}$$

The second step is

$$u_j^{n+1} = u_j^n - \frac{g\Delta t}{2\Delta x}(h_{j+1}^* - h_{j-1}^*) \tag{B-5}$$

and

$$h_j^{n+1} = h_j^n - \frac{H\Delta t}{2\Delta x}(u_{j+1}^* - u_{j-1}^*). \tag{B-6}$$

Combining (B-3) and (B-4) with (B-5) and (B-6), we get, after rearranging,

$$u_j^{n+1} = u_j^n - \frac{g\Delta t}{2\Delta x}(h_{j+1}^n - h_{j-1}^n) + \left(\frac{\sqrt{gH}\,\Delta t}{2\Delta x}\right)^2 (u_{j+2}^n + u_{j-2}^n - 2u_j^n) \tag{B-7}$$

and

$$h_j^{n+1} = h_j^n - \frac{H\Delta t}{2\Delta x}(u_{j+1}^n - u_{j-1}^n) + \left(\frac{\sqrt{gH}\Delta t}{2\Delta x}\right)^2 (h_{j+2}^n + h_{j-2}^n - 2h_j^n). \tag{B-8}$$

Substituting the trial solutions

$$u_j^n = u_0\, \zeta^n e^{ik\Delta x},\ h_j^n = h_0\, \zeta^n e^{ikj\Delta x} \tag{B-9}$$

into (B-7) and (B-8) leads to the expressions

$$\left[\zeta - 1 - (gH)\left(\frac{\Delta t}{\Delta x}\right)^2 \sin^2(k\Delta x)\right] u_0 + \left[i\,\frac{g\Delta t}{\Delta x}\ \sin(k\Delta x)\right] h_0 \tag{B-10}$$

and

$$\left[i\,\frac{H\Delta t}{\Delta x}\ \sin(k\Delta x)\right] u_0 + \left[\zeta - 1 - (gH)\left(\frac{\Delta t}{\Delta x}\right)^2 \sin^2(k\Delta x)\right] h_0. \tag{B-11}$$

The determinant of (B-10) and (B-11) is the frequency equation

$$\zeta = 1 \pm i\,\frac{\sqrt{gH}\,\Delta t}{\Delta x}\ \sin(k\Delta x) - \left[\frac{\sqrt{gH}\Delta t}{\Delta x}\ \sin(k\Delta x)\right]^2 . \tag{B-12}$$

From the frequency equation the amplification can be determined:

$$R = \left\{1 - \left[\frac{\sqrt{gH}\Delta t}{\Delta x}\ \sin(k\Delta x)\right]^2 + \left[\frac{\sqrt{gH}\Delta t}{\Delta x}\ \sin(k\Delta x)\right]^4\right\}^{1/2} . \tag{B-13}$$

It can be seen that, provided $\frac{\sqrt{gH}\Delta t}{\Delta x} < 1$, the Euler-backward technique is damping. The damping rate per time step is shown in figure (B-1) as a function of the product $(k\Delta x)$ and the stability ratio $\sqrt{gH}(\Delta t/\Delta x)$. The diagram shows that maximum damping occurs in the wave four grid intervals long for the stability ratio about seven-tenths. For greater stability ratios, the damping in this wavelength diminishes, and disappears for neutral stability, so that maximum damping occurs in two wavelengths. Figure B-2 shows accumulated damping after a number of time steps as a function of wavelength or period. Note that an oscillation of two-hour period is reduced to less than ten percent of its amplitude in 100 time steps, but an oscillation of a ten-hour period retains above 85% of its original amplitude after the same number of iterations.

Also from the frequency equation, the numerical phase angle φ can be computed:

$$\varphi = \sin^{-1}\left\{\left[\sqrt{gH}\left(\frac{\Delta t}{\Delta x}\right)\ \sin(k\Delta x)\right] / R\right\}. \tag{B-14}$$

Values of the ratio $\varphi/kc\Delta t$ are plotted in figure B-3 against wavelength for different stability ratios. For neutral stability, the Euler-backward in combination with centered-space differences is highly accelerative for medium-length waves down to the four-grid-interval wave. For shorter waves, the decelerative nature of the centered-space approximation is predominant.

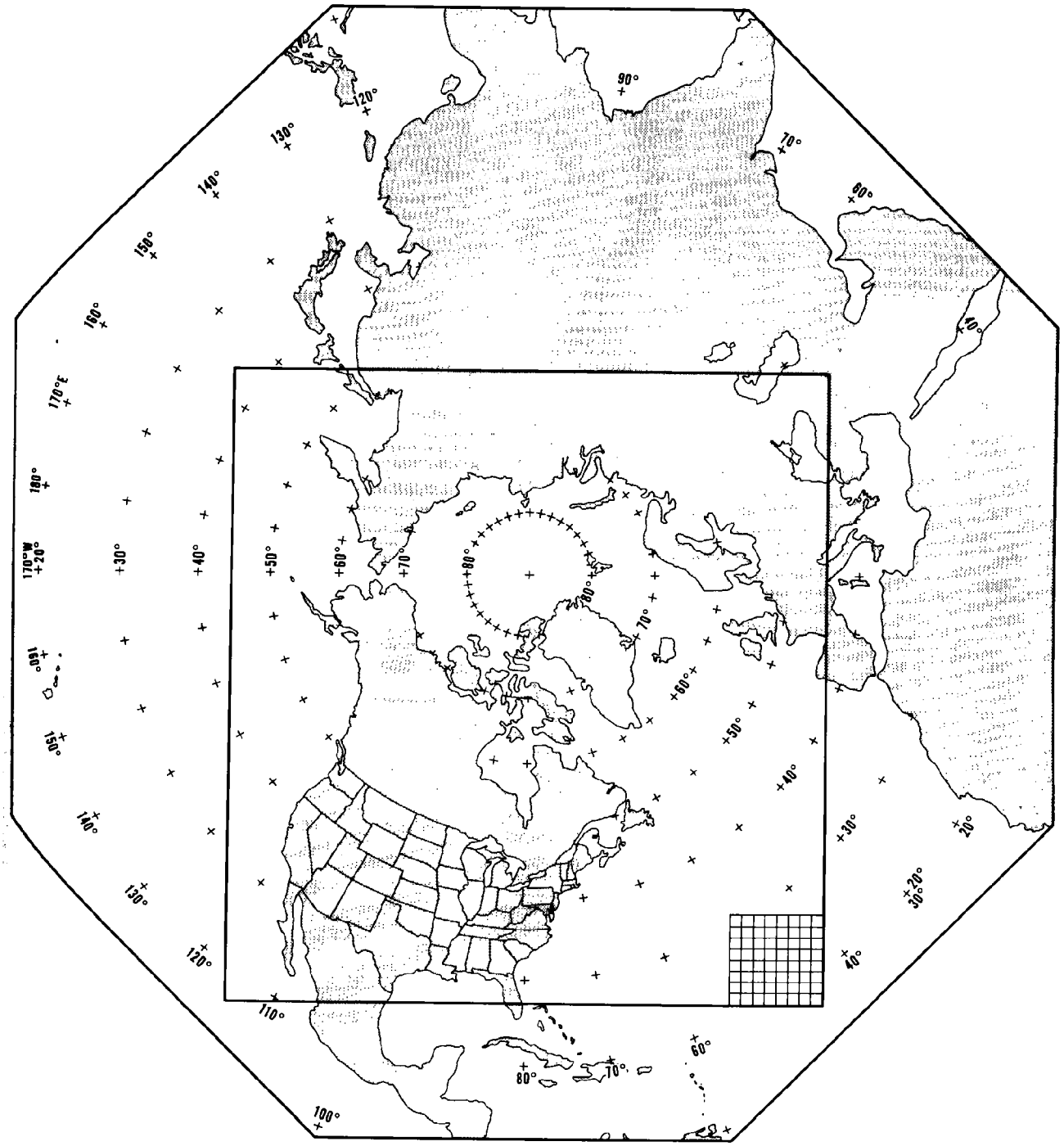

Figure 1.--Polar stereographic map of the Northern Hemisphere showing the octagon within which data was available. Also shown is the rectangular boundary of the limited-area, fine-mesh within which the model equations were solved. In the lower right corner of the rectangle a portion of the fine-mesh grid is illustrated.

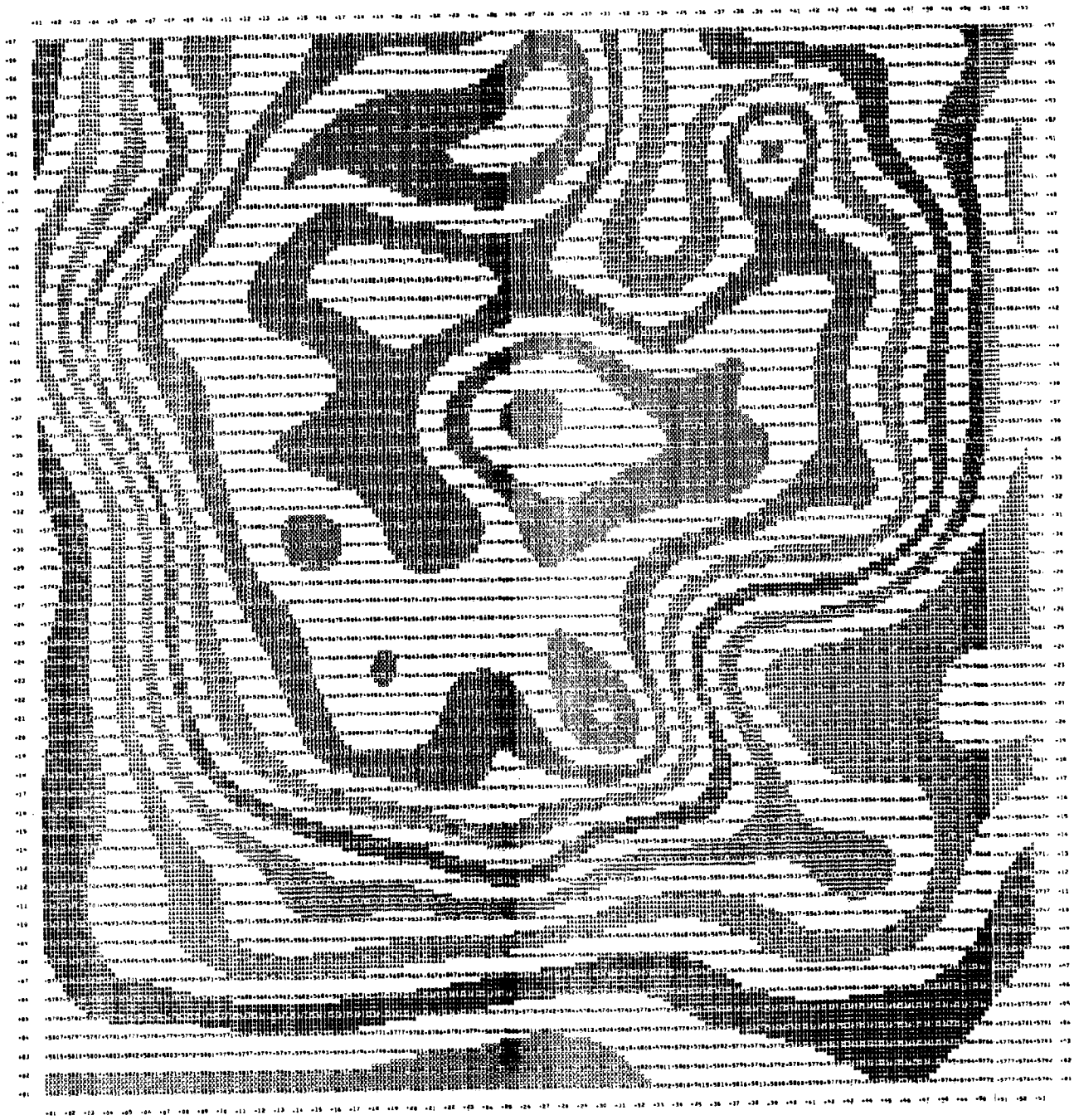

Figure 2.--500-mb height analysis on the limited-area, fine-mesh grid for 1 February 1969, 12Z.

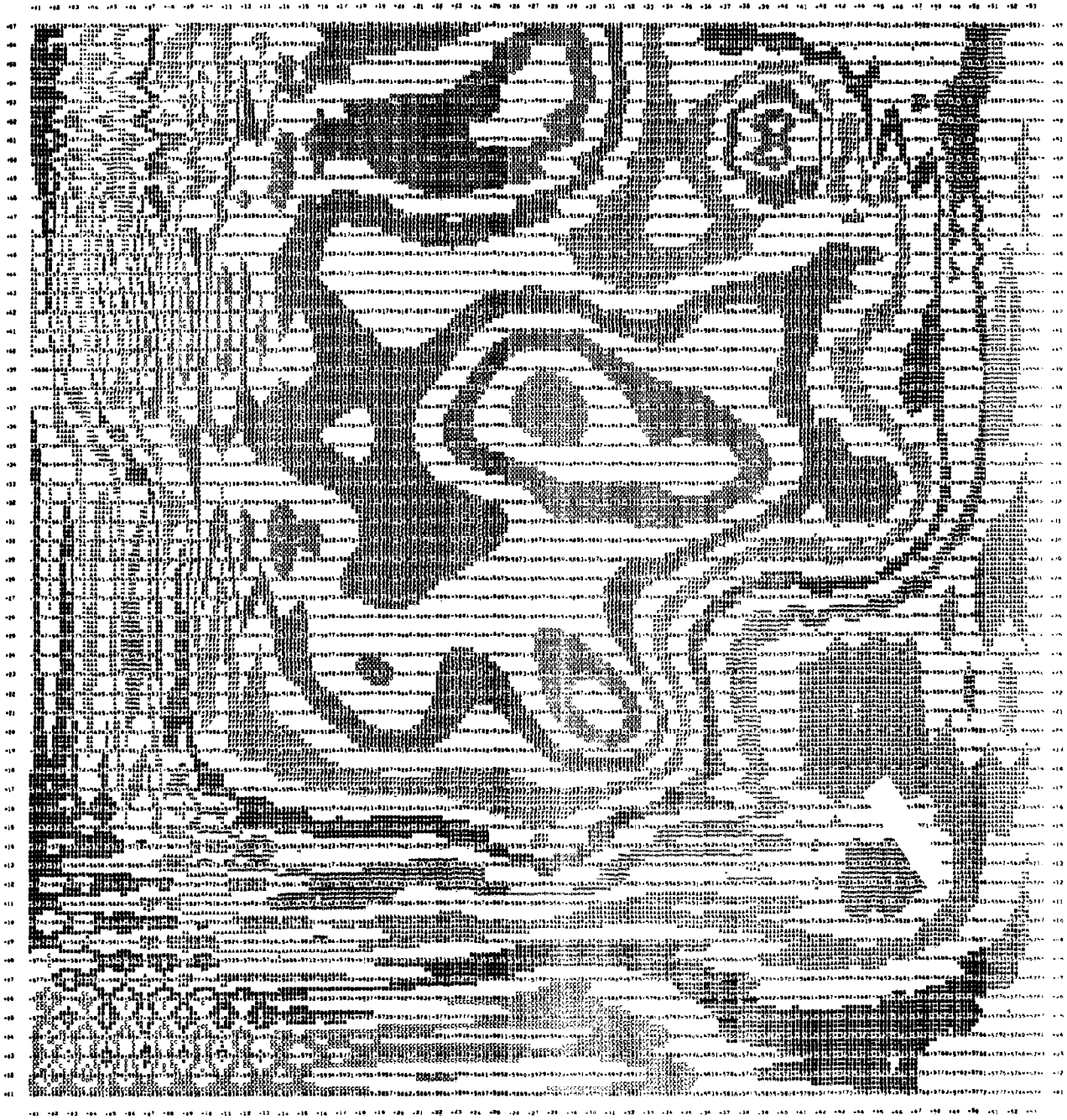

Figure 3.--Three-hour 500-mb height forecast based on the initial conditions in Figure 2 from the limited-area, fine-mesh, primitive equation barotropic model. The group of five underlined points refers to Figures 8-11.

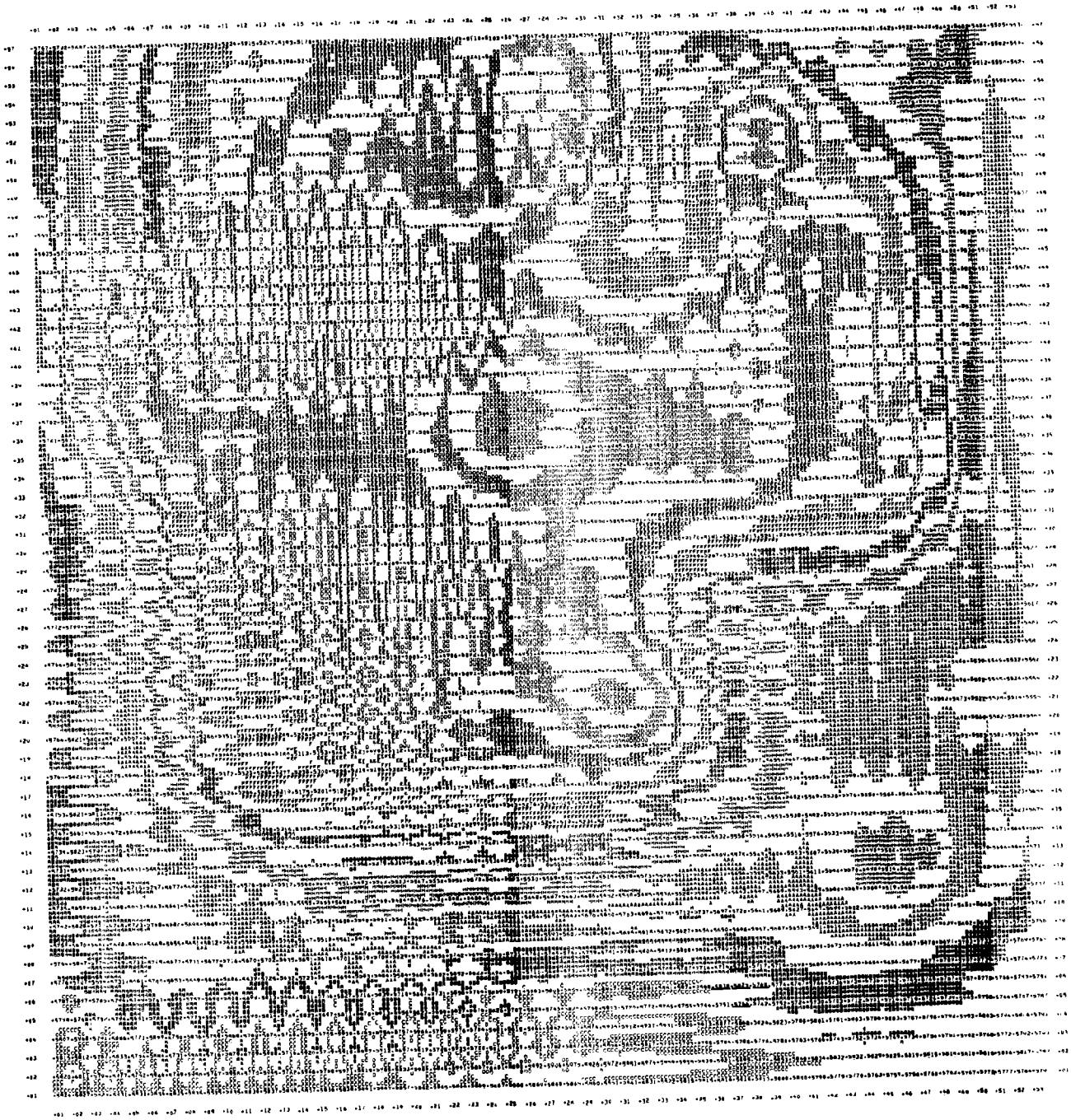

Figure 4.--Six-hour 500-mb height forecast based on the initial conditions in Figure 2 from the limited-area, fine-mesh, primitive equation barotropic model. The group of five underlined points refers to Figures 8-11.

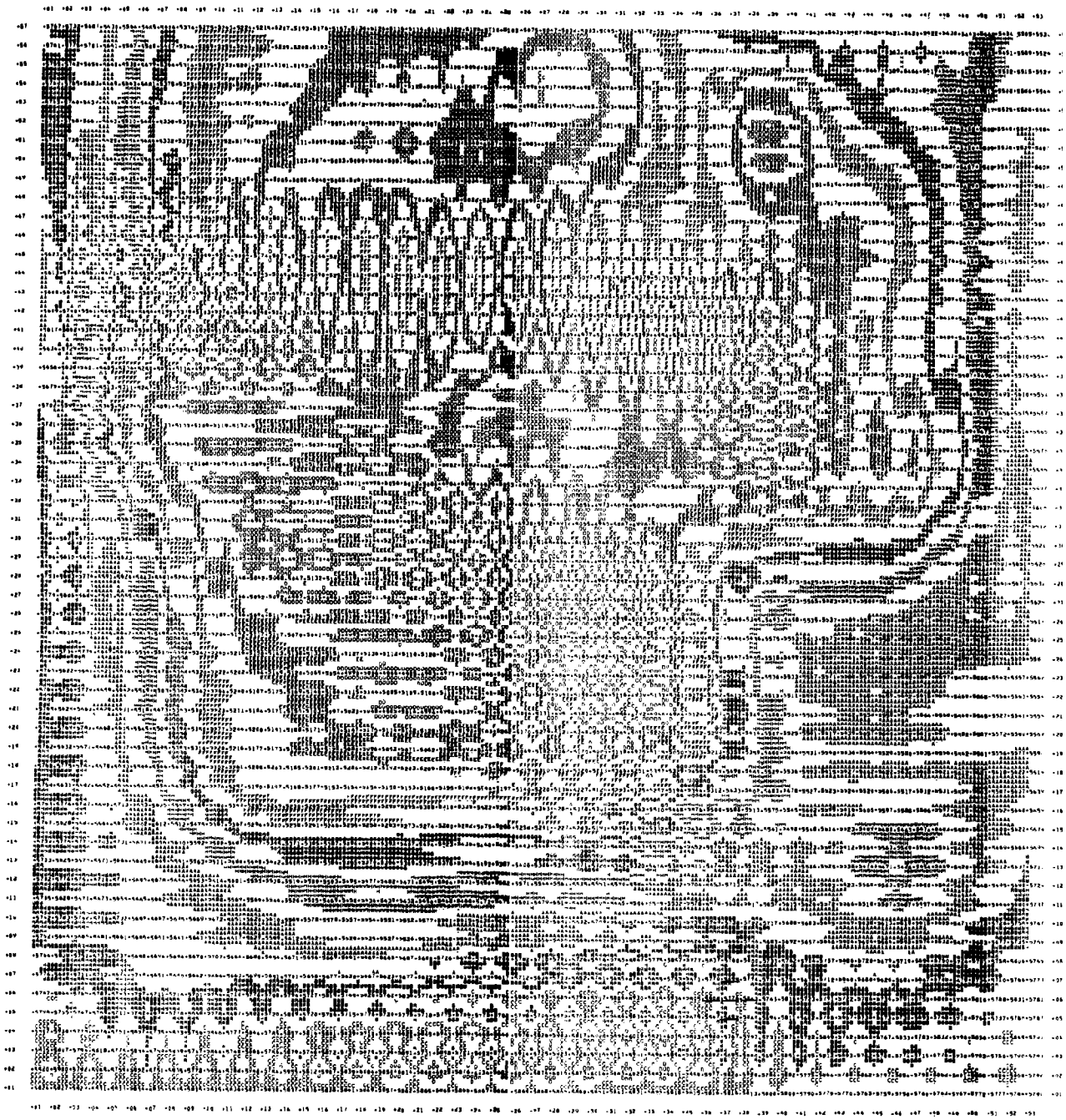

Figure 5.--Nine-hour 500-mb height forecast based on the initial conditions in Figure 2 from the limited-area, fine-mesh, primitive equation barotropic model. The group of five underlined points refers to Figures 8-11.

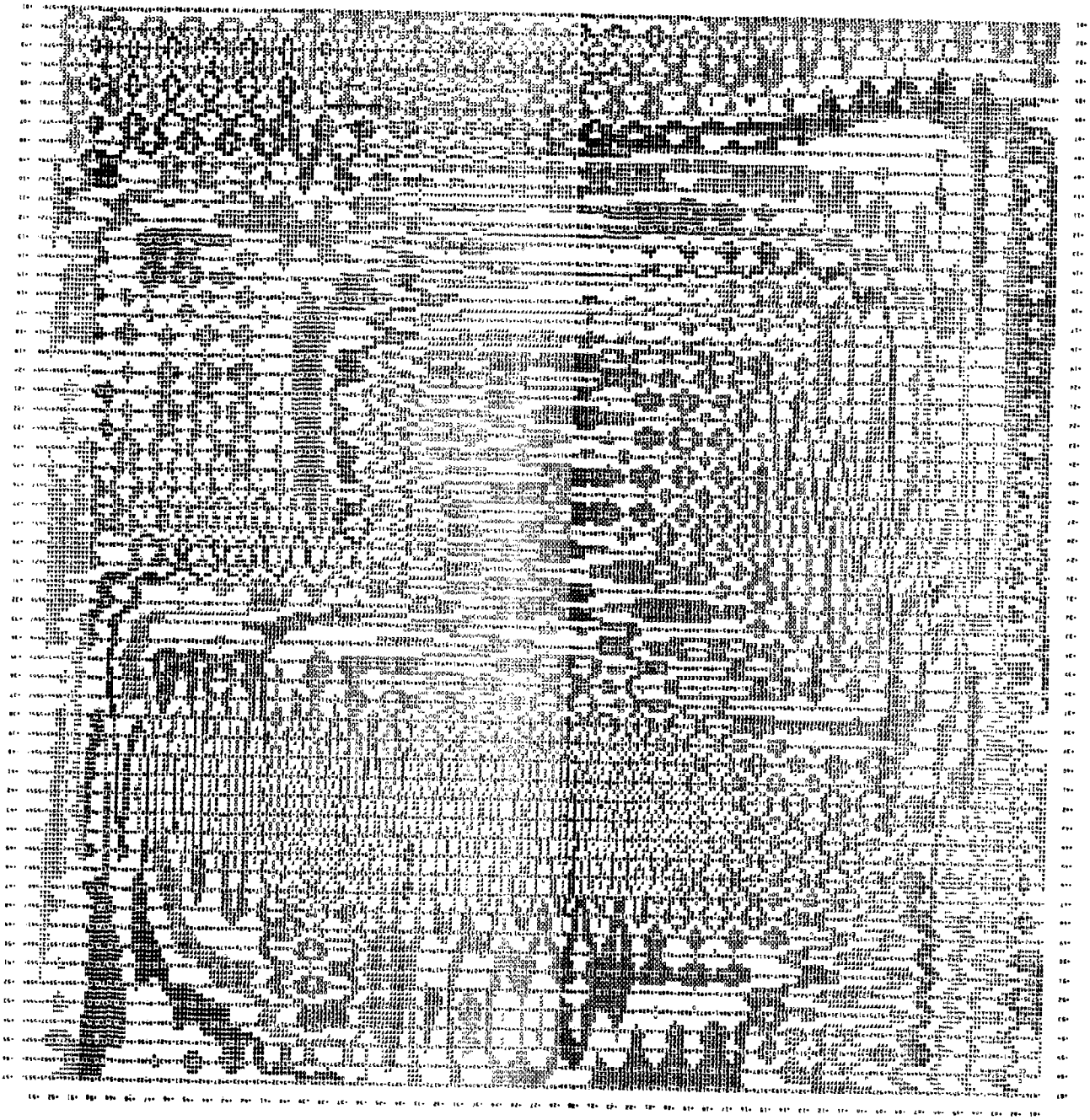

Figure 6.--Twelve-hour 500 mb height forecast based on the initial conditions in Figure 2 from the limited-area, fine-mesh, primitive equation barotropic model. The group of five underlined points refers to Figures 8-11.

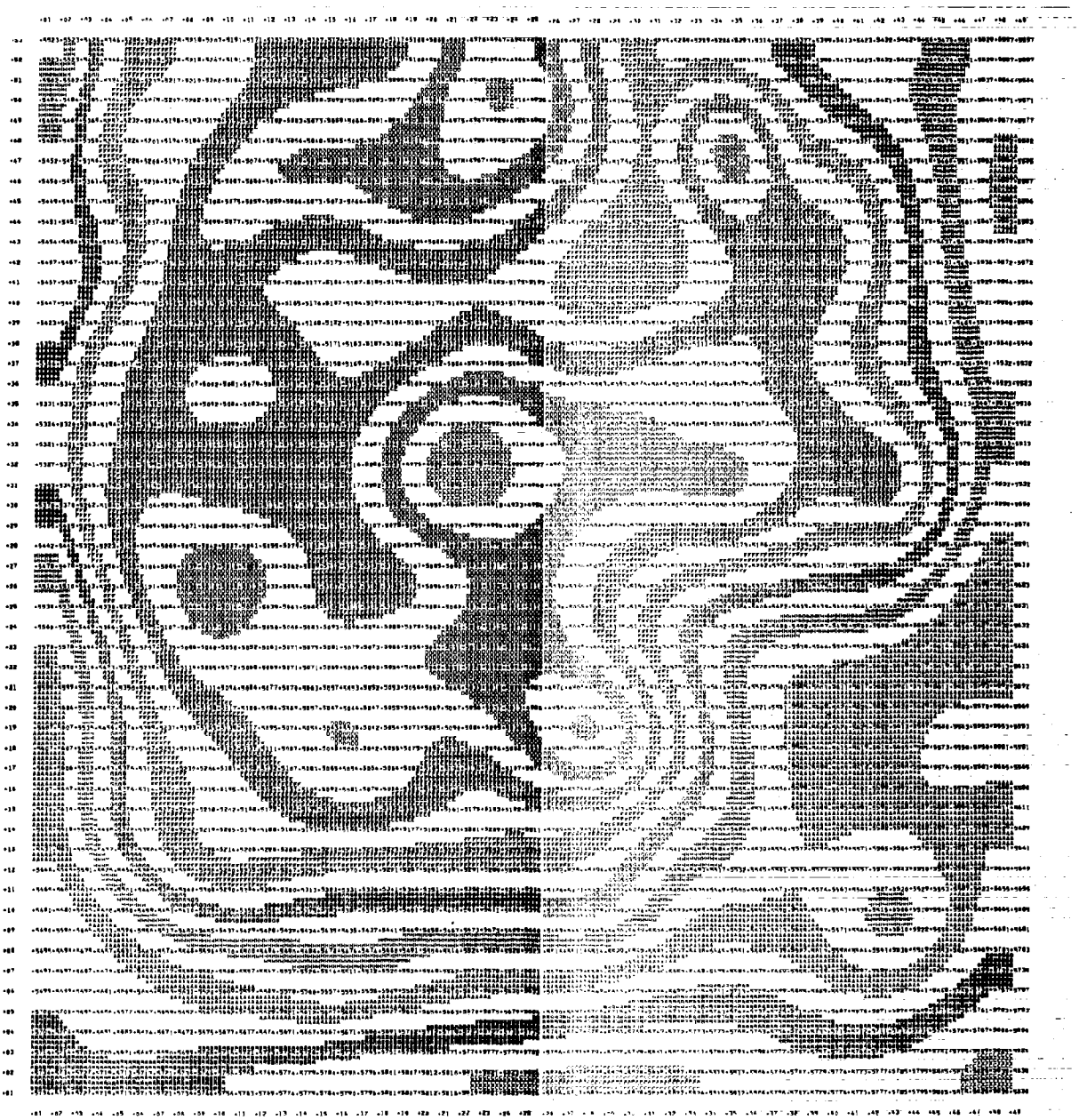

Figure 7.--Twelve-hour 500-mb forecast as in Figure 6, after passing a low-pass filter (Gerrity and McPherson, 1969) over the field prior to output.

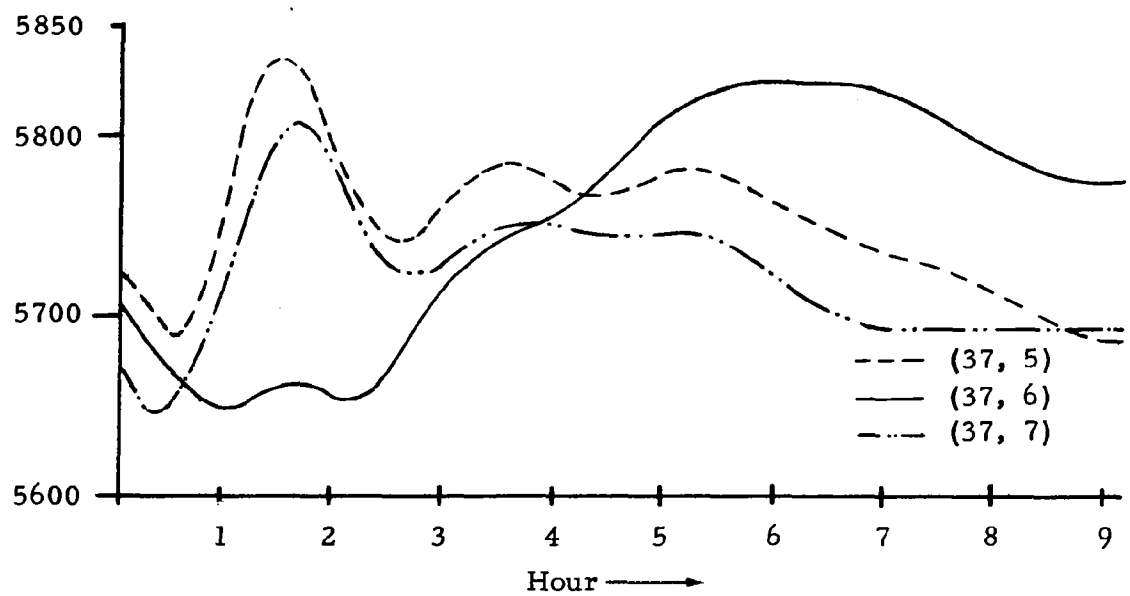

Figure 8.--500-mb height prior to filtering at each time step for points (37, 5), (37, 6), and (37, 7) underlined in Figures 3-6.

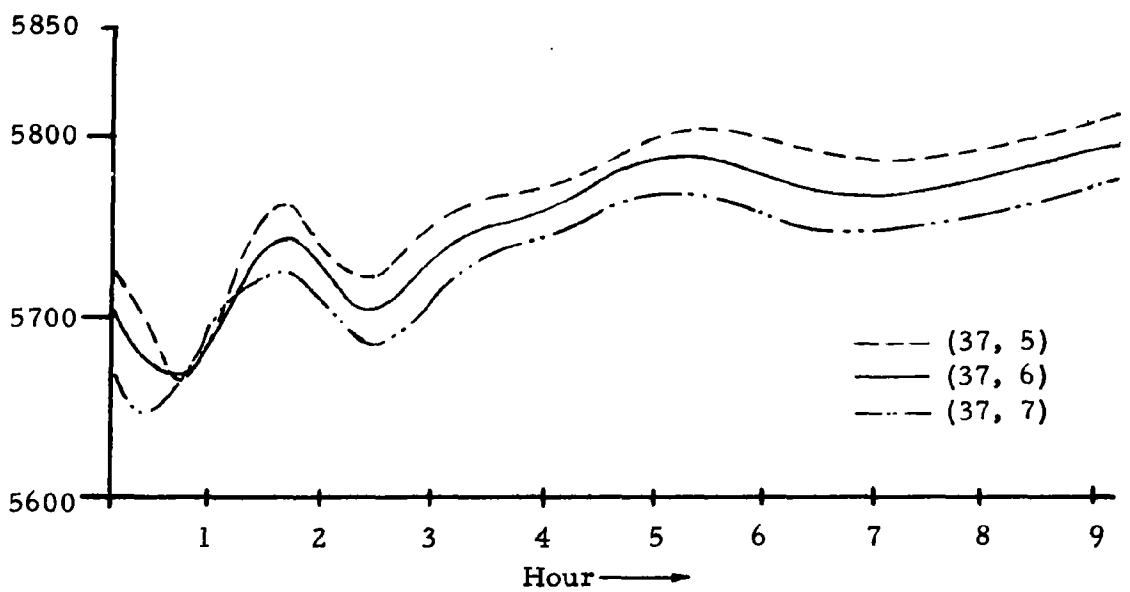

Figure 9.--500-mb height after filtering at each time-step for points (37, 5), (37, 6), and (37, 7) underlined in Figures 3-6.

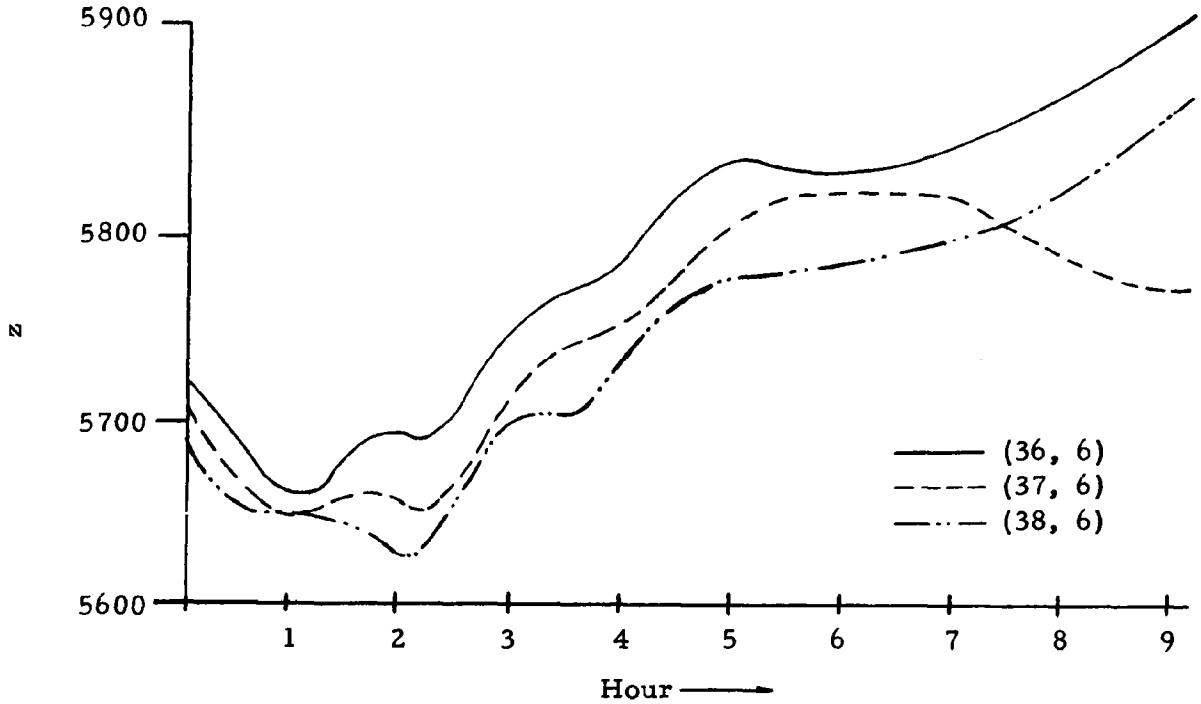

Figure 10.--500-mb height prior to filtering at each time step for points (36, 6), (37, 6), and (38, 6) underlined in Figures 3-6.

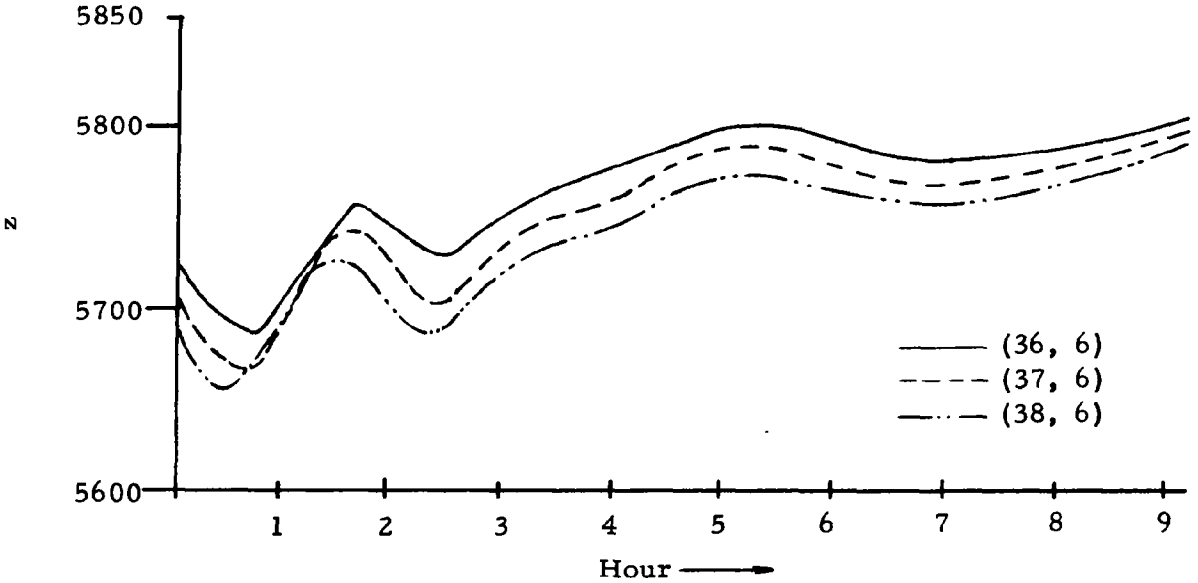

Figure 11.--500-mb height after filtering at each time step for points (36, 6), (37, 6), and (38, 6) underlined in Figures 3-6.

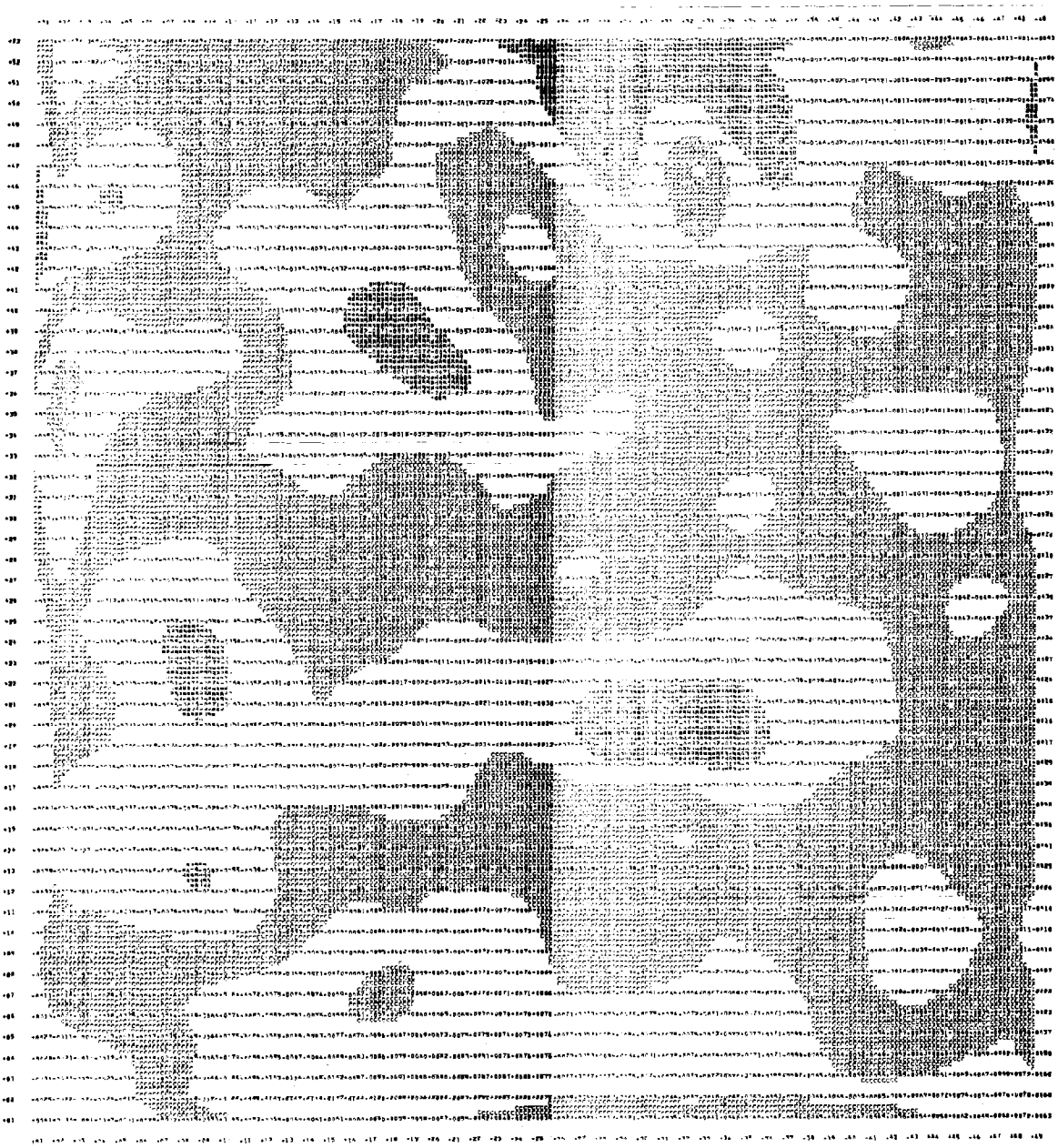

Figure 12.--Error associated with the 12-hour limited-area, fine-mesh forecast of the 500-mb height field, shown in Figure 7. The error is defined as the forecast value minus the observed value.

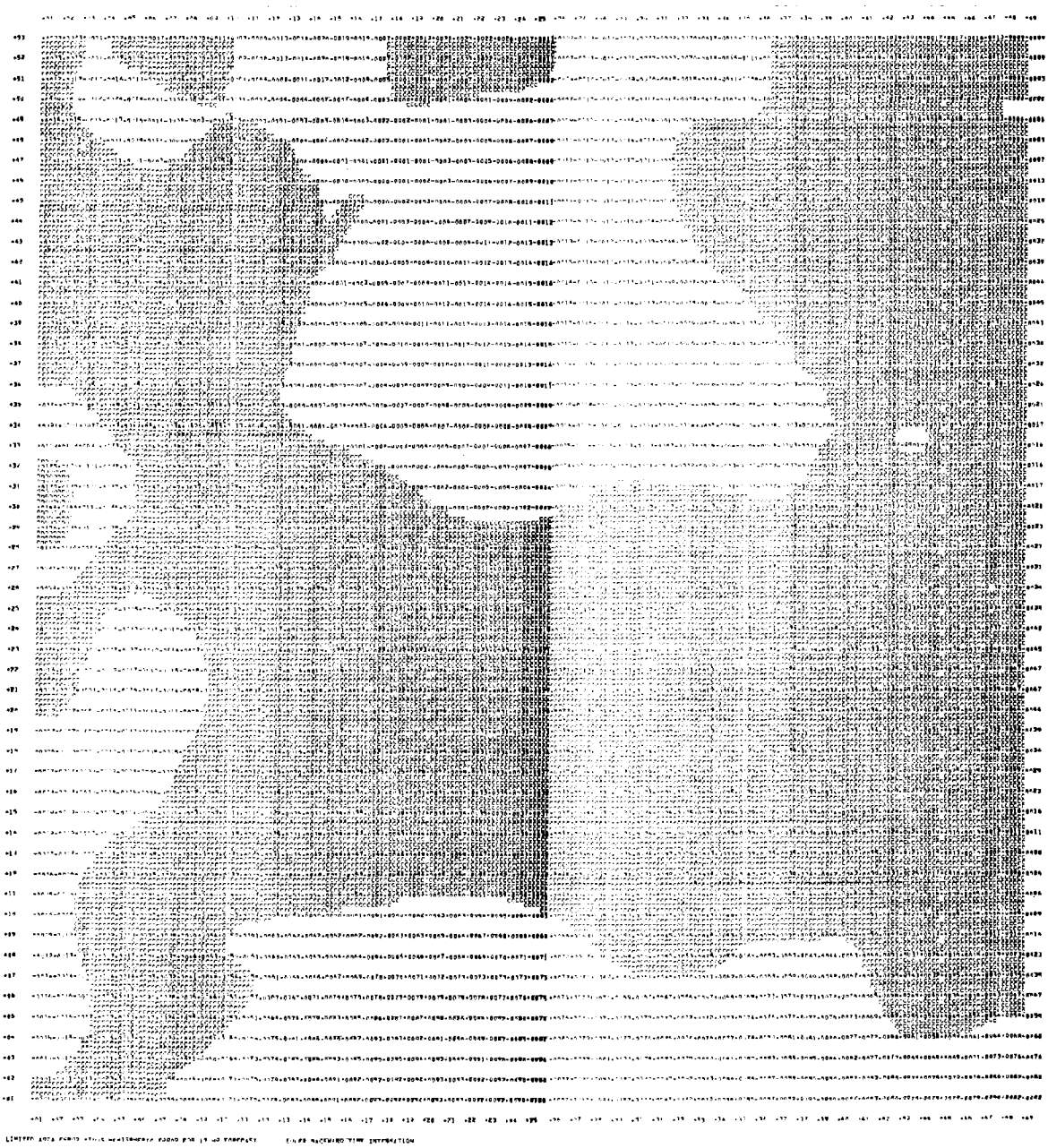

Figure 13.--Difference between the error field shown in Figure 12 and that associated with a 12-hour forecast from the identical fine-mesh primitive equation barotropic model integratied over the entire octagon shown in Figure 1.

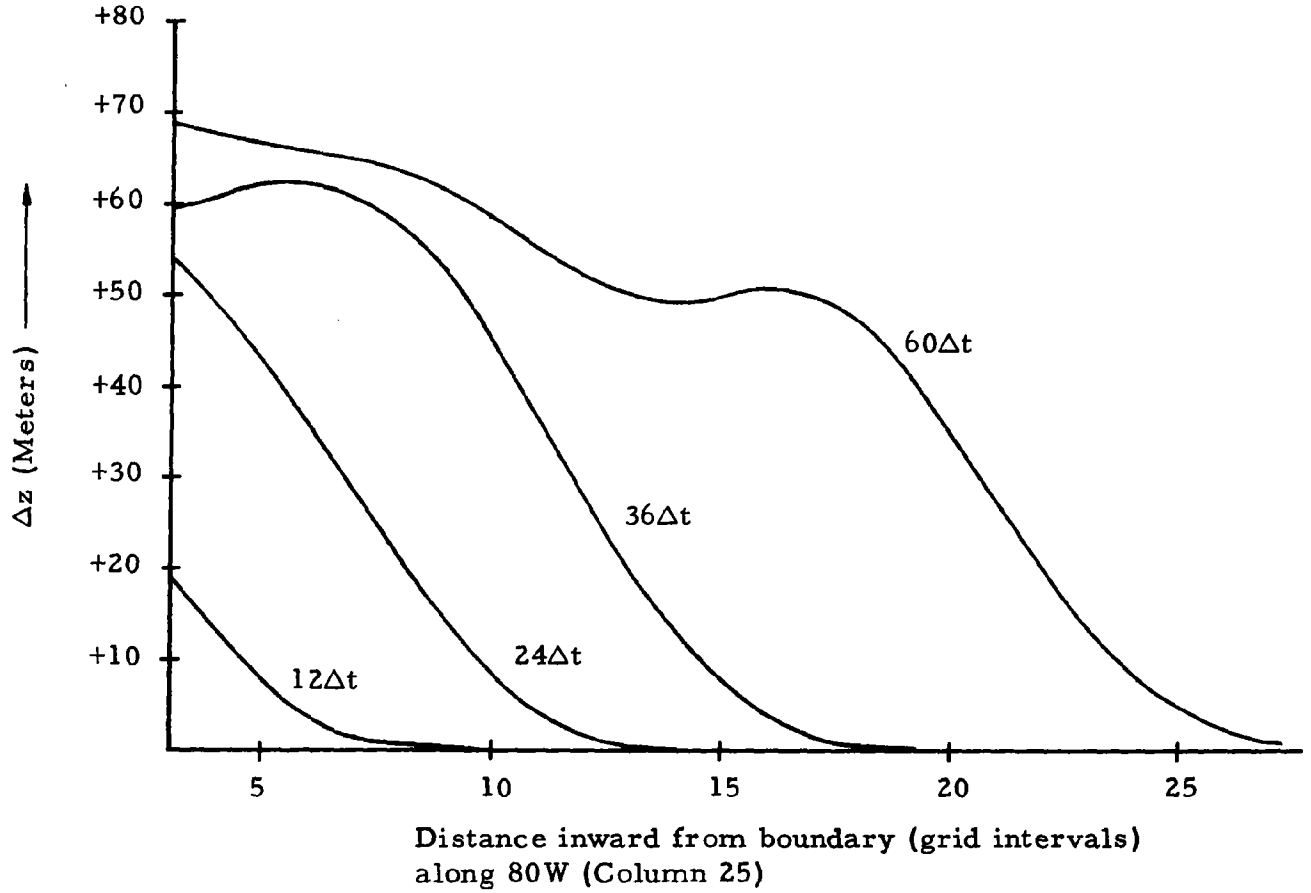

Figure 14.--Difference between the error fields associated with the forecasts from the limited-area and quasi-hemispheric fine-mesh models, displayed at one, two, three, and five hours along 80 W (column 25 of Figure 13).

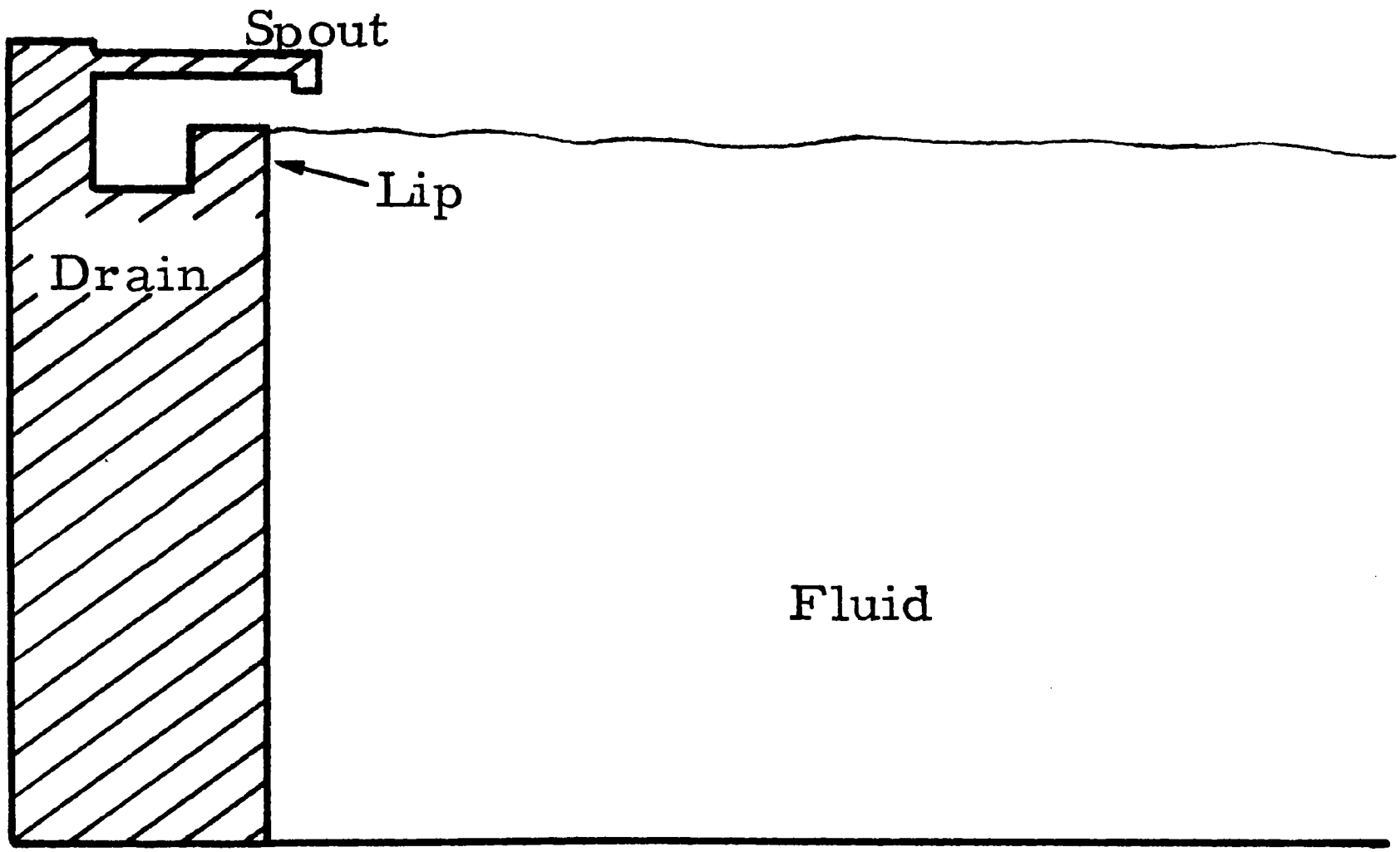

Figure 15.--Schematic illustrating the "swimming pool" physical analog of the mathematical one-dimensional simulation of the noise problem.

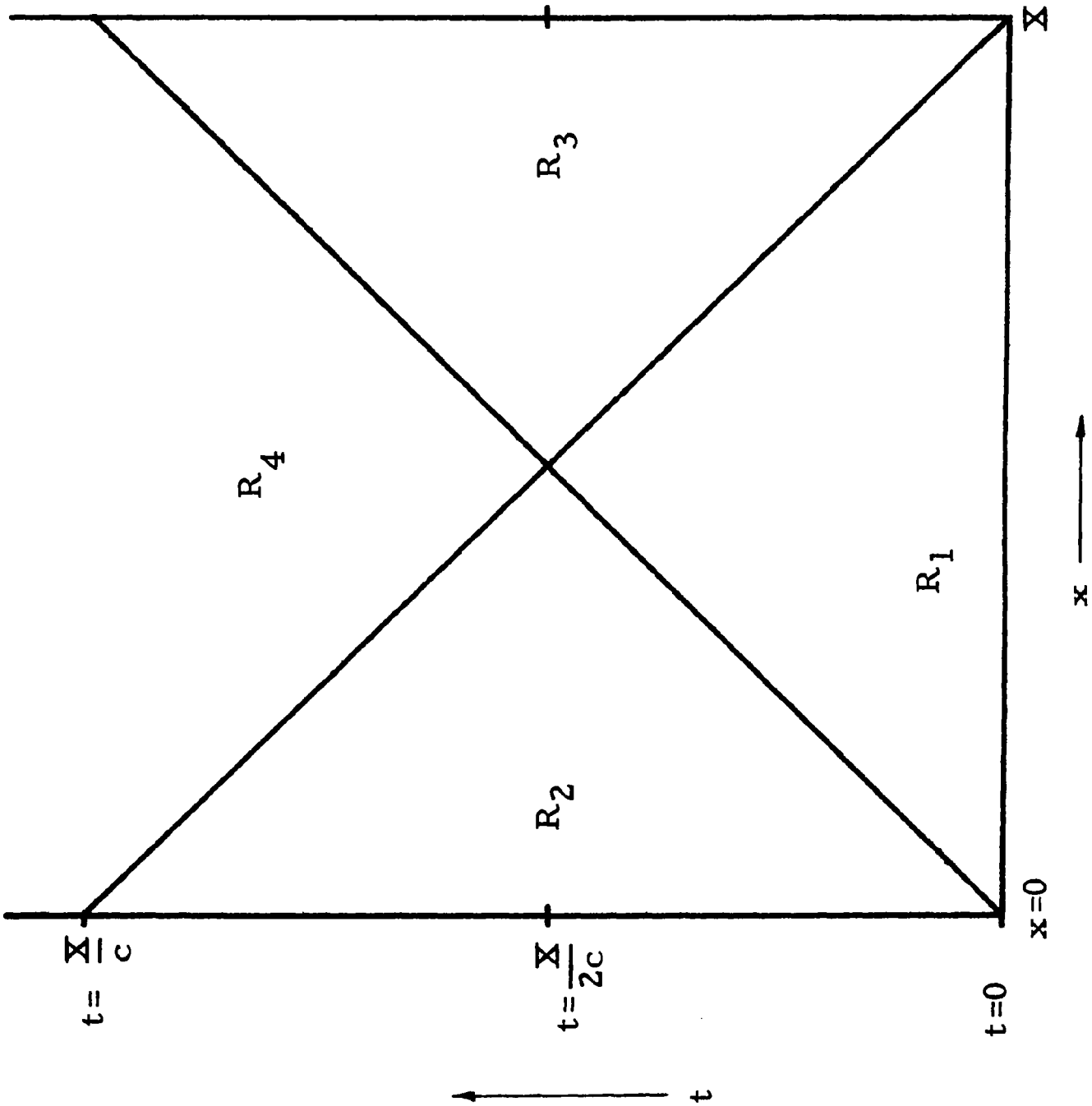

Figure 16.--Characteristic diagram illustrating the four regions of the analytic solution of the one-dimensional, constant-boundaries, linear gravity wave problem.

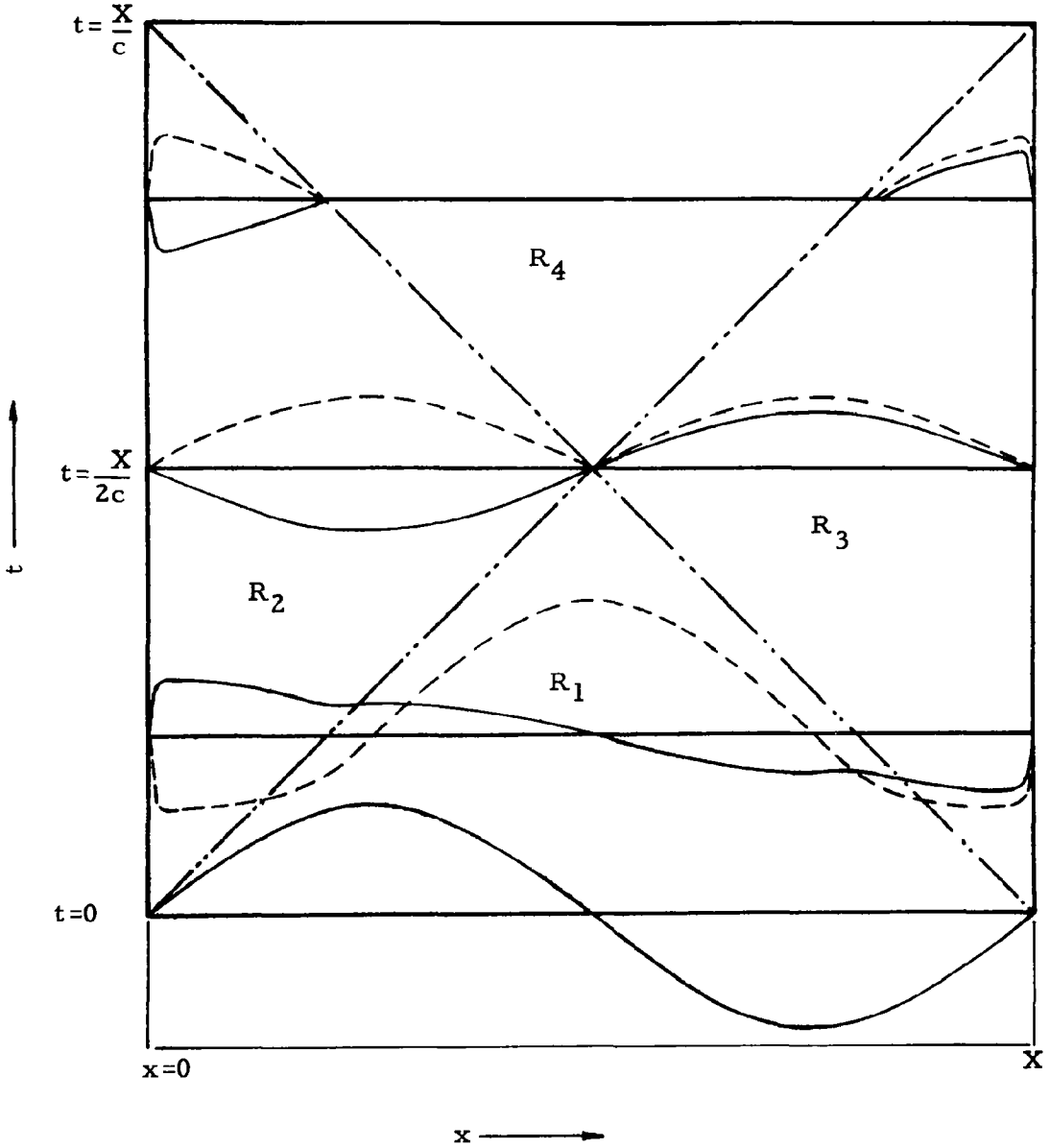

Figure 17.--Analytic solutions of the one-dimensional, constant boundaries, linear gravity wave problem, as obtained by the method of characteristics.

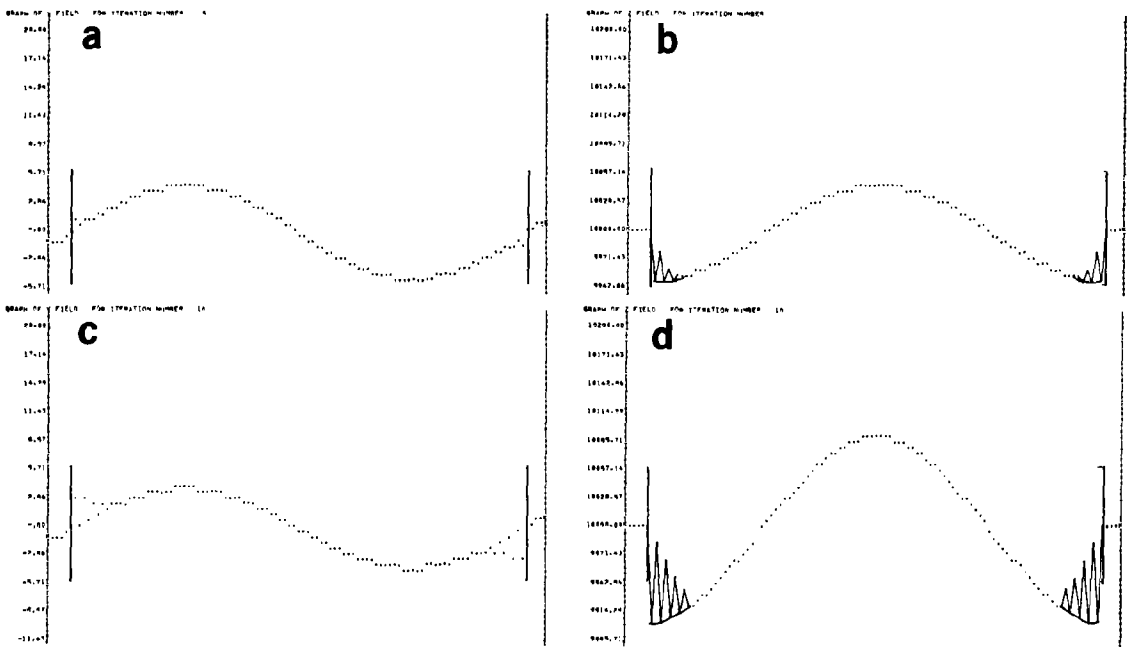

Figure 18.--Numerical solutions of the one-dimensional, constant-boundaries, linear gravity wave problem using centered differences in space and time. Solutions at each grid point are indicated by dots. The boundaries of the region of integration are denoted by short, solid, vertical lines. $(\sqrt{gH})\Delta t/\Delta x=1$.

a, b: velocity and height, respectively, at time step 5;
c, d: velocity and height, respectively, at time step 10.

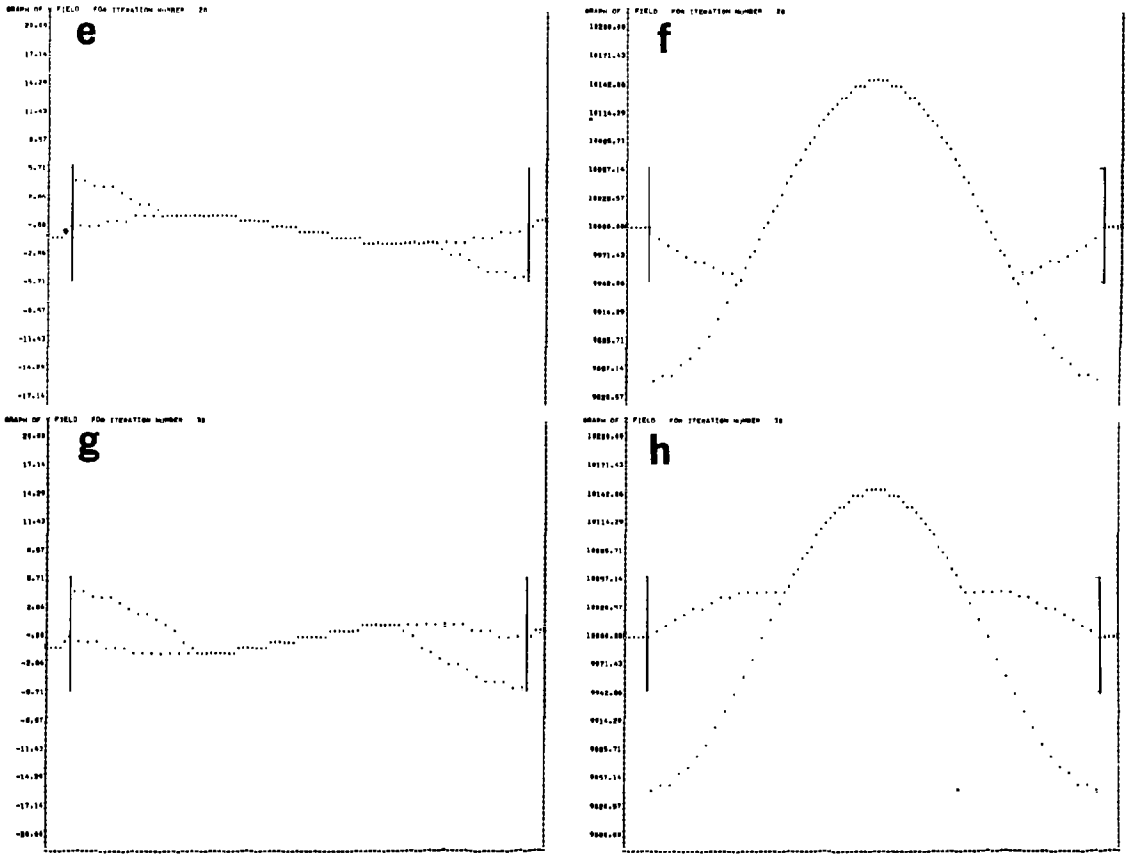

Figure 18.--(continued). Numerical solutions of the one-dimensional, constant-boundaries, linear gravity wave problem using centered differences in space and time. Solutions at each grid point are indicated by dots. The boundaries of the region of integration are denoted by short, solid, vertical lines. $(\sqrt{gH})\Delta t/\Delta x=1$.

e, f: velocity and height, respectively, at time step 20;
g, h: velocity and height, respectively, at time step 30.

149 440

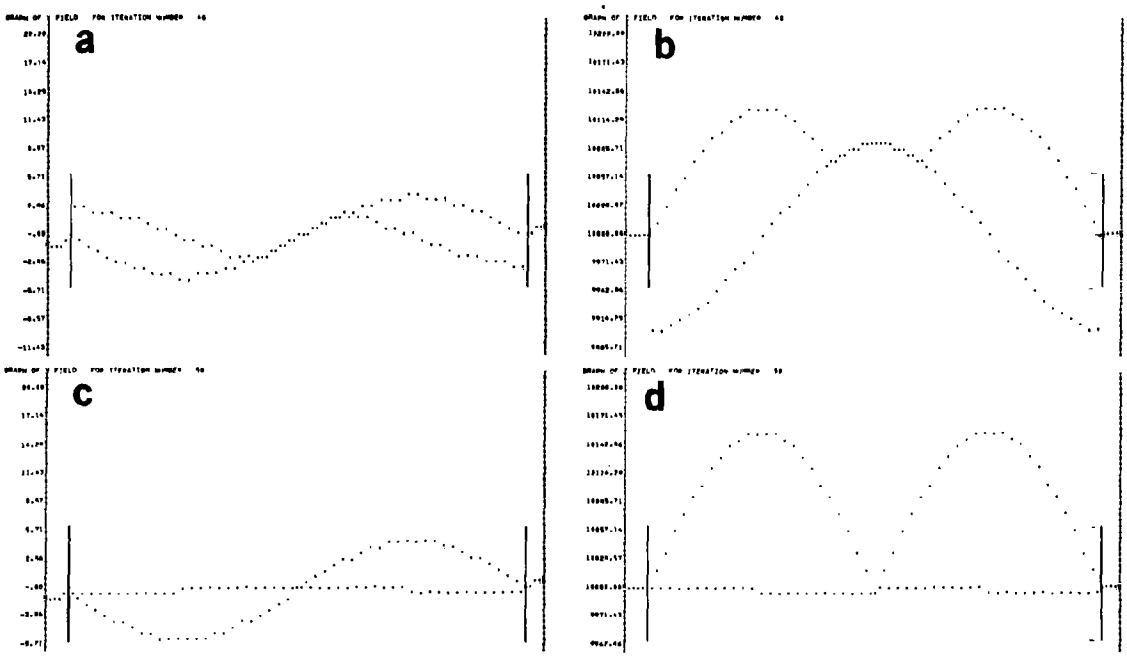

Figure 19.--Numerical solutions of the one-dimensional, constant boundaries, linear gravity wave problem using centered differences in space and time. Solutions at each grid point are indicated by dots. The boundaries of the region of integration are denoted by short, solid, vertical lines. $(\sqrt{gH})\Delta t/\Delta x=1$.

a, b: velocity and height, respectively, at time step 40;
c, d: velocity and height, respectively, at time step 50.

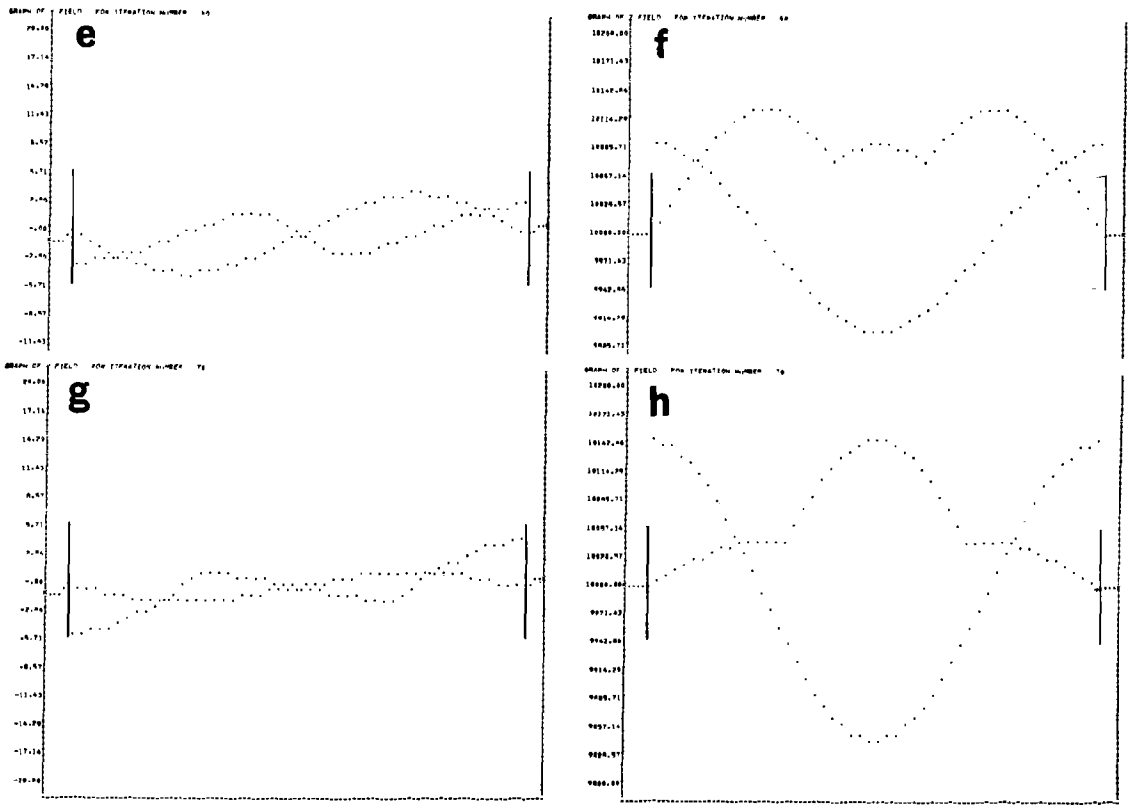

Figure 19.--(continued). Numerical solutions of the one-dimensional, constant boundaries, linear gravity wave problem using centered differences in space and time. Solutions at each grid point are indicated by dots. The boundaries of the region of integration are denoted by short, solid, vertical lines.

$(\sqrt{gH})\Delta t/\Delta x=1.$

e, f: velocity and height, respectively, at time step 60;
g, h: velocity and height, respectively, at time step 70.

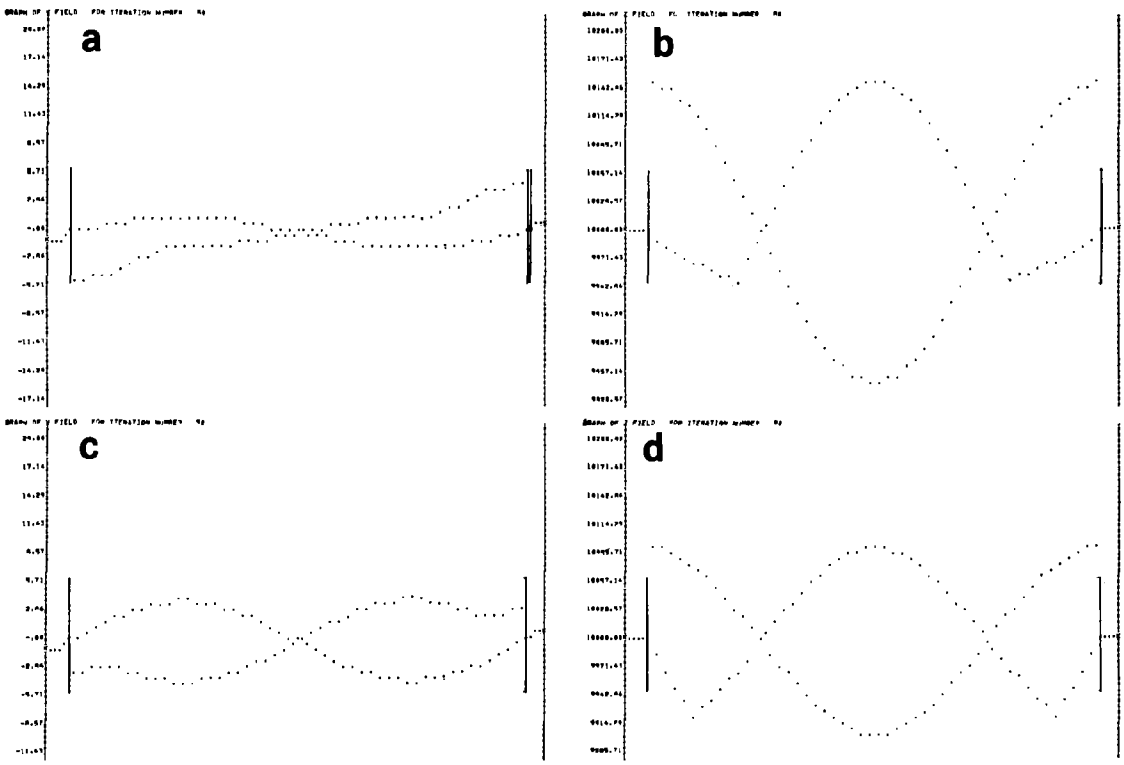

Figure 20.--Numerical solutions of the one-dimensional, constant-boundaries, linear gravity wave problem using centered differences in space and time. Solutions at each grid point are indicated by the dots. The boundaries of integration are denoted by short, solid, vertical lines. $(\sqrt{gH})\Delta t/\Delta x=1$.

a, b: velocity and height, respectively, at time step 80;
c, d: velocity and height, respectively, at time step 90.

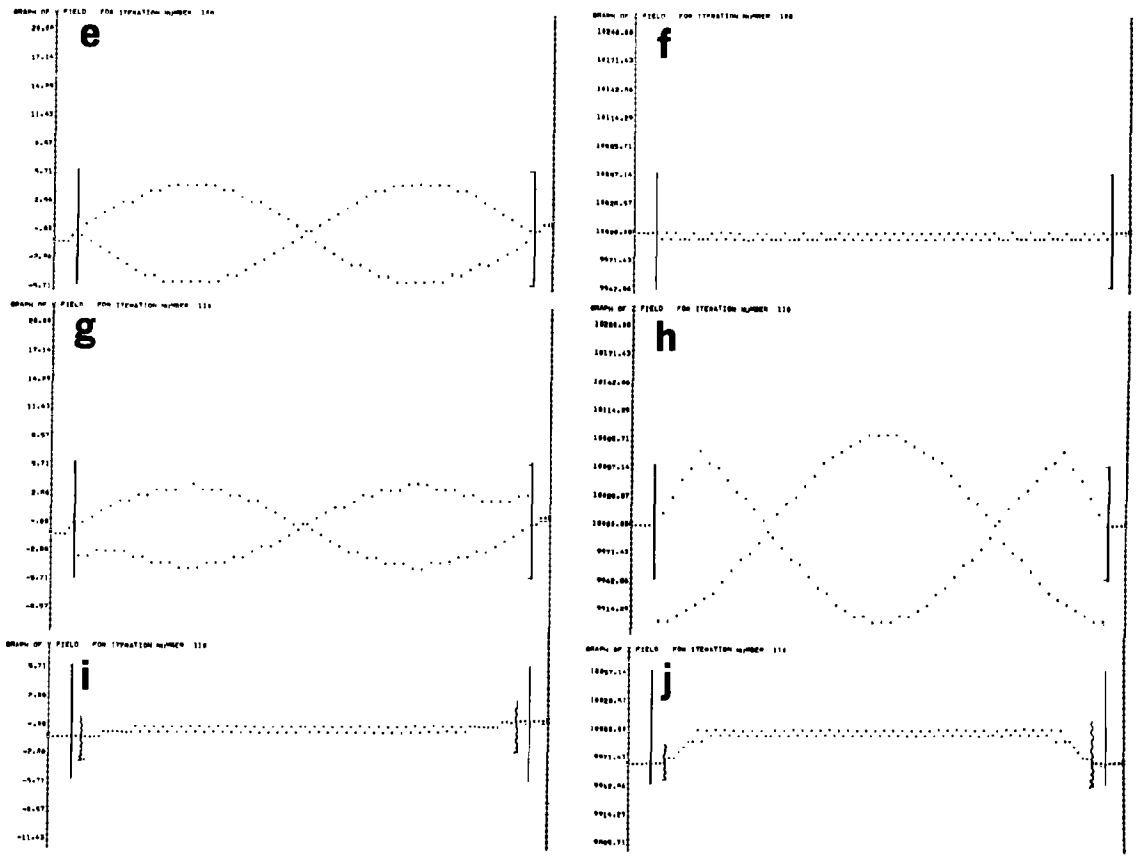

Figure 20.--(continued). Numerical solutions of the one-dimensional, constant boundaries, linear gravity wave problem using centered differences in space and time. Solutions at each grid point are indicated by the dots. The boundaries of the region of integration are denoted by short, solid, vertical lines. $(\sqrt{gH})\Delta t/\Delta x=1$.

e, f: velocity and height, respectively, at time step 100;
g, h: velocity and height, respectively, at time step 110;
i, j: velocity and height, respectively, at time step 110, after filtering with the one-dimensional version of the filter described by Gerrity and McPherson(1969).

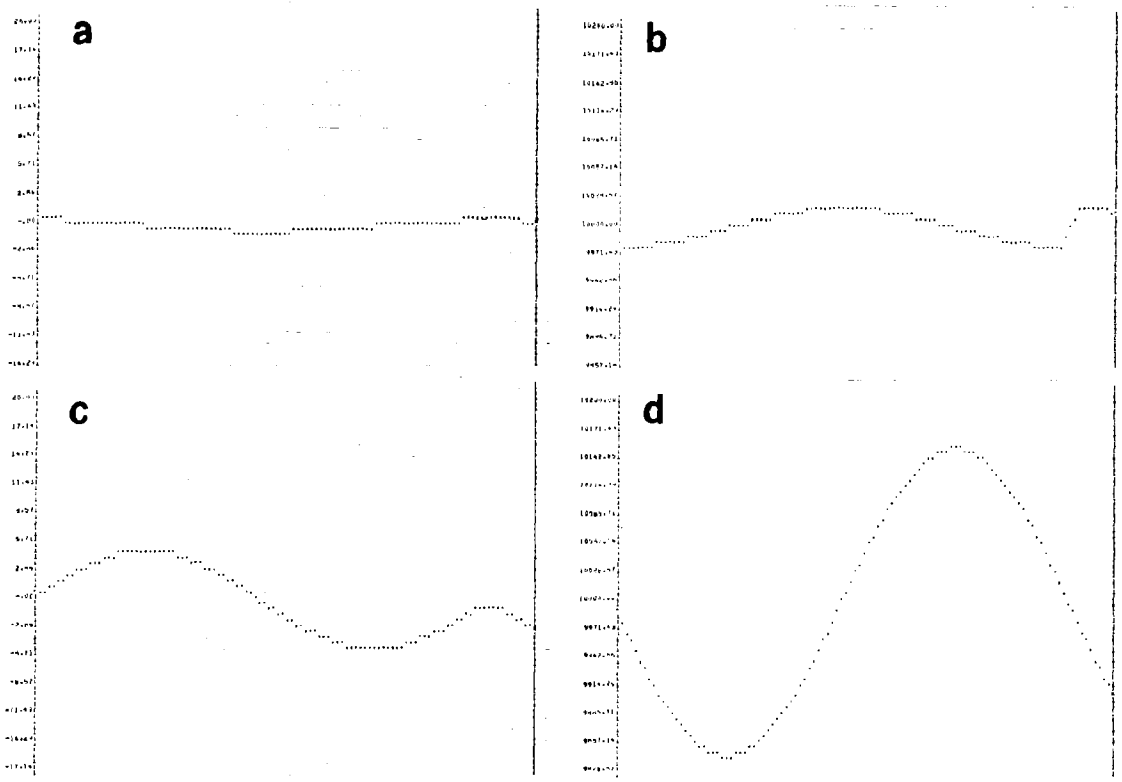

Figure 21.--Numerical solutions of the one-dimensional, constant-boundaries, linear gravity wave problem using centered differences in space and time. Solutions are obtained at each time step.
a, b: velocity and height, respectively, at grid point 5;
c, d: velocity and height, respectively, at grid point 6;

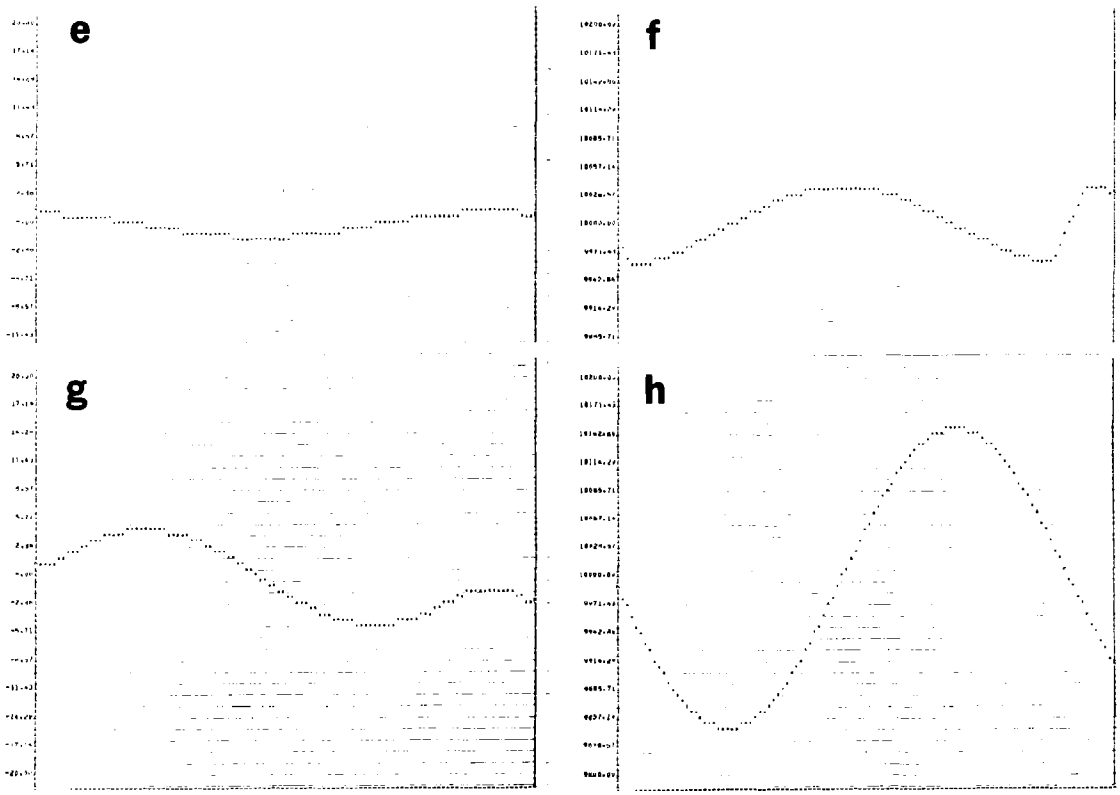

Figure 21.--(continued). Numerical solutions of the one-dimensional, constant-boundaries, linear gravity wave problem using centered differences in space and time. Solutions are displayed at each time step.
e, f: velocity and height, respectively, at grid point 7;
g, h: velocity and height, respectively, at grid point 8.

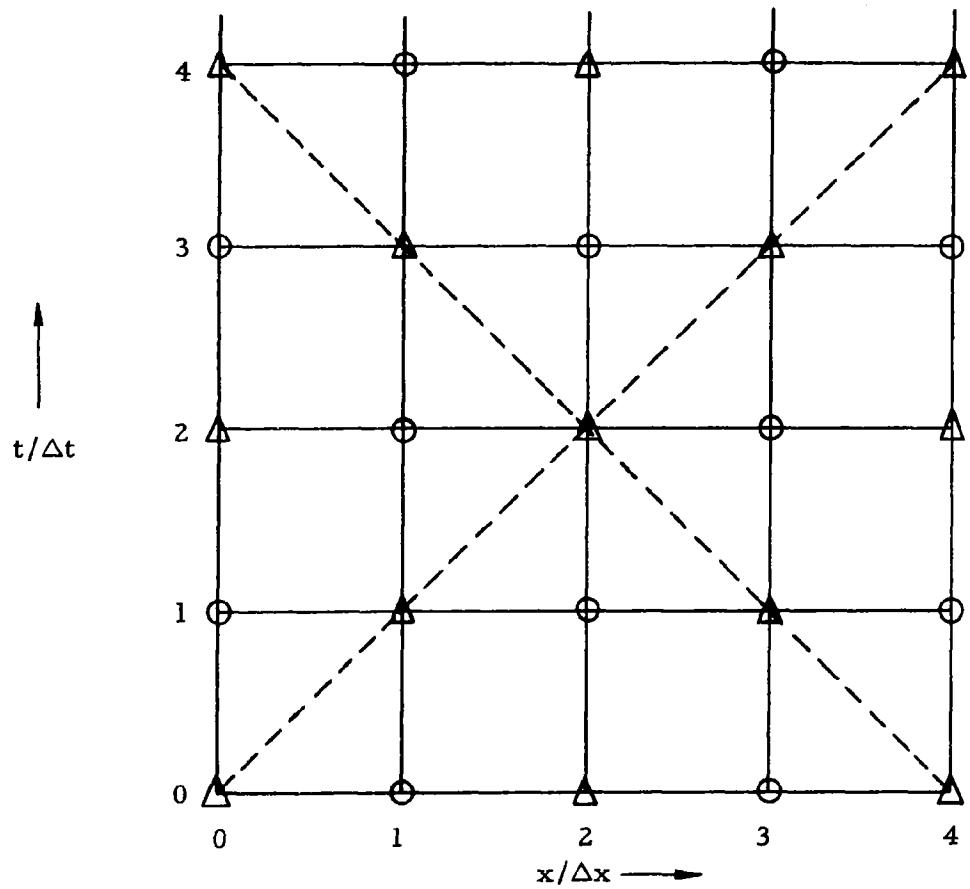

Figure 22.--Schematic illustrating the lattice structure of the grid used in centered space-time differencing. Points denoted by circles constitute one complete lattice, entirely independent of that marked by triangles. The dashed lines are characteristic lines for $(\sqrt{gH})\Delta t/\Delta x=1$.

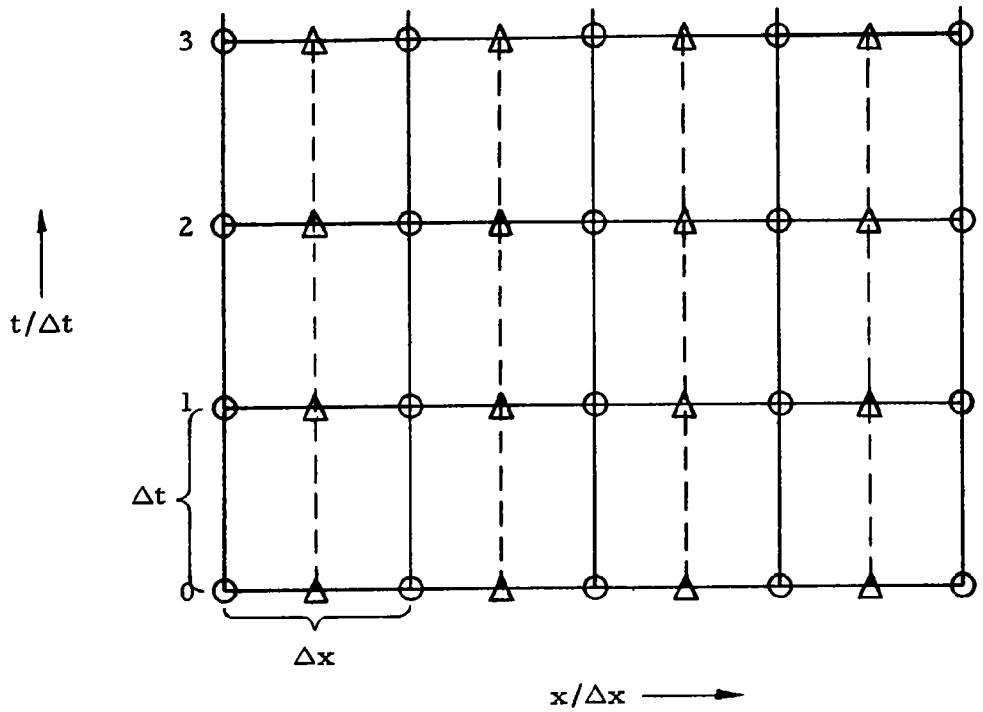

Figure 23.--Schematic illustrating space-staggered grid. In the one(space)-dimensional linear gravity wave problem one variable is defined at points marked by circles; the other variable is defined at points marked by triangles.

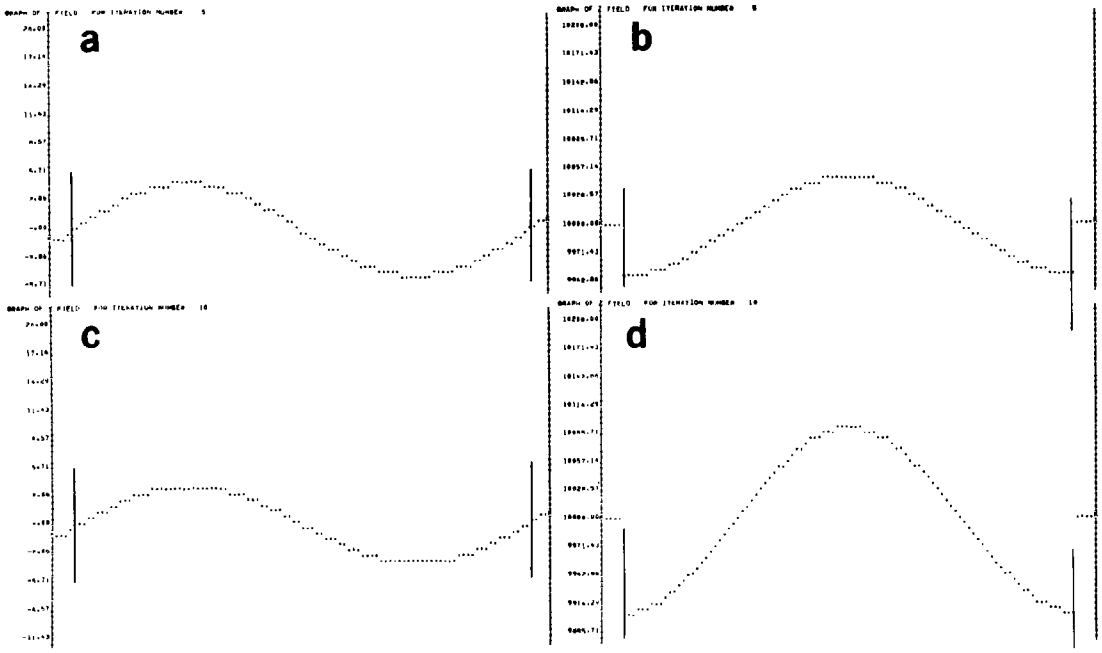

Figure 24.--Numerical solutions of the one-dimensional, linear gravity wave problem on the staggered grid of Figure 23. Velocity is defined at points marked by circles, and is held constant on the boundaries which are marked by short, vertical lines. Height is defined at points marked by triangles. $(\sqrt{gH})\Delta t/\Delta x=1$.

a, b: velocity and height, respectively, at time step 5;
c, d: velocity and height, respectively, at time step 10.

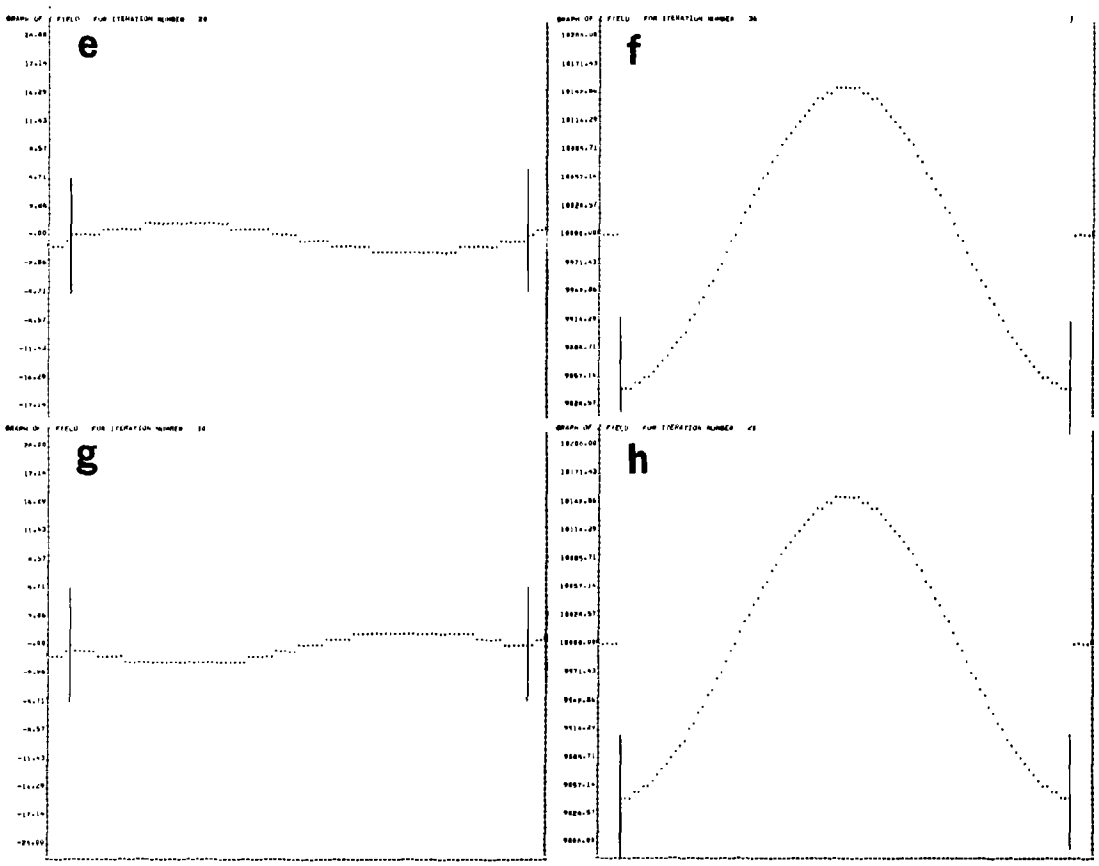

Figure 24.--(continued). Numerical solutions of the one-dimensional, linear gravity wave problem on the staggered grid of Figure 23. Velocity is defined at points marked by circles, and is held constant on the boundaries which are marked by short, vertical lines. Height is defined at points marked by triangles. $(\sqrt{gH})\Delta t/\Delta x=1$.

e, f: velocity and height, respectively, at time step 20;
g, h: velocity and height, respectively, at time step 30.

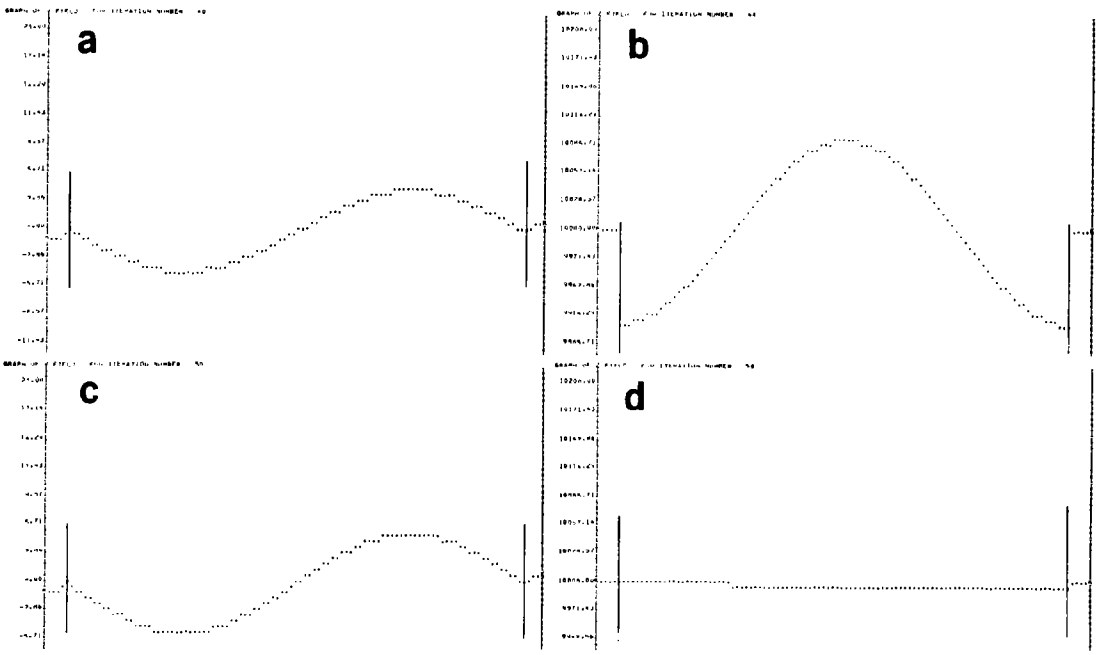

Figure 25.--Numerical solutions of the one-dimensional, linear gravity wave problem on the staggered grid of Figure 23. Velocity is defined at points marked by circles, and is held constant on the boundaries which are marked by short, vertical lines. Height is defined at points marked by triangles. $(\sqrt{gH})\Delta t/\Delta x=1$.

a, b: velocity and height, respectively, at time step 40;
c, d: velocity and height, respectively, at time step 50.

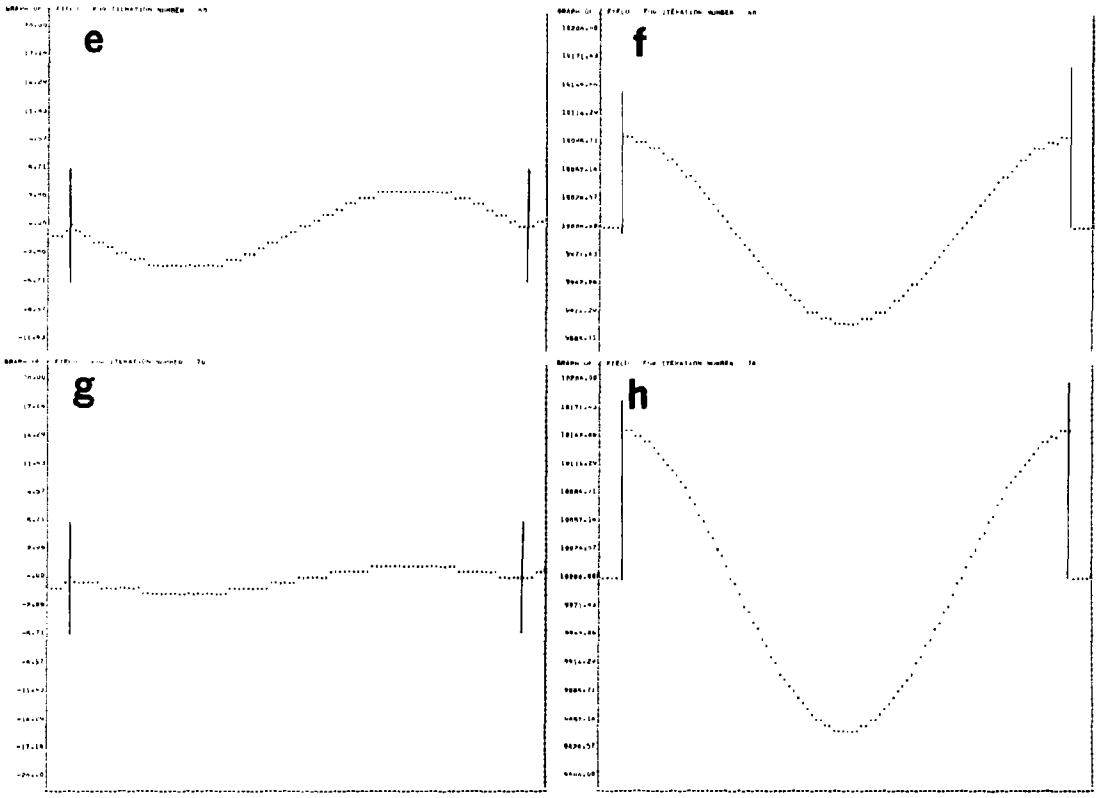

Figure 25.--(continued). Numerical solutions of the one-dimensional, linear gravity wave problem on the staggered grid of Figure 23. Velocity is defined at points marked by circles, and is held constant on the boundaries which are marked by short, vertical lines. Height is defined at points marked by triangles. $(\sqrt{gH})\Delta t/\Delta x=1$.

e, f: velocity and height, respectively, at time step 60;
g, h: velocity and height, respectively, at time step 70.

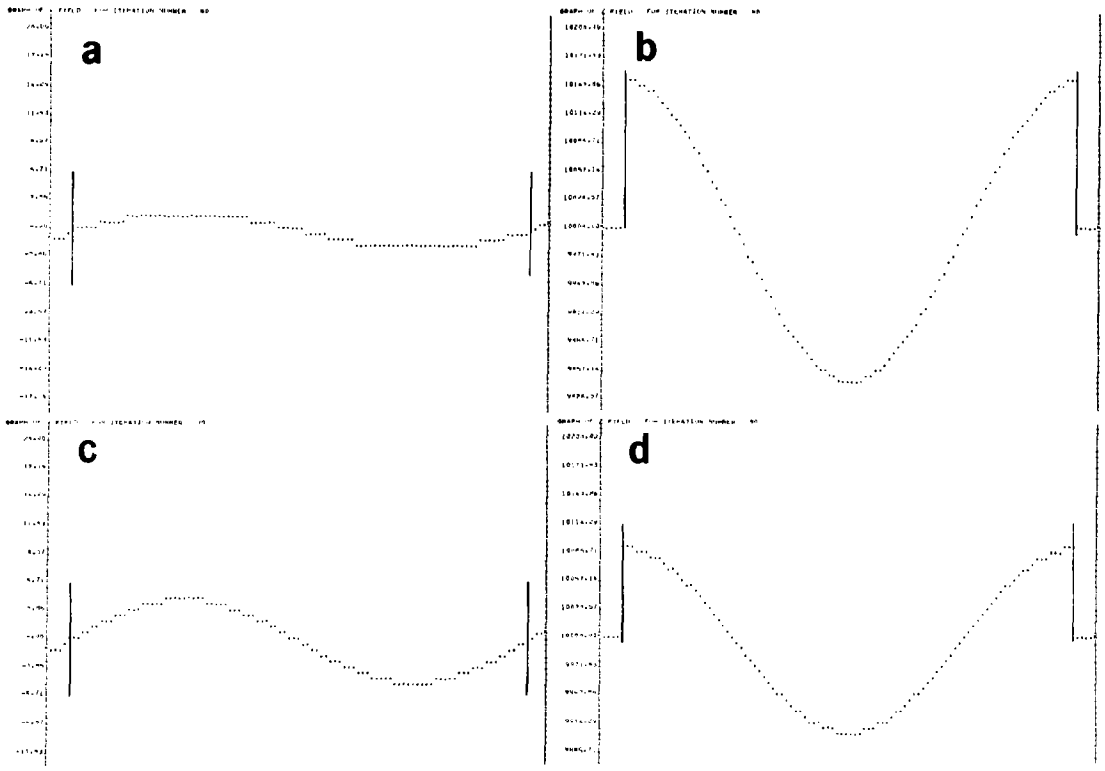

Figure 26.--Numerical solutions of the one-dimensional linear gravity wave problem on the staggered grid of Figure 23. Velocity is defined at points marked by circles, and is held constant on the boundaries which are marked by short, vertical lines. Height is defined at points marked by triangles. $(\sqrt{gH})\Delta t/\Delta x=1$.

a, b: velocity and height, respectively, at time step 80;
c, d: velocity and height, respectively, at time step 90.

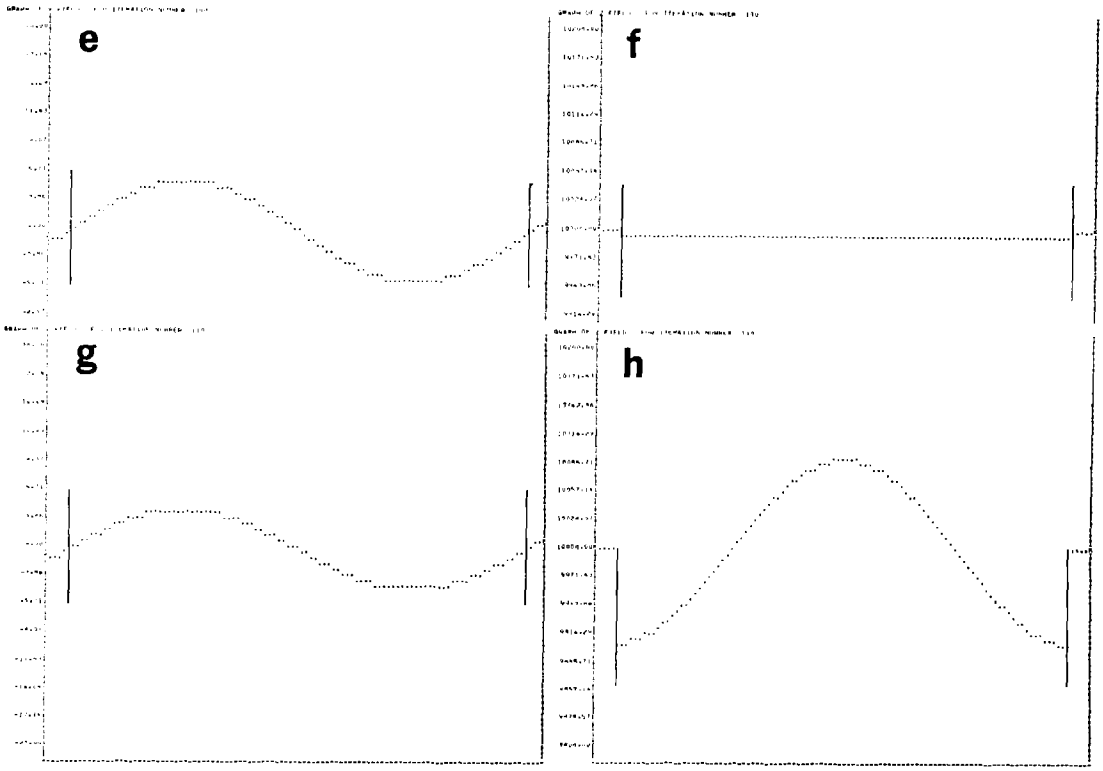

Figure 26.--(continued). Numerical solutions of the one-dimensional linear gravity wave problem on the staggered grid of Figure 23. Velocity is defined at points marked by circles, and is held constant on the boundaries which are marked by short, vertical lines. Height is defined at points marked by triangles. $(\sqrt{gH})\triangle t/\triangle x=1$.

e, f: velocity and height, respectively, at time step 100;
g, h: velocity and height, respectively, at time step 110.

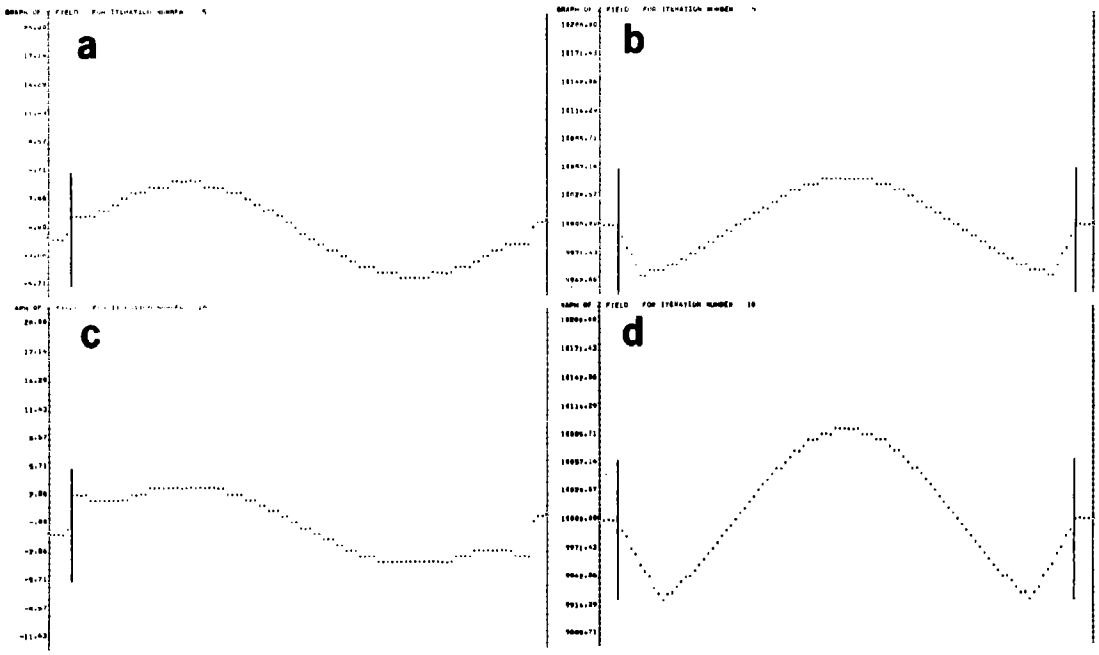

Figure 27.--Numerical solutions of the one-dimensional linear gravity wave problem on the staggered grid of Figure 23. Height is defined at circled points and is held constant on the boundaries which are marked by short, vertical lines. Velocity is defined at points marked by triangles. $(\sqrt{gH})\Delta t/\Delta x=1$.

a, b: velocity and height, respectively, at time step 5;
c, d: velocity and hieght, respectively, at time step 10.

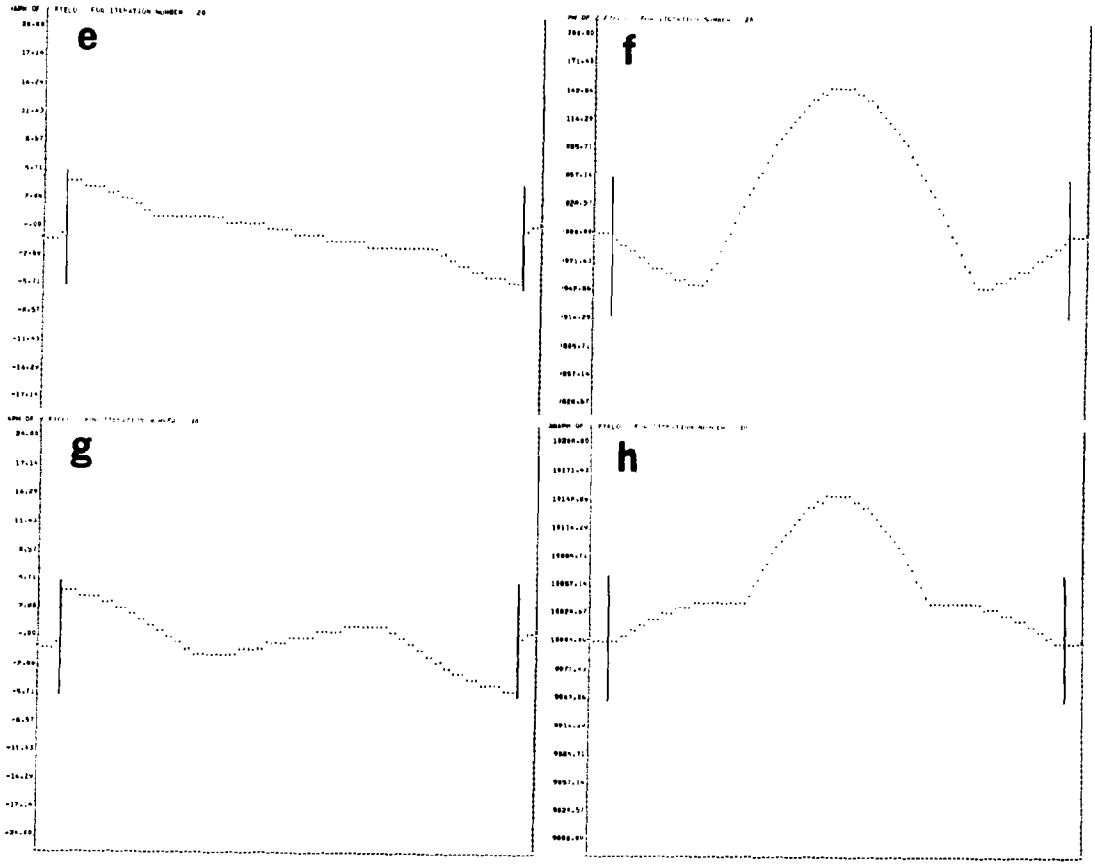

Figure 27.--(continued). Numerical solutions of the one-dimensional linear gravity wave problem on the staggered grid of Figure 23. Height is defined at circled points and is held constant on the boundaries which are marked by short, vertical lines. Velocity is defined at points marked by triangles. $(\sqrt{gH})\Delta t/\Delta x=1$.

e, f: velocity and height, respectively, at time step 20;
g, h: velocity and height, respectively, at time step 30.

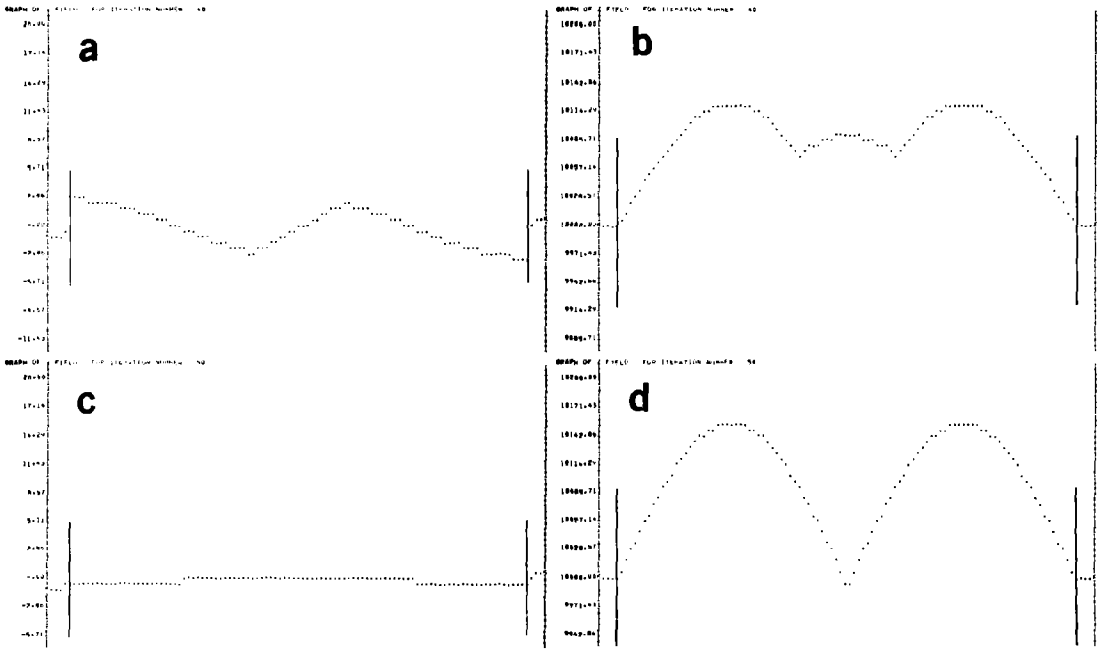

Figure 28.--Numerical solutions of the one-dimensional linear gravity wave problem on the staggered grid of Figure 23. Height is defined at circled points and is held constant on the boundaries which are marked by short, vertical lines. Velocity is defined at points marked by triangles. $(\sqrt{gH})\Delta t/\Delta x=1$.

a, b: velocity and height, respectively, at time step 40;
c, d: velocity and height, respectively, at time step 50.

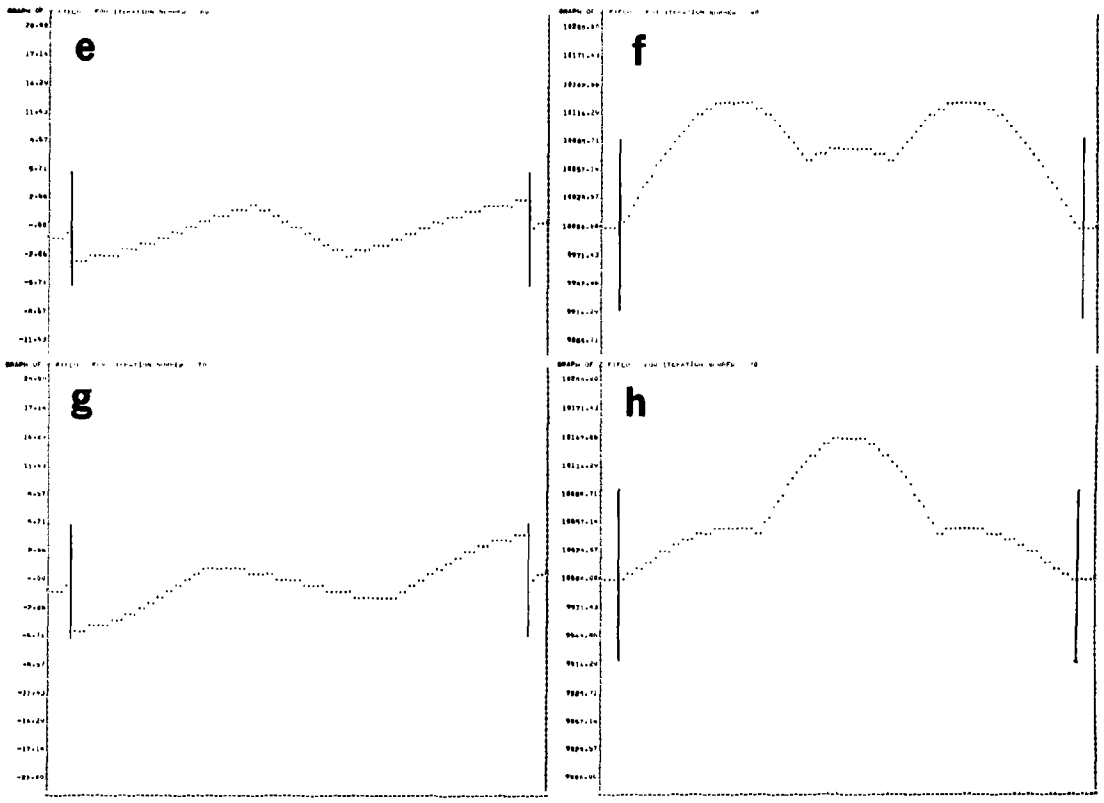

Figure 28.--(continued). Numerical solutions of the one-dimensional linear gravity wave problem on the staggered grid of Figure 23. Height is defined at circled points and is held constant on the boundaries which are marked by short, vertical lines. Velocity is defined at points marked by triangles. $(\sqrt{gH})\Delta t/\Delta x=1$.

e, f: velocity and height, respectively, at time step 60;
g, h: velocity and height, respectively, at time step 70.

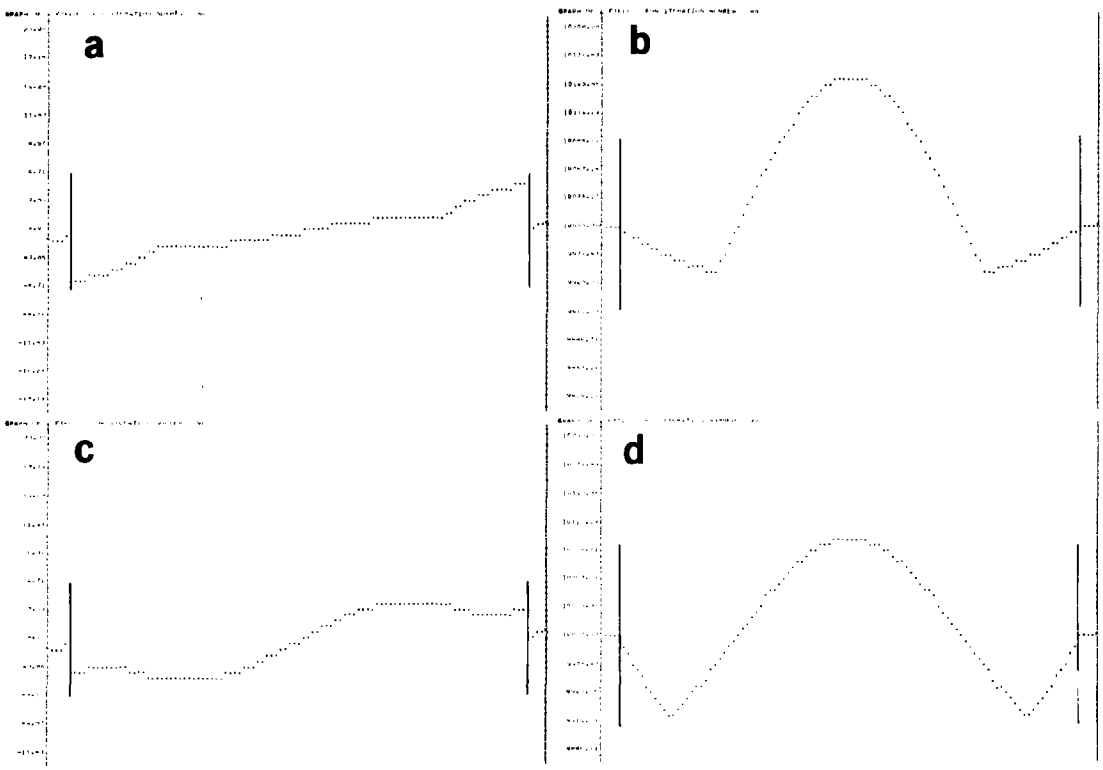

Figure 29.--Numerical solutions of the one-dimensional linear gravity wave problem on the staggered grid of Figure 23. Height is defined at circled points and is held constant on the boundaries which are marked by short, vertical lines. Velocity is defined at points marked by triangles. $(\sqrt{gH})\Delta t/\Delta x=1$.

a, b: velocity and height, respectively, at time step 80;
c, d: velocity and height, respectively, at time step 90.

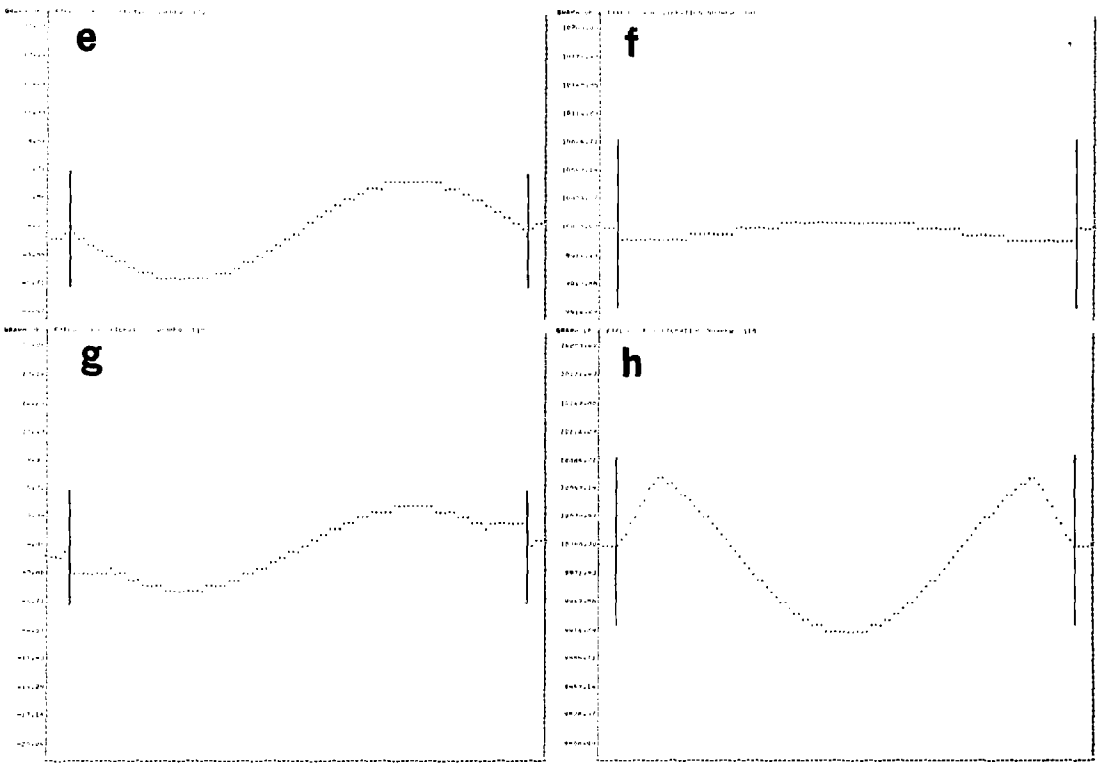

Figure 29.--(continued). Numerical solutions of the one-dimensional linear gravity wave problem on the staggered grid of Figure 23. Height is defined at circled points and is held constant ant the boundaries which are marked by short, vertical lines. Velocity is defined at points marked by triangles. $(\sqrt{gH})\Delta t/\Delta x=1$.

e, f: velocity and height, respectively, at time step 100;
g, h: velocity and height, respectively, at time step 110.

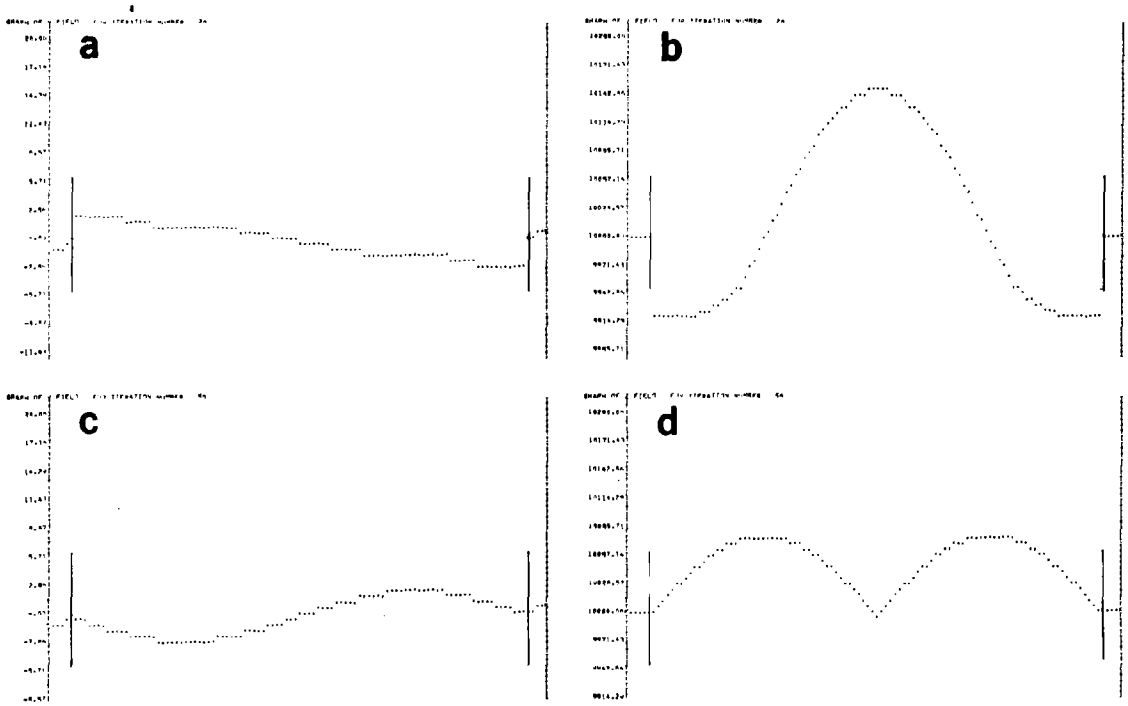

Figure 30.--Numerical solution of the one-dimensional linear gravity wave problem with both velocity and height held constant at the boundaries which are marked by short, vertical lines. The one-step Lax-Wendroff scheme is introduced at the first interior grid point. $(\sqrt{gH})\Delta t/\Delta x=1$.

a, b: velocity and height, respectively, at time step 20;
c, d: velocity and height, respectively, at time step 50.

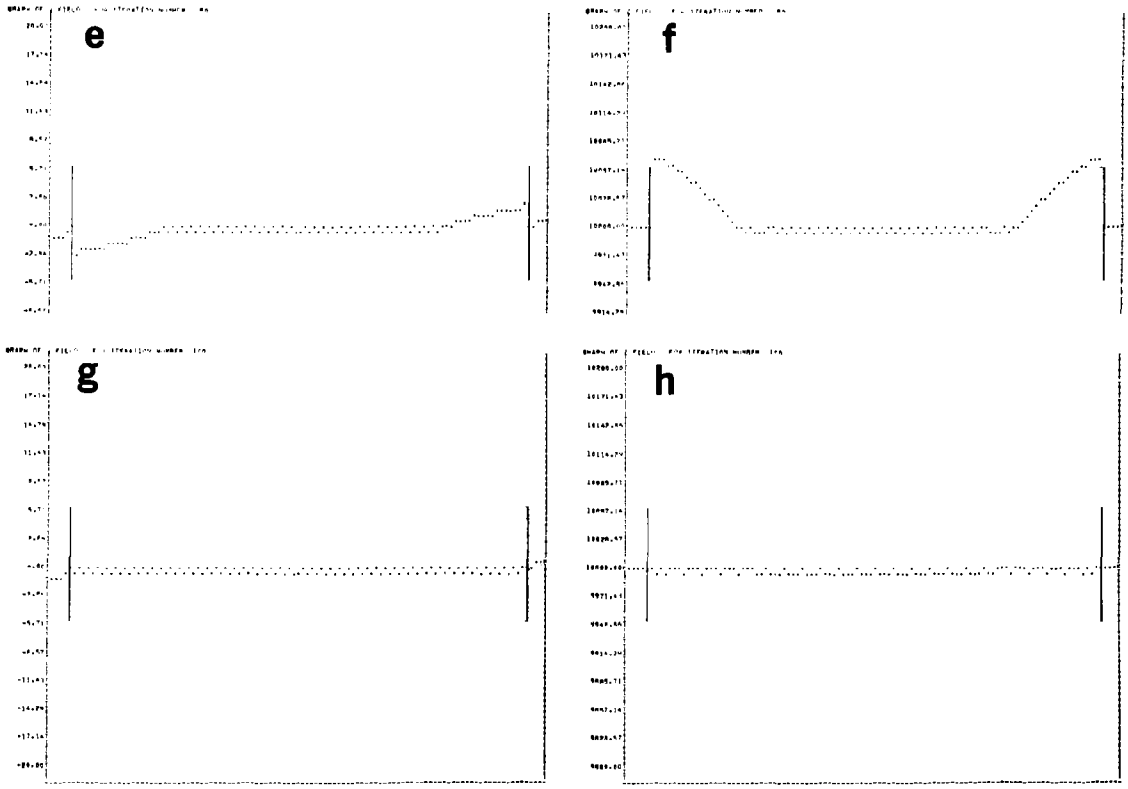

Figure 30.--(continued). Numerical solution of the one-dimensional linear gravity wave problem with both velocity and height held constant at the boundaries which are marked by short, vertical lines. The one-step Lax-Wendroff scheme is introduced at the first interior grid point. $(\sqrt{gH})\Delta t/\Delta x=1$.

e, f: velocity and height, respectively, at time step 80;
g, h: velocity and height, respectively, at time step 100.

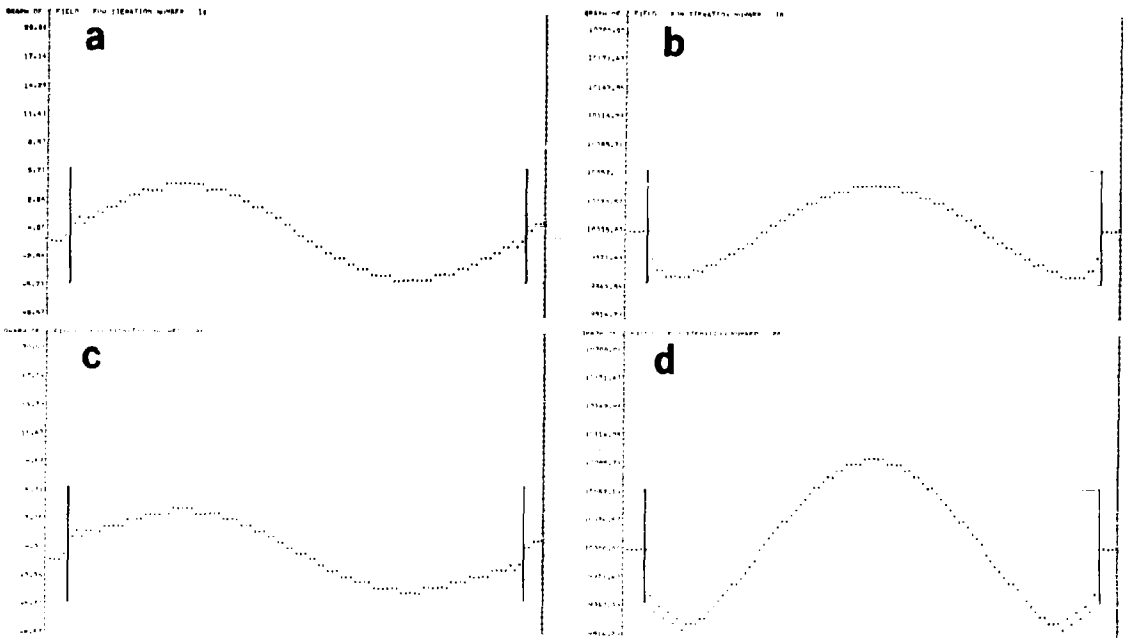

Figure 31.--Numerical solution of the one-dimensional linear gravity wave problem with both velocity and height held constant at the boundaries which are marked by short, vertical lines. The one-step Lax-Wendroff scheme is introduced at the first interior grid point. $(\sqrt{gH})\Delta t/\Delta x=1/2$.

a, b: velocity and height, respectively, at time step 10;
c, d: velocity and height, respectively, at time step 20.

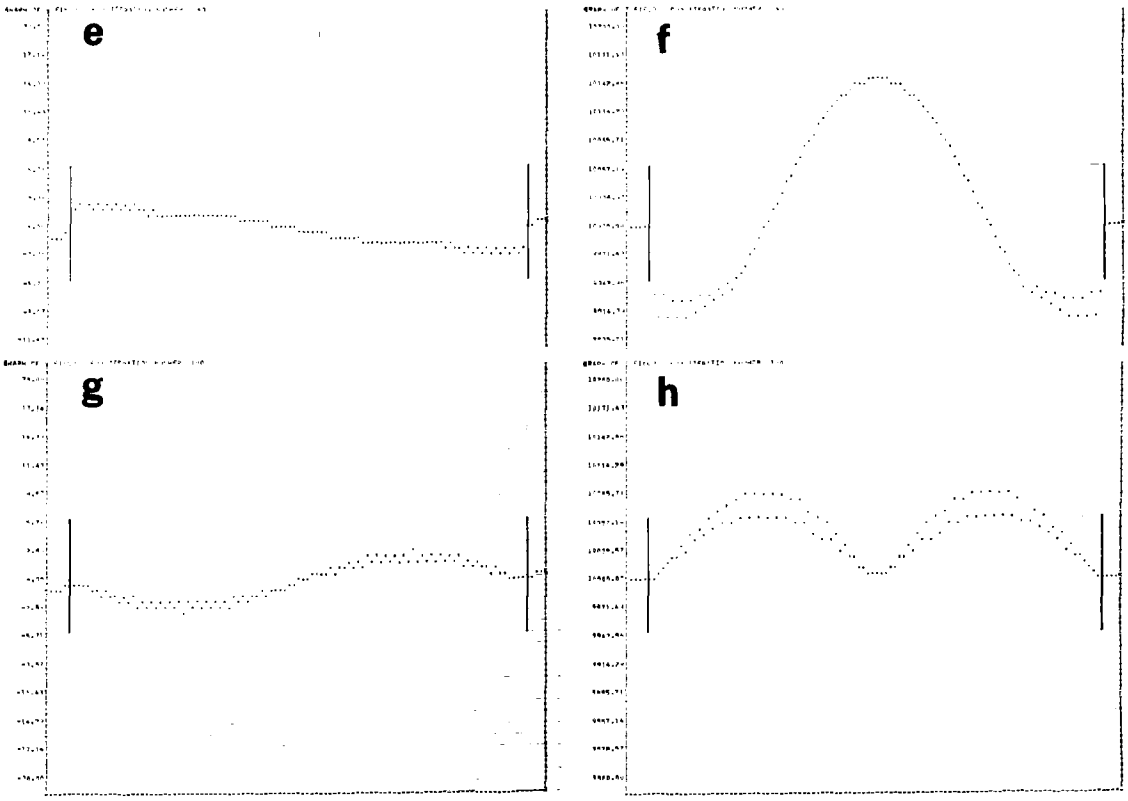

Figure 31.--(continued). Numerical solution of the one-dimensional linear gravity wave problem with both velocity and height held constant at the boundaries which are marked by short, vertical lines. The one-step Lax-Wendroff scheme is introduced at the first interior grid point. $(\sqrt{gH})\Delta t/\Delta x=1/2$.

e, f: velocity and height, respectively, at time step 40;
g, h: velocity and height, respectively, at time step 50.

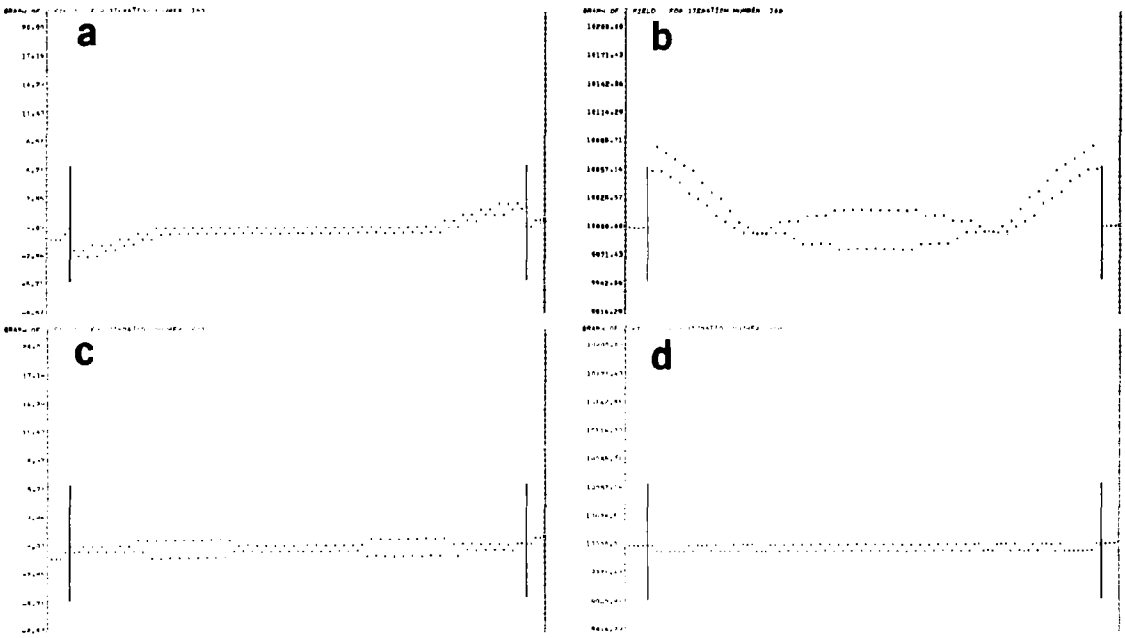

Figure 32.--Numerical solution of the one-dimensional linear gravity wave problem with both velocity and height held constant at the boundaries which are marked by short, vertical lines. The one-step Lax-Wendroff scheme is introduced at the first interior grid point. $(\sqrt{gH})\Delta t/\Delta x=1/2$.

a, b: velocity and height, respectively, at time step 160;
c, d: velocity and height, respectively, at time step 200.

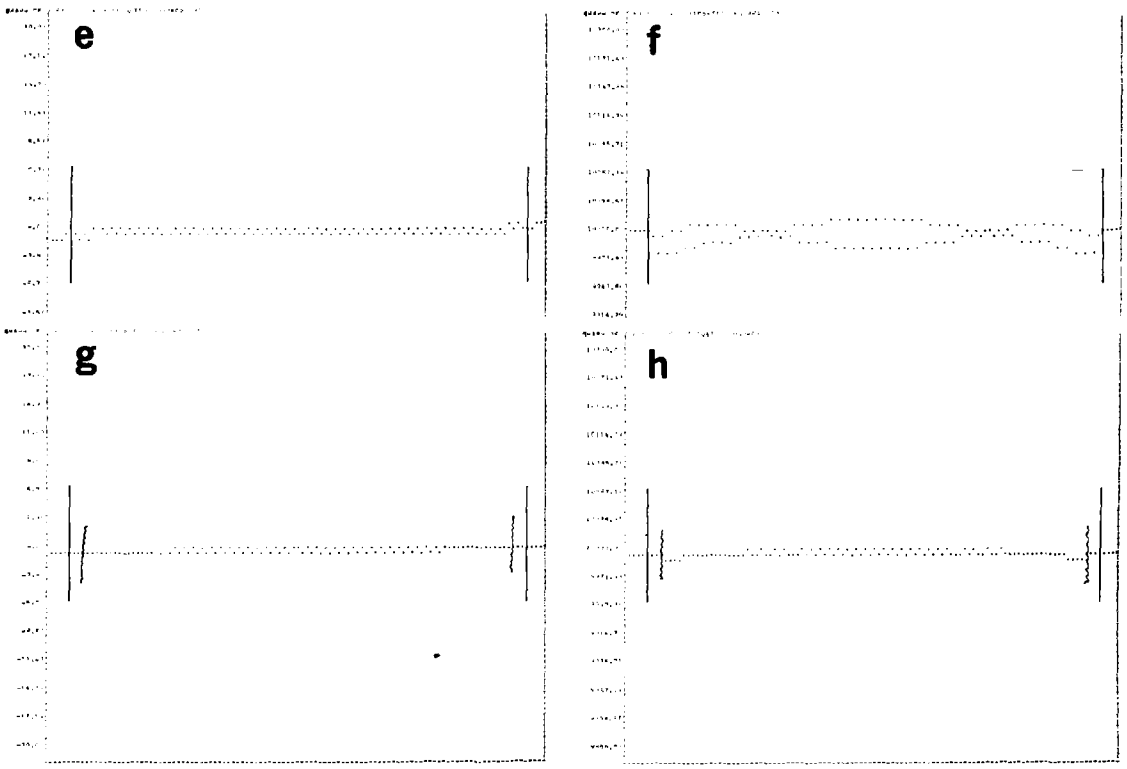

Figure 32.--(continued). Numerical solution of the one-dimensional linear gravity wave problem with both velocity and height held constant at the boundaries which are marked by short, vertical lines. The one-step Lax-Wendroff scheme is introduced at the first interior grid point. $(\sqrt{gH})\Delta t/\Delta x=1/2$.

e, f: velocity and height, respectively, at time step 220;
g, h: velocity and height, respectively, at time step 220; after filtering with the one-dimensional version of the filter described by Gerrity and McPherson (1969).

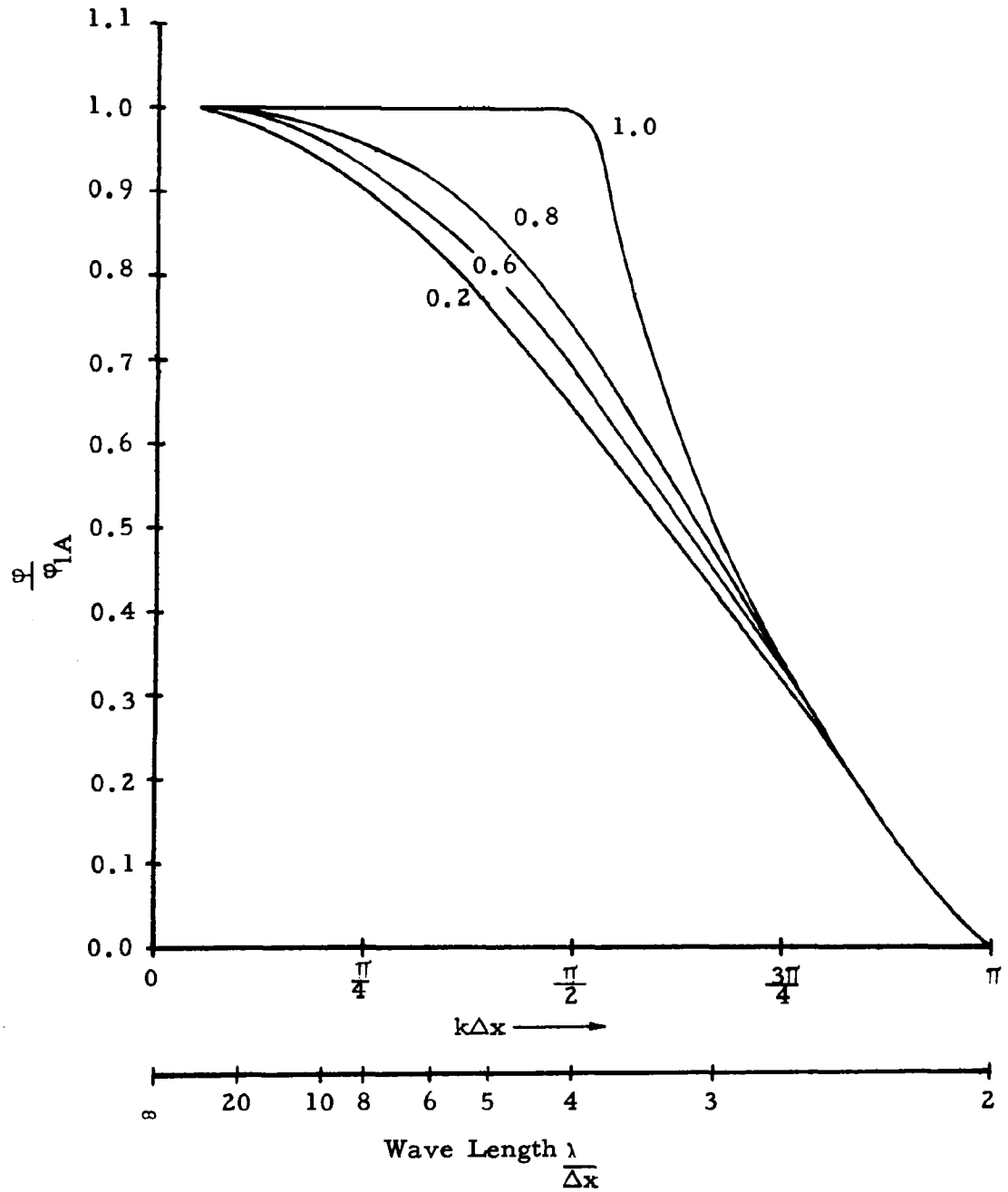

Figure A-1.--Ratio of numerical phase angle φ to analytic phase angle φ_A as a function of wave number k and the stability ratio $(\sqrt{gH})\Delta t/\Delta x$, for centered space-time differences.

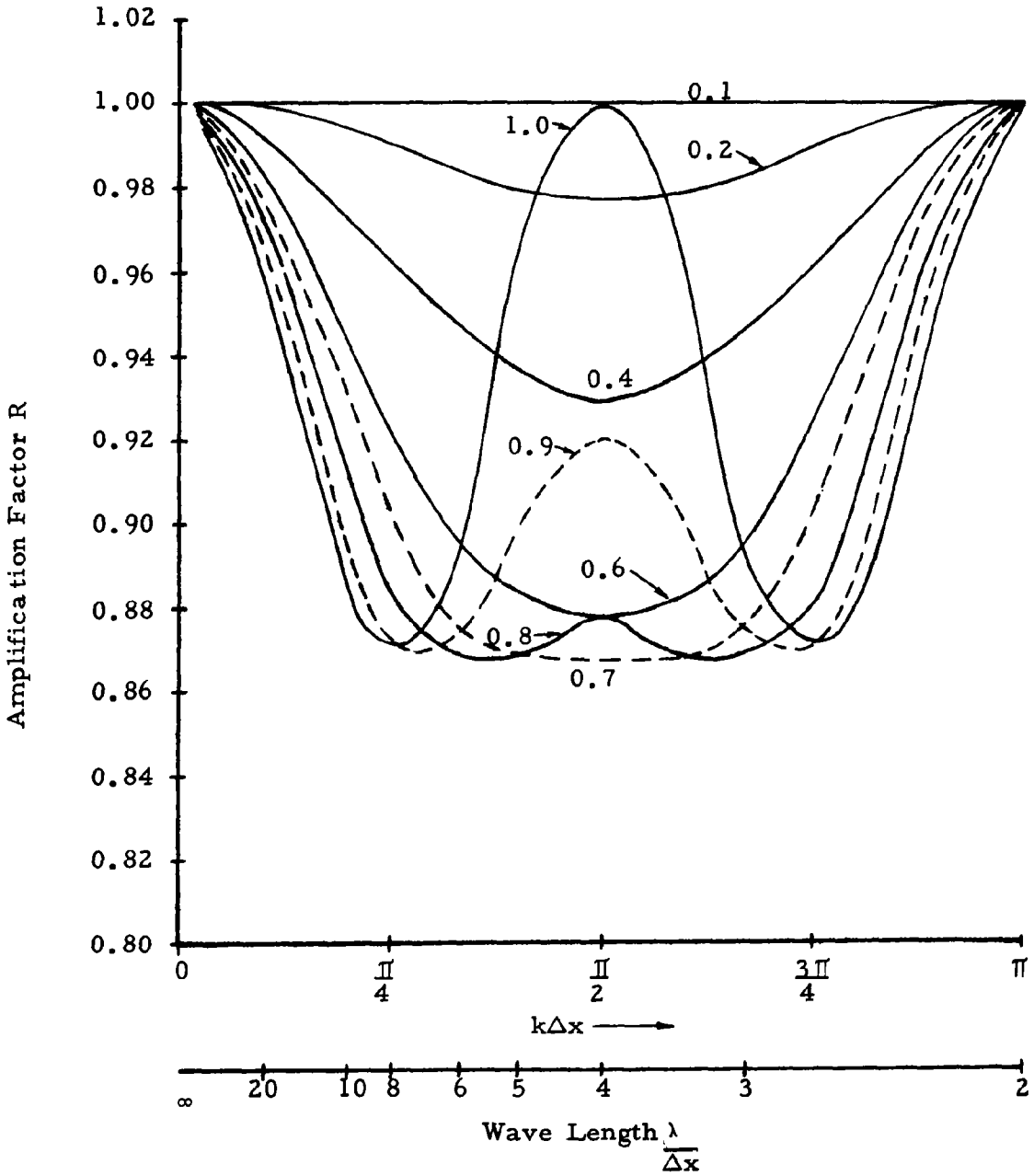

Figure B-1.--Amplification factor R for the Euler-backward method combined with centered-space differences, as a function of wave number k and the stability ratio $(\sqrt{gH})\Delta t/\Delta x$.

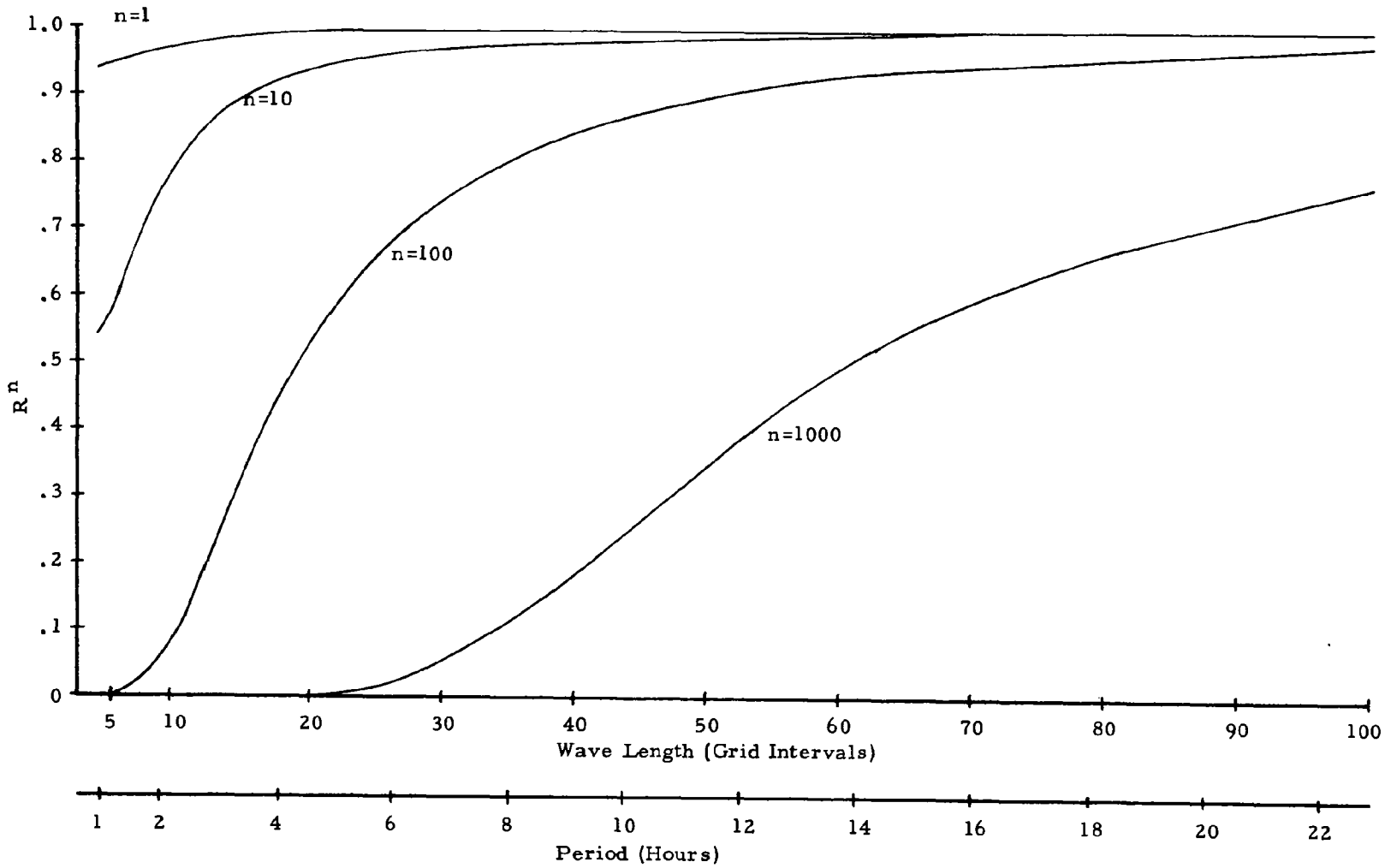

Figure B-2.--Damping associated with the Euler-backward method combined with centered-space differences after 1, 10, 10^2, and 10^3 time steps, as a function of wavelength/period.

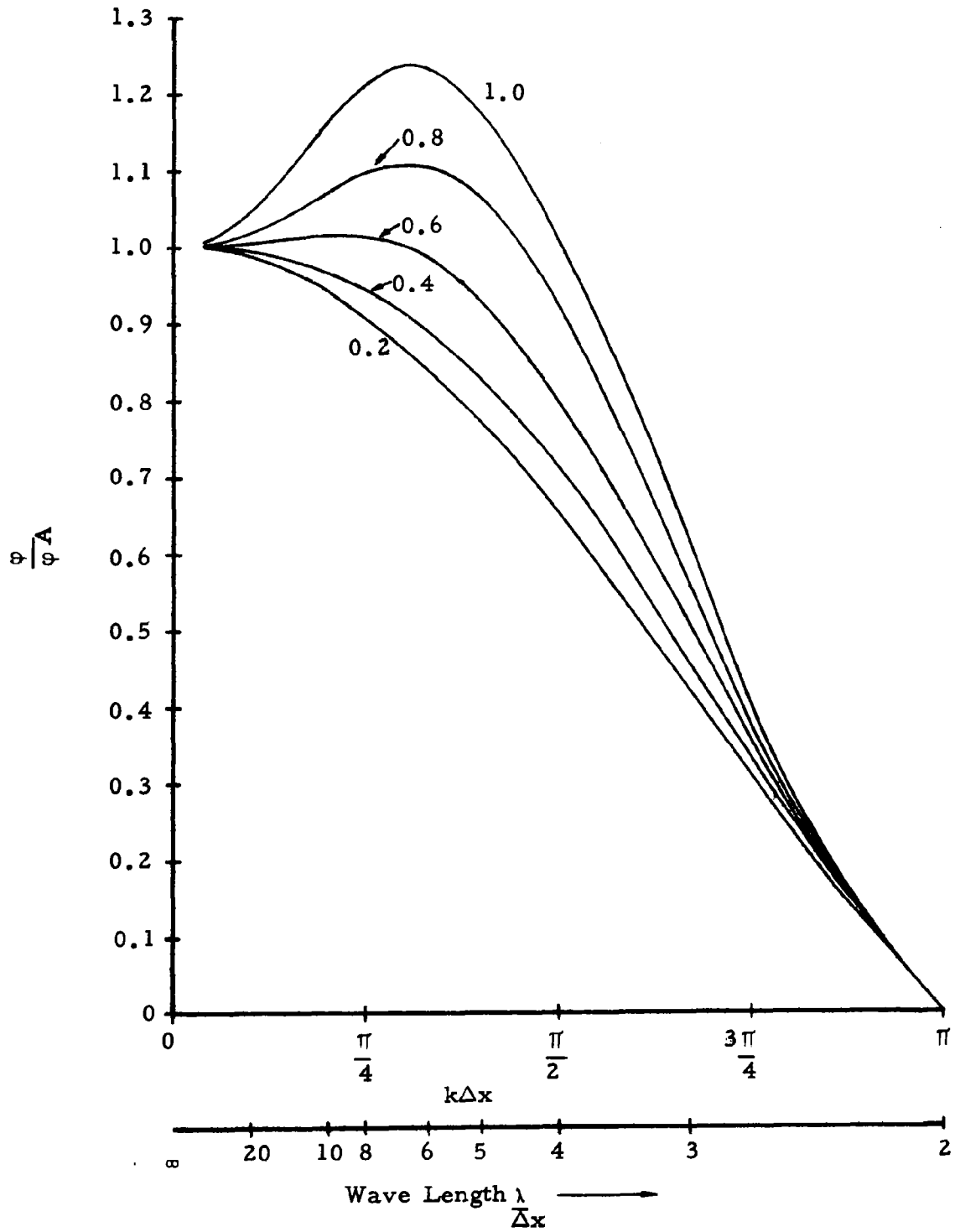

Figure B-3.--Ratio of numerical phase angle φ to analytic phase angle φA as a function of wave number k and the stability ratio $(\sqrt{gH})\Delta t/\Delta x$, for the Euler-backward method combined with centered-space differences.